# Deciphering organic matter degradation in the continuous permafrost zone of Alaska based on biomarker analyses

**Master Thesis**

for the award of the academic degree Master of Science (M. Sc.)

at the University of Potsdam

Faculty of Science

Institute of Environmental Science and Geography

Institute of Physics and Astronomy

**Climate, Earth, Water, Sustainability**


| | |
|---|---|
| Submitted by: | Carolin Luise Frauhammer[2] |
| E-Mail: | carolin.frauhammer@uni-potsdam.de |
| Matriculation number: | 797703 |

| | |
|---|---|
| 1st Supervisor: | Dr. Jens Strauss[1] |
| 2nd Supervisor: | Prof. Dr. Guido Grosse[1,2] |

[1] Alfred-Wegener-Institute Potsdam

[2] University of Potsdam



Potsdam, 6 August 2025

# Table of contents

# Table of contents

# List of figures

# List of figures

# List of tables

# Abbreviations

| | | |
|---|---|---|
| ~ | approximately | |
| ° | degree | |
| °C | degree Celsius | 273.15 K |
| °N | latitudinal position in degrees north the equator | |
| °W | longitudinal position in degrees west the prime median | |
| Ø | Diameter | |
| ‰ | per mille | |
| $\delta^{13}C$ | stable carbon isotope ratio $^{13}C$ and $^{12}C$ | ‰ vs. VPDB |
| $\delta^{18}O$ | stable oxygen isotope ratio $^{18}O$ and $^{16}O$ | ‰ vs. SMOW |
| $\delta D$ | stable hydrogen isotope ratio $^{2}H$ and $^{1}H$ | ‰ vs. SMOW |
| $^{14}C$ | radiocarbon age; radioactive carbon isotope $^{14}C$ and $^{12}C$ | cal. ka BP |
| ACL | average chain length | |
| ACP | Arctic coastal plain | |
| AL | active layer (as permafrost layer) | |
| BP | before present (1950) | |
| b.s.l. | below surface level | cm |
| C | carbon | |
| cal. | calibrated | |
| $CH_4$ | methane | |
| cm | centimetre | $10^{-2}$ m |
| C/N | ratio between TOC and TN | |
| $CO_2$ | carbondioxide | |
| CPI | carbon preference index | |
| DLB | drained thermokarst lake basin core BAL-T0-DLB | |
| DTLB | drained thermokarst lake basin | |
| DOC | dissolved organic matter | mg $L^{-1}$ |
| e.g. | latin: exempli grata; for example | |
| EC | electrical conductivity | µS $cm^{-1}$ |
| eV | electronvolt | $1.602*10^{-19}$ J |
| g | gram | $10^{-3}$ kg |
| GHG | greenhouse gas | |
| HCPC | hierarchical clustering on principal components | |
| Gt | gigaton | $10^{12}$ kg |
| h | hour | 3600 s |
| ha | hectare | 10 000 $m^2$ |
| ka | latin: kilo annus; thousand years | $3.154 * 10^{10}$ s |
| L | thermokarst lake core BAL24-T0-L | |
| M | marine core BAL24-T0-M | |
| $m^3$ | cubic meter | $m^3$ |
| m/z | mass-to-charge ratio | |
| min | minute | 60 s |

# Abbreviations

| | | |
|---|---|---|
| mL | millilitre | $10^{-6}$ $m^3$ |
| mg | milligram | $10^{-3}$ g |
| mm | millimetre | $10^{-3}$ m |
| MPa | megapascal | $10^{6}$ Pa |
| n.valid | number of valid cases | |
| nm | nanometre | $10^{-9}$ m |
| ns | not statistically significant | |
| OM | organic matter | |
| p | p-value; probability for a statistical test | |
| $p_{aq}$ | aquatic proxy | |
| PCA | principal component analysis | |
| PF | perennial frozen (as permafrost layer) | |
| pH | potential of hydrogen | |
| $p_{wax}$ | terrestrial proxy | |
| R | Pearson's correlation coefficient | |
| $R^2$ | coefficient of determination | |
| Sed | sediment | |
| SOC | soil organic carbon | |
| SMOW | standard mean ocean water | ‰ |
| T | talik (as permafrost layer) | |
| TC | total carbon | wt% |
| TIC | total inorganic carbon | wt% |
| TL | thermokarst lake | |
| TN | total nitrogen | wt% |
| TOC | total organic carbon | wt% |
| u | unified atomic mass unit | $1.661 * 10^{-27}$ kg |
| UL | upland core BAL24-T0-UL | |
| vol% | per cent by volume | |
| VPDB | Vienna Pee Dee Belemnite | ‰ |
| wt% | per cent by weight | |
| µg | microgram | $10^{-9}$ kg |
| µL | microliter | $10^{-6}$ L |
| µS | microsiemens | $10^{-6}$ S |

# Abstract

Human-induced climate change has led to a significant rise in global temperatures, with the Arctic warming nearly four times faster than the global average. This accelerated warming makes the Artic to one of the most vulnerable regions on Earth. A major compo-nent of this region is permafrost, permanently frozen grounds that covers around 22 % of the exposed land are of the northern Hemisphere. Permafrost regions store vast amounts of carbon and are therefore a key point in the carbon-climate-cycle, as the strong warming threatens the stability of the frozen ground and makes these storages available for micro-bial decomposition, which increases the greenhouse gas production. In particular thermo-karst processes – ground subsidence caused by the thawing of ice-rich permafrost – re-shape permafrost landscapes, resulting in degeneration features as thermokarst lakes, drained thermokarst lake basins and coastal erosion. This mobilizes previously frozen organic matter, altering its composition, reactivity and greenhouse gas potential. Thus, knowledge about the origin, quantity and quality are essential to estimate the future fate of organic matter in a changing permafrost landscape. This study addresses these knowledge gaps by analysing OM characteristics in northwestern Alaska. The aim of this study is to investigate (1) the paleoenvironment of the landscape and (2) the characteriza-tion of the OM by its quantity, source and quality. Therefor a multiproxy approach of bio-geochemistry, hydrochemistry, sedimentology and biomarker analyses for a transect along the four main features Upland, Thermokarst lake, Drained Thermokarst Lake Basin and Marine on the Baldwin Peninsula was used.

The deposition in this region started > 50 cal ka BP in a strongly aeolian regime. The sediments are mostly of coarse silt, indicating parent material at all four sites, and show with high water contents, organic-rich layers and high radiocarbon ages typically characteris-tics of late Pleistocene Yedoma, while the bottom layers show signs of an ancient fluvial environment and former thermokarst processes. Also, the biomarker analysis suggests a common terrestrial origin of the OM, also for the marine site, indicating a secondary ma-rine infiltration, as well as a slightly aquatic influences, especially in the deeper layers, resulting from ancient thermokarst processes and the lake / marine phases. The carbon quantity decreases significantly from the Upland to the Marine site. It has a high quality without statistically significant differences between the sites.

Due the high ice amount and carbon quality, the studied deposits are highly vulnerable to thawing under future warming and thus constitute a high greenhouse gas release potential.

# Zusammenfassung

Der anthropogene Klimawandel hat zu einem signifikanten Anstieg der globalen Temperatur geführt, wobei sich die Arktis fast viermal so schnell wie der globale Durchschnitt erwärmt. Diese beschleunigte Erwärmung macht sie zu einer der vulnerabelsten Regionen der Welt. Einer der Hauptbestandteile dieser Region ist Permafrost, dauerhaft gefrorener Boden, der ~22 % der freiliegenden Landfläche der nördlichen Hemisphäre bedeckt. Per-mafrost Regionen speichern große Mengen an Kohlenstoff und sind dadurch ein Kern-punkt im Kohlenstoff-Klima-Kreislauf, da die starke Erwärmung die Stabilität des gefro-renen Bodens und damit des Kohlenstoffes gefährdet. Besonders Thermokarstprozesse – Bodenabsenkung infolge des Tauens von eisreichem Permafrost – verändern diese Land-schaften und schaffen Strukturen wie Thermokarstseen, drainierte Thermokarstseebecken und Küstenerosion. Das wiederum mobilisiert zuvor eingefrorenes organisches Material, verändert dessen Zusammensetzung und Treibhausgaspotential. Daher ist es essenziell, mehr Wissen über die Charakteristik des organischen Materials zu erlangen, um dessen zukünftige Entwicklung in einer sich wandelnden Permafrost Landschaft abzuschätzen. Diese Studie fokussiert sich auf diese Wissenslücke. Ziel ist die Untersuchung (1) der Pa-läoumwelt und Entstehung der Landschaft sowie (2) die Charakterisierung der OM an-hand ihrer Quantität, Herkunft und Qualität. Dafür wird ein Multi-Proxy-Ansatz aus Bio-geochemie, Hydrochemie, Sedimentologie und Biomarker Analyse entlang eines Tran-sekts mit vier Hauptmerkmalen – Hochebene, Thermokarstsee, drainiertes Thermokarst-seebecken und marine Ablagerungen – auf der Baldwin-Halbinsel angewendet. Die Abla-gerung startet vor über 50 cal ka BP in einem stark äolischen Regime. Die Sedimente be-stehen überwiegend aus grobem Schluff, was auf dasselbe Ausgangsmaterial an allen Standorten hinweist. Sehr hohe Eisgehalte, organikreiche Schichten und Radiokarbonalter > 30 cal ka BP deuten auf typische Eigenschaften spätpleistozänen Yedomas hin, während tiefere Schichten Spuren früherer fluvialer Bedingungen und Thermokarstprozesse auf-weisen. Die Biomarker Analyse bestätigt einen gemeinsamen terrestrischen Ursprung der OM, auch am marinen Standort, der terrestrisch abgelagert und später durch Erosion und Infiltration marin überprägt wurde. Die Kohlenstoffmenge nimmt vom Hochland zum marinen Standort deutlich ab. Sie weist eine hohe Qualität auf, ohne signifikante Unter-schiede zwischen den Standorten. Aufgrund hoher Eismengen, potenzieller Talikbildung und undegradierten Kohlenstoffs sind die untersuchten Ablagerungen sehr anfällig für Auftauen unter zukünftiger Erwärmung und stellen somit ein hohes Treibhausgas Freisetzungspotenzial dar.

# 1. Introduction

## 1.1 Thematic relevance

Humanity and ecosystems are currently facing on the most pressing challenges due anthropogenic global warming. The climate has warmed at a rate unprecedented in at least the last 2 000 years by human's influence, with higher temperatures each of the last four decades than any previous one since 1850 (IPCC 2023c). According to the IPCC (2023a), the global surface temperature in 2011 – 2020 was around 1.1 °C above 1850 – 1900 due to human caused stronger radiative forcing, mainly by increasing concentrations of the greenhouse gases (GHG) carbon dioxide ($CO_2$), methane ($CH_4$) and nitrous oxide ($N_2O$). In 1900 – 2019, atmospheric $CO_2$ has risen as a minimum ten times faster than any previous in the last 800 000 years and likely four – five times faster than in the past 56 million years (IPCC 2023b). Regardless of emission scenarios, global temperatures are projected to rise by more than 2 °C by mid-century unless negative GHG emissions occur in the coming decades. Climate change has strong effects on all compartments of the earth systems, as sea-ice and ice-sheet loss, glacier retreat, global mean sea level rise due land ice loss and thermal expansion and the weather. So, additional warming will increase the frequency and intensity of climate extremes as heatwaves, heavy precipitations, drought and tropical cyclones (IPCC 2023c). Especially the polar regions are highly climate-sensitive areas on the planet, with the Arctic having warmed up to four times as fast as the global average in the last 30 years, as seen in Figure 1, and is projected to continue to warm with above two times the rate of global warming and an increase in the temperature of the coldest days three times the rate of global mean (Rantanen et al. 2022).

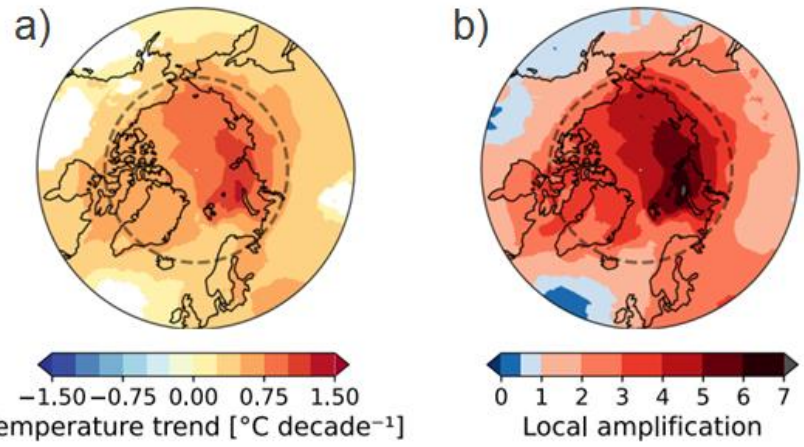


*Figure 1. (a) Annual mean temperature trends and (b) local amplification ratio from 1979 – 2021. The Artic circle (66.5 °N latitude) is indicated by the dashed line. From Rantanen et al. 2022.*

This phenomenon is called Arctic amplification, likely caused among others by increasing ocean heating and ice-albedo feedback (Screen and Simmonds 2010; Dai et al. 2019), Plank feedback (Pithan and Mauritsen 2014), lapse-rate feedback (Stuecker et al. 2018), inversion of the Arctic wintertime temperature (Bintanja et al. 2011), cloud feedback (Taylor et al. 2013), enhanced horizontal ocean heat transport (Beer et al. 2020) and transport of moist air into the arctic (Woods and Caballero 2016).

Permafrost soils, underlaying 15 % of the terrestrial environment of the Northern Hemisphere, are particularly vulnerable to global warming, with increasing ground temperatures to record high levels up to 2 – 3 °C warmer than 30 years ago (IPCC polar regions 2019). This warming causes a deepening of the active layer, the layer above the permafrost which is subject to annual thawing and freezing, up to complete thawing in the future (Schaeffer et al. 2011). The consequences of permafrost degradation are one the one hand regional impacts as change of ecosystems and hydrology, infrastructure damages and food security, especially for indigenous people living in these regions. Moreover, approximately 1 538 Gt carbon (C) are stored in the terrestrial permafrost region, which accounts for ~30 % of the global C pool in only ~15 % of the global land area. In addition, there are estimated 2 822 Gt C stored in subsea permafrost, resulting in 4 360 Gt C in total, as seen in Figure 2 (Strauss et al. 2025).

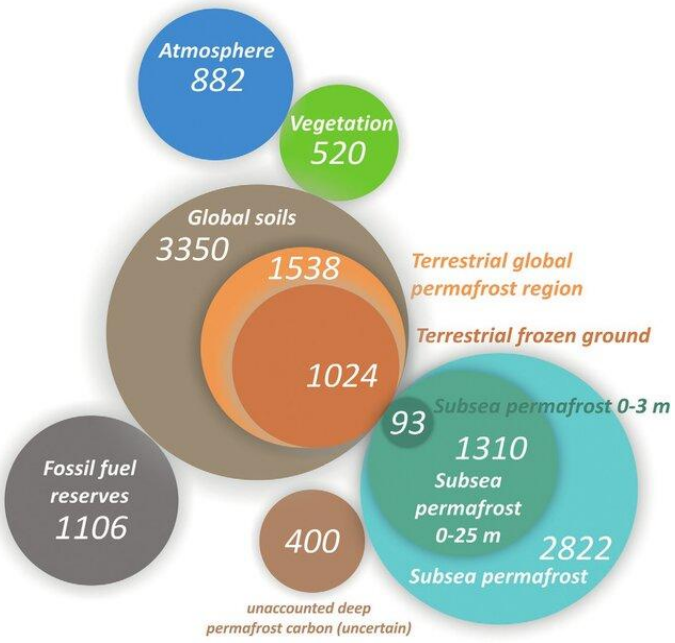


*Figure 2. Atmospheric and terrestrial carbon stocks in relation to carbon stored in the permafrost zone, given in Gt, with the size of the circles proportional to the size of the carbon stocks. The global soil estimate (3350 Gt) is based on soils ≤ 3 m depth (2800 Gt) as well as deep permafrost > 3 m depth (500 Gt) and tropical peatlands (50 Gt; (Jackson et al. 2017)). Based on data from different IPCC reports, (Miesner et al. 2023) and (Hugelius et al. 2014; Hugelius et al. 2020). Adapted and updated from (Strauss et al. 2017). Figure from Strauss et al. (2025).*

The further Arctic warming is expected to make these deposits of organic-rich material trapped within permafrost more accessible for microbial decomposition, leading to heightened production of GHG as permafrost thaws, and thus in further climate warming; the positive permafrost carbon feedback, Figure 3 (Schuur et al. 2008; Schaeffer et al. 2011). One of the most abundant forms of permafrost degradation in ice-rich Arctic landscapes is thermokarst (Section 2.3), resulting from the thawing of excess ice-bearing permafrost or the melting of massive near-surface ice due active layer deepening (van Everdingen 2005; Morgenstern et al. 2011; Farquharson et al. 2022). The following surface lowering can lead to the formation of thaw lakes, called thermokarst lakes (TL) (van Everdingen 2005; Grosse et al. 2011), which grow, coalesce and eventually drain to drained thermokarst lake basins (DTLB), resulting in a lake-drained lake basin system (Fuchs et al. 2019). As thermokarst is already the dominant landscape change process in the Arctic with occupying ~20 % of the northern permafrost region, rising permafrost temperatures induce an increase in frequency and magnitude of thermokarst as well as a shift to landscapes dominated by DTLBs (Olefeldt et al. 2016; Jones et al. 2022; Jones et al. 2023). TLs have been shown to release organic carbon (OC) previously frozen in permafrost, especially since they can reach and thus mobilize old, deep permafrost carbon. DTLBs have the potential to reaggregate permafrost in a cold climate, though this potential will slow or not occur in a warming climate (Jones et al. 2022).

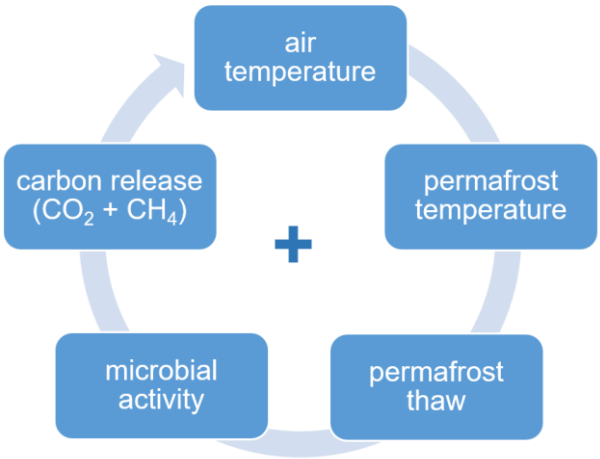


*Figure 3.The permafrost-carbon feedback loop.*

In addition, there is the process of talik formation (perennially thawed subsurface soils) by an adjustment of the active layer to a new thermal regime (Jorgenson et al. 2010), thermokarst related under a lake (subaquatic) due thermal interaction between surface water and permafrost (Parsekian et al. 2013), or non-lake environments (subaerial), when the summer thaw-depth exceeds the winter freeze-depth (Farquharson et al. 2022). The formation of talik

is of special interest for the permafrost-carbon feedback, as it accelerates permafrost degradation and can mobilize old soil organic carbon (SOC) in deep permafrost (> 3 m), leading to a potential shift in the Arctic ecosystems from a C sink to a C source in long-term (Parazoo et al. 2018).

Many TLs and DTLBs are located close to the coast and are therefore strongly influenced by it and its changes (Hussey and Michelson 1966). The Arctic coastlines, which account for approximately 34 % of global coastlines (Lantuit et al. 2012), are with on average 0.5 m $a^{-1}$ and with locally up to 47 m $a^{-1}$ under the fastest eroding coasts (Lantuit et al. 2012; Obu et al. 2017; Malenfant et al. 2022), leading to a high release of c into the Arctic sea (Creel et al. 2024) and a change of the biochemistry of the permafrost soils by salt inundation (Jenrich et al. 2021).

Due to the resulting transition from a terrestrial to a marine permafrost environment through coastal erosion, marine sites represent a potentially end-member version along a permafrost degradation transect in the Arctic coastal plain (ACP). Thereby they serve as an excepted future fate of degraded carbon from thermokarst affected soils. Especially knowledge about biochemical properties of the soils as well as processes mobilizing and decomposing deep, old carbon in the context of thermokarst, talik development and marine transgression are rare. As the mobilization and decomposition of organic matter (OM) also highly depends on soil properties as grain size (distribution), pH and C/N, investing theses parameters is key to assess the quality and especially the potential GHG release of C from a permafrost affected landscape (Strauss et al. 2015). Additional biomarker analysis can support these by contributing information about the C sources as well as the quality (Fuchs et al. 2019).

## 1.2 Aim of the study

As there is sparse knowledge about C stocks, quality and mobility in thermokarst affected permafrost regions (Fuchs et al. 2019), this study uses a multiproxy approach of biogeochemistry, hydrochemistry, sedimentology and biomarker analyses to investigate the source and quality changes of OM affected by permafrost degradation along a landscape transect – from an undegraded upland, a thermokarst lake and drained thermokarst lake basin up to a marine site – to assess the potential vulnerability of the stored OM (Fuchs et al. 2019). The aim is to gain a further knowledge of the processes influencing the stability and mobility of OM in a changing permafrost landscape and of its potential future under further climate warming. Therefore, the four primary landscape units Upland (UL), Thermokarst Lake (L), Drained Lake Basin (DLB) and Marine (M), as well as the three permafrost layers contained

therein, active layer (AL), perennial frozen (PF) and talik (T), were used to create a space-for-time approach along a geomorphological gradient of multiple successive permafrost degradation stages in the ACP. The resulting research objectives of this study are:

1) Reconstruction of the paleoenvironment of the landscape and the four landscape units
2) Characterisation of the OM with respect to differences between the four landscape units and the three permafrost layers, regarding:
    a. Quantity of the stored OM
    b. Source of the stored OM
    c. Quality of the stored OM and its development along the transect and the degradation of the permafrost

# 2. Theoretical background

## 2.1 Periglacial environment and permafrost

Periglacial refers to conditions, processes and landforms associated with cold, non-glacial environments. These environments are dominated by frost action processes and often underlain by permafrost (van Everdingen 2005). Permafrost itself is defined as any ground with a maximum of 0 °C for at least two consecutive years, this can be soil or rock, frozen or unfrozen (van Everdingen 2005). The thickness of permafrost varies between 350 and 650 m in the continuous permafrost zone of the Northern Hemisphere and between 1 and 50 m in the discontinuous zone (Strauss et al. 2021a). In the Northern Hemisphere, the permafrost region covers around 22 % of the terrestrial environment, as seen in Figure 4. This includes more than 60 % of the Russian Federation, up to 46 % of the Canadian land surface, large areas of Alaska, Tibet and China, Greenland, northern Scandinavia, and Antarctic islands and dry valleys (Obu et al. 2019). Depending on the geographic continuity in the landscape, permafrost is categorized into four zones: the continuous zone with permafrost underlying 90 – 100 %, the discontinuous zone with permafrost underlying 50 – 90 %, the sporadic zone with permafrost underlying 10 – 50 % and isolated patches with permafrost underlying 0 – 10 % of the area.

Large quantities of permafrost were formed mostly during the late Pleistocene (126 – 11.7 ka BP) in the lowlands and hills of the northern circumpolar region as a remnant of the paleoclimate. The formation was syngenetic, deposition and permafrost development at the same time, as the Yedoma permafrost (Section 2.2), and epigenetic, permafrost aggregation in existing deposits, as mostly in uplands (Péwé 1975; Kanevskiy et al. 2011; Schirrmeister

et al. 2011b; Kanevskiy et al. 2014; Ping et al. 2015). During the Holocene (<11.7 ka BP), a more modern permafrost formed under contemporary conditions by deglaciation and vegetation succession under cold climatic conditions, mostly in the sub-Arctic and boreal zone (Zoltai and Tarnocai 1975; Ping et al. 2015). The upper layer of the permafrost, which is subject to annual thawing and freezing, is called the active layer. The active layer thickness (the depth to which it thaws in summer) depends on air temperature, vegetation, drainage, soil or rock type, moisture, snow cover as well as degree and orientation of the slope (van Everdingen 2005). It ranges in the continuous zone from a few decimetres to more than 2 m, whereby it can exceed several meters in the discontinuous zone (Schuur et al. 2008).

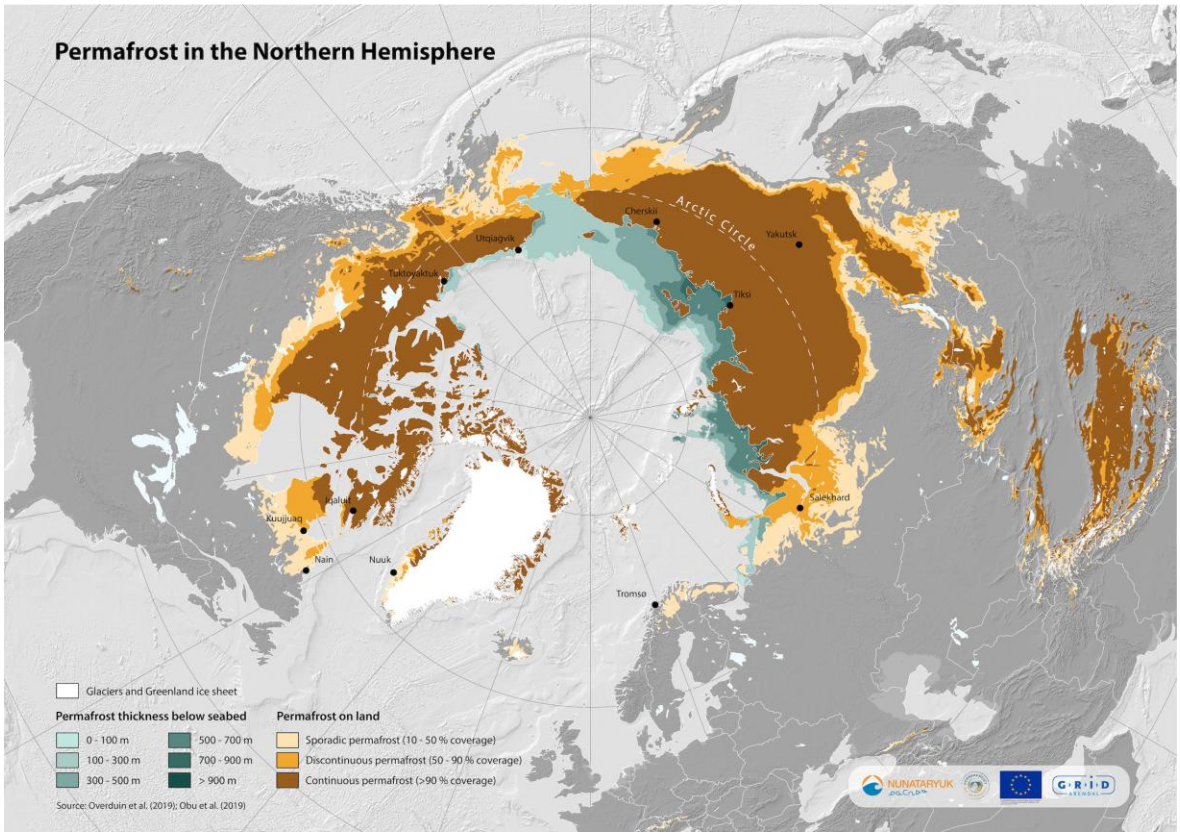


*Figure 4. Distribution and extent of the terrestrial and subsea Northern Hemisphere permafrost. GRID-Arenal based data from Obu et al. (2019) and Overduin et al. (2019) adapted by G. Fylakis for the NUNATURYUK project in collaboration with GRID Arendal, 2020.*

## 2.2 Yedoma permafrost

The Yedoma permafrost is a late Pleistocene Ice Complex, formed syngenetic under continental conditions in polygonal tundra with deposits up to 50 m thick. The Yedoma domain covers approximately 2 587 000 km$^2$ (11.3 % of the permafrost region) in Russia, Canada and Alaska, where estimated 480 000 km$^2$ of this domain is underlain by Yedoma deposits (Strauss et al. 2021b). Yedoma deposits are fine-grained, organic-bearing and ice supersaturated (50 – 95 %) permafrost soils with large syngenetic ice wedges, segregated ice lenses

and sub horizontal ice bands (Strauss et al. 2012; Schirrmeister et al. 2013; Schirrmeister et al. 2020). Yedoma formed polygenetic due alluvial, fluvial and niveo-aeolian transport, ponding water accumulation, frost weathering and post-depositional processes with syngenetic ice growth, determined by local conditions (Schirrmeister et al. 2020). Due the high amount of ground ice, Yedoma is very extremely vulnerable to permafrost degradation and disturbances (Section 2.3) (Strauss et al. 2017).

## 2.3 Permafrost degradation, thermokarst and coastal erosion

Permafrost soils are highly sensitive to climate, thus natural or artificial disturbances lead to the degradation of permafrost resulting in a decrease of permafrost thickness or areal extend (Jorgenson 2013). The disturbances can be categorized into (1) presses; impacts due changes on a decadal to century-scale as top-down thaw (active layer deepening), paludification, aridification or changes in the vegetation structure, and (2) pulses; abrupt changes due one-time or episodic short-term events, as wildfires, thermokarst, flooding or rapid soil erosion, which can trigger each other (Grosse et al. 2011).

Thermokarst is the most abundant and recognisable process of permafrost degradation. It results of the thawing of ice-rich permafrost or the melting of excess ice, leading to surface settlement. The initiation depends on hydrology, soil properties, vegetation, geomorphology and disturbance interactions (Grosse et al. 2011; Morgenstern et al. 2011; Jorgenson 2013). The resulting surface depression can be occupied by water, resulting in a thermokarst lake.

After the initiation, TLs grow, and potential coalesce by shoreline erosion and further thawing due downward and laterally heat flows and finally drain (partially or completely). The drainage can happen by a changing lake water balance or external factors as melting of ground ice, creation of a drainage pathway, headward gully erosion, river, lake or stream tapping, bank overtopping, coastal erosion or anthropogenic disturbances (Hinkel et al. 2007; Grosse et al. 2013; Jones et al. 2020b; Irrgang et al. 2022; Jones et al. 2022). The resulting DTLBs are optimal habitats for peat accumulation as vegetation can settle and in a cold climate, this basins can refreeze, followed by permafrost development (Jones et al. 2022).

A further consequence of thermokarst processes is the formation of taliks by local anomalies in thermal, hydrological or hydrochemical conditions (van Everdingen 2005). As they can also form sub-aerial due to wildfires or active layer adjustment to a new thermal regime when the summer thaw-depth exceeds the winter freezing-depth (Rey et al. 2020; Farquharson et al. 2022), TLs lead to the formation of sub-aquatic taliks under them and at their

margins, as they transfer heat from the water body into the underlaying ground, especially when the water depth exceeds the maximum thickness of winter ice cover (Burn 2002, 2005; Grosse et al. 2013).

Taliks are therefore thermal disturbances penetrating through permafrost, leading to fast thawing (Burn 2020; Rey et al. 2020; Ohara et al. 2022) and are thus crucial for the permafrost-carbon budget (Section 2.4). The resulting thermokarst landscape occupies ~20 % of the northern permafrost region, TLs and DTLBs are its most abundant recognisable form, with a two – three times higher area of DTLBs than TLs. Often, several TLs and DTLBs generations initiated during the transition between the Pleistocene and the Holocene and during the Holocene Thermal Maximum (11 – 5 ka BP) are present (Romanovskii et al. 2004; Grosse et al. 2013; Fuchs et al. 2019).

As the concentration of TLs and DTLBs increases with the proximity to the coast (Hussey and Michelson 1966), the ACP is strongly influenced by the sea. 34 % of the earth's coasts are affected by permafrost and/or seasonal sea ice cover (Lantuit et al. 2012) and therefore highly influenced by sea-level rise and coastal erosion, which is mainly driven by mechanical thermo-abrasion from wave action and thermo-denudation from insolation and summer warmth (Aré 1988a, 1988b). This leads to a transition from a terrestrial to a marine environment. As the coastal permafrost soils get occupied by the sea, salty seawater inundates them and changes the biogeochemical properties and the mobilization potential of OM into the Arctic ocean (Tagliapietra et al. 2009; Creel et al. 2024; Jenrich et al. 2025).

## 2.4 Permafrost and carbon

Permafrost carbon is the carbon stored in soils of the northern circumpolar region and in mountain permafrost regions (Schuur et al. 2013). The northern circumpolar region also contains C pools in subsea shelfs, originally terrestrial during the last ice ages, which have been little researched yet, but are highly valued (Miesner et al. 2023).

The permafrost is the largest terrestrial C pool, with ~ 30 % of the global C pool on land in only ~15 % of the area (Figure 5). An estimated 1 538 Gt C are stored in the terrestrial permafrost region, with alone 327 – 466 Gt contained in Yedoma deposits in Alaska and Siberia (Strauss et al. 2017; Strauss et al. 2025). A further 2 822 Gt C are expected in subsea permafrost soils (Miesner et al. 2023).

The main sources of C are plant litter inputs and microbial residues (Ping et al. 2015). Even so the C input is low, the much lower output due the cold and wet soil conditions on permafrost and the long deposition since the Pleistocene enabled this huge C pool. The C accumulation is determined by the landscape topography, vegetation, hydrology, permafrost conditions and the climate (Strauss et al. 2025). The low temperatures of the permafrost soils and the resulting impeding of water movement create a cold and wet environment and thus low decomposition rates due inhibited biochemical processes. The C is locked from the active carbon cycling and preserved like in a freezer for over thousands of years. The ongoing deposition, which buries the OM into deep permafrost deposits, recent peat accumulation which stores OM in the long-term in the soils, and cryoturbation (soil movement due thaw- and freeze-cycles), which relocates and redistributes OM into deeper layers of the perennial frozen soil, stabilize the OM and have led to the large C accumulation and storages in permafrost soils, as seen in Figure 5 (Schuur et al. 2008; Ping et al. 2015; Strauss et al. 2025).

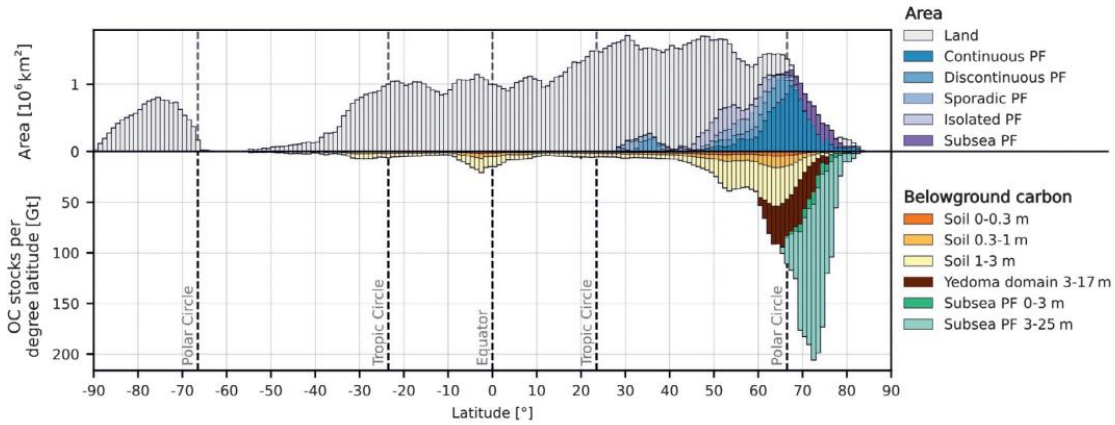


*Figure 5. Latitudinal distribution of belowground organic carbon in relation to land mass. Updated data from Poggio et al. (2021), Miesner et al. (2023) and Strauss et al. (2017, 2021b). Figure from Strauss et al. (2025).*

This stored OM can be decomposed by microorganisms, as it gets accessible and mobilized due thawing (of the surface layer and the subsurface due abrupt thawing events like thermokarst and talik formation) and erosion. Consequently, $CO_2$ and $CH_4$, depending on the hydrologic conditions, get released to the atmosphere. Thereby, permafrost C plays an essential role for the high-northern carbon cycle (Olefeldt et al. 2016).

Especially thermokarst is important for this budget (Heslop et al. 2015). Figure 6 shows schematically the carbon cycling in TLs and DTLBs. TLs emit high amounts of $CH_4$, especially in the initiation phase, originated from the thawed permafrost soils underneath and at the margins of the lakes (taliks) and decomposition of the young OM in the lakes, as well as due shoreline erosion (Walter et al. 2006; Kessler et al. 2012; Walter Anthony and Anthony 2013; Anthony et al. 2014; Heslop et al. 2015; Walter Anthony et al. 2016), followed by $CO_2$

sequestration in the later lake phases due sedimentation. Though it is unclear, if this compensates the GHG emissions. The formed taliks under and at the margins of the lakes can then reach and mobilize old, deep carbon that wouldn't be tapped with only gradual top-down thawing (Walter Anthony et al. 2018).

Anthony et al. (2014) estimated that 28 ± 12 % of the thawed C under permafrost lakes is converted into GHG over the lakes' millennial-scale lifespans. The C balance in DTLBs is still uncertain and strongly depends on the hydrologic conditions, vegetation, depth of the active layer and the time since drainage. DTLBs can act as a C source, especially shortly after the drainage by releasing $CO_2$ and small amounts of $CH_4$ due microbial decomposition. Since the basins favour peat accumulation and a fast succession from fen-type wetland to bog and tundra wetlands, they can then become a C sink, supplemented through new permafrost aggregation in a cold climate (Wickland et al. 2009; Anthony et al. 2014). The estimated C fluxes of DTLBs are one – three magnitudes smaller than in TKLs, with high $CO_2$ uptake offset and $CH_4$ emissions at the beginning, which declines with time (Walter Anthony et al. 2018; Zona et al. 2010; Zona et al. 2012; Treat et al. 2021; Jones et al. 2022). Thereby, thermokarst landscapes are a dynamic, uncertain component in the permafrost carbon budget, as they act as a C source through thaw and erosion processes on one hand and can

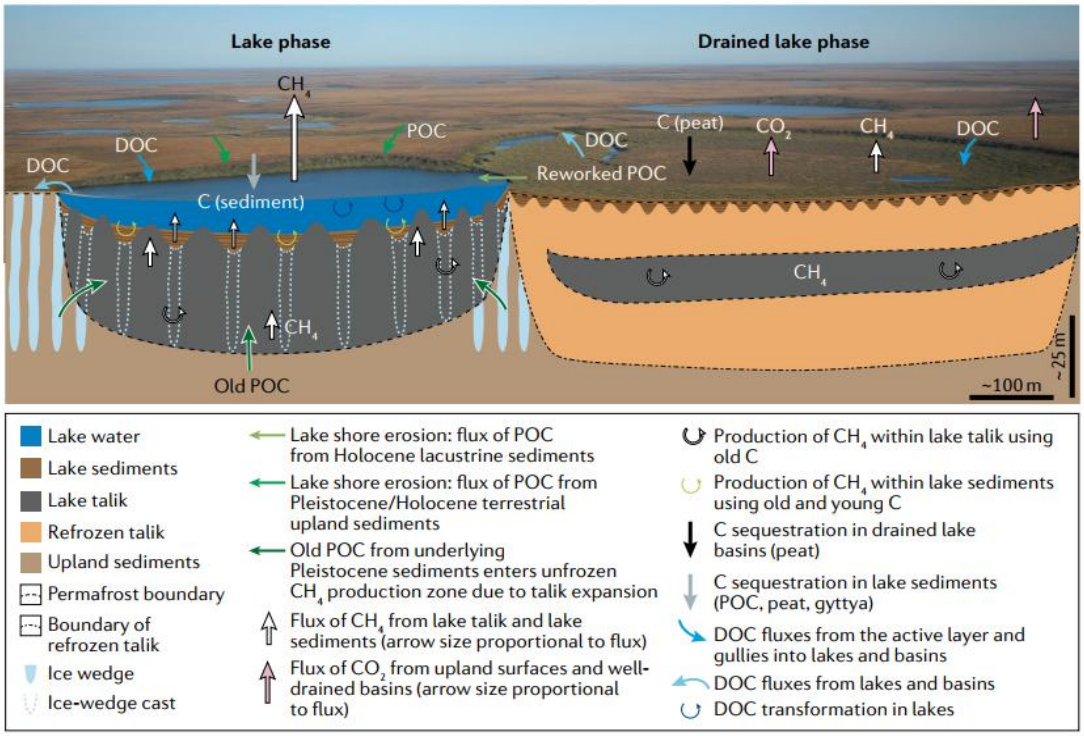


*Figure 6. Carbon cycling of a lake and drained lake basin system in lowland permafrost. Oblique aerial photograph of a thermokarst lake and drained lake basin in ice-rich permafrost on the northern Seward Peninsula, Alaska. Shown in cross section are idealized schematics of the underlaying talik and permafrost configurations associated with the lake and drained lake basin phases, and key surface and subsurface carbon (C) cycling components indicated by the arrows. Background image courtesy of Lawrence Plug, Figure by Jones et al. (2022).*

be a C sink in DTLBs on the other (Anthony et al. 2014; Fuchs et al. 2019).

## 2.5 Permafrost in a warming climate

Responding to climate warming, permafrost ground temperatures are on high records with increasing rates of up to 0.4 - 0.8 °C per decade since the 1980s (Smith et al. 2022). Between 2007 and 2016, the global permafrost temperatures have increased 0.29 ± 0.12 °C, with higher rates for the continuous (0.39 ± 0.15 °C) than for the discontinuous (0.20 ± 0.10°C) zone, indicating ongoing thawing and active layer thickening in the warmer regions as the heat is being absorbed by the phase change of ice to water, instead of directly rising the ground temperatures (Biskaborn et al. 2019). This is of particular concern as it mobilizes the stored OM due active-layer deepening, thermokarst development, riverbank and coastal erosion, thaw subsidence, forest and tundra fires (Strauss et al. 2025). The permafrost warming followed by gradual and abrupt thaw brings back the C into the active C cycling and enhances microbial decomposition causing $CO_2$ and $CH_4$ release into the atmosphere, which in turn causes further climate warming, called the "permafrost carbon feedback" loop, Figure 3 (Schuur et al. 2022). As a result, it is likely that the northern permafrost region transitions over the long term from a C sink to a C source, with substantial C losses after 2100 (McGuire et al. 2018). The sixth assessment report of the IPCC estimates the permafrost GHG feedback from $CO_2$ per degree of global warming at the end of the century is 18 (3.1 – 41) Gt C $°C^{-1}$ and 2.8 (0.7 – 7.3) Gt $CO_2$-eq $°C^{-1}$ for $CH_4$ (IPCC 2023b). Schuur et al. (2022) states that the thawing of terrestrial permafrost could release 5 – 15 % of its C pool during this century, leading to calculated net $CO_2$ and $CH_4$ (as $CO_2$ equivalents) emissions by 2100 of 55 – 232 Gt C-$CO_2$-eq. This is in the range of an industry nation as Russia, OECD, USA and China (scaled to 100 a), while these calculations do not yet include abrupt thaw processes as thermokarst, which could add another 40 % to the projections of C release (Schuur et al. 2022).

Previous studies found that the recent climate warming and rising permafrost temperatures have already led to an increase in the frequency and magnitude of thermokarst (Fedorov et al. 2014; Lantz and Kokelj 2008; Jorgenson et al. 2006), and thus an increase in TLs and DTLBs, with the number of water bodies increasing by 10.7 %, while the area is decreasing due the drainage of large water bodies by 14.9 % (Jones et al. 2011). Further, Jones et al. (2022) states a shift from TLs to DTLBs. While DTLBs have under cold climate the potential of peat accumulation and refreezing and thus of acting as a net C sink, the future warming inhibits this permafrost re-aggregation and causes persist taliks, which can mobilize old and

deep permafrost carbon, contrary to active-layer deepening, which mostly impacts shallow, young carbon (Jones et al. 2022; Parazoo et al. 2018). Additionally, warming permafrost and thus subsiding permafrost landscapes are accelerating the coastal erosion ( Biskaborn et al. 2019; Lim et al. 2020; Jones et al. 2020a). This is among further factors as reduction of sea-ice extent and increasing open water period duration (Perovich et al. 2020), rising air and water surface temperatures (Ballinger et al. 2020; Timmermans and Labe 2020), sea-level rise (Moon et al. 2020) and stronger wave action (Casas-Prat and Wang 2020), resulting in some of the highest coastal erosion rates on Earth with up to 47 m $a^{-1}$, as seen in Figure 7 (Irrgang et al. 2022).

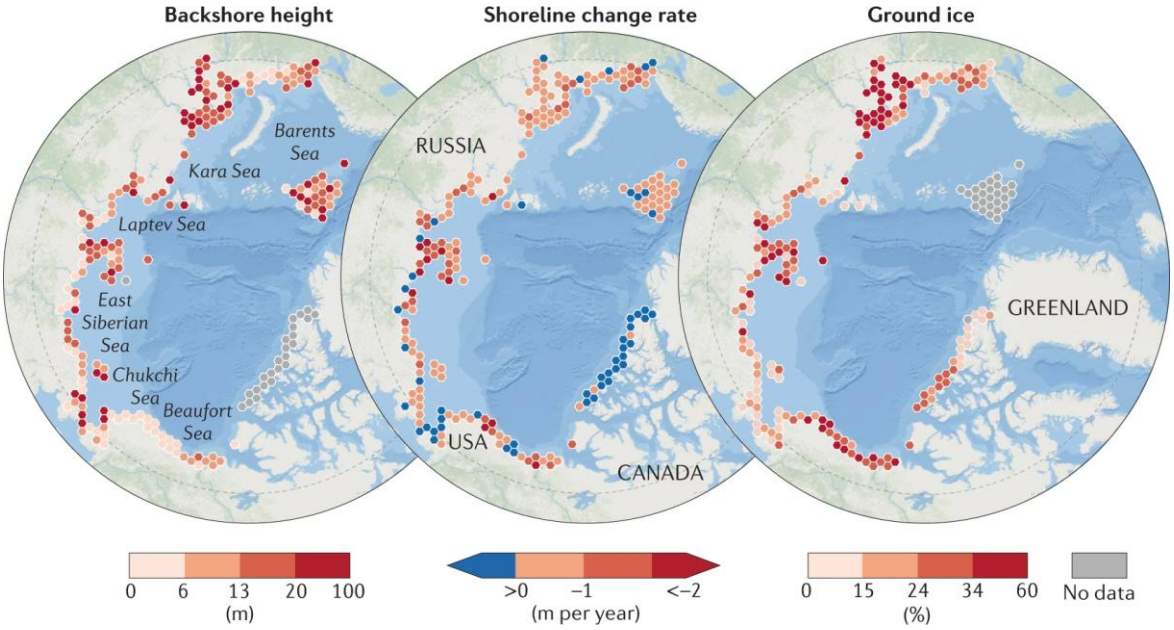


*Figure 7. Change of Backshore height, shoreline change rate and ground ice content along the Arctic coast. Data used from the Arctic Coastal Dynamics database (Lantuit et al. 2020) and summarized over a 100 * $10^3$ m extent. Figure from Irrgang et al. (2022).*

Creel et al. (2024) found that under medium emission scenarios, the Arctic coastline will loss 6 638 $km^2$ of land due erosion, permafrost subsidence and sea-level rise by 2100. Respectively, the estimated OC disturbance is 0.453 Gt. Also, taliks are expected to highly increase in frequency and extend, e.g. Parazoo et al. (2018) simulated that from 2100 to 2300, taliks will widespread form in the northern high latitudes, followed by a C sink-to-source transition. In the discontinuous zone, taliks will form across up to 70 % of the area by 2030 and reach thicknesses of 12 m by 2090. Figure 8 shows this C source to sink transition.

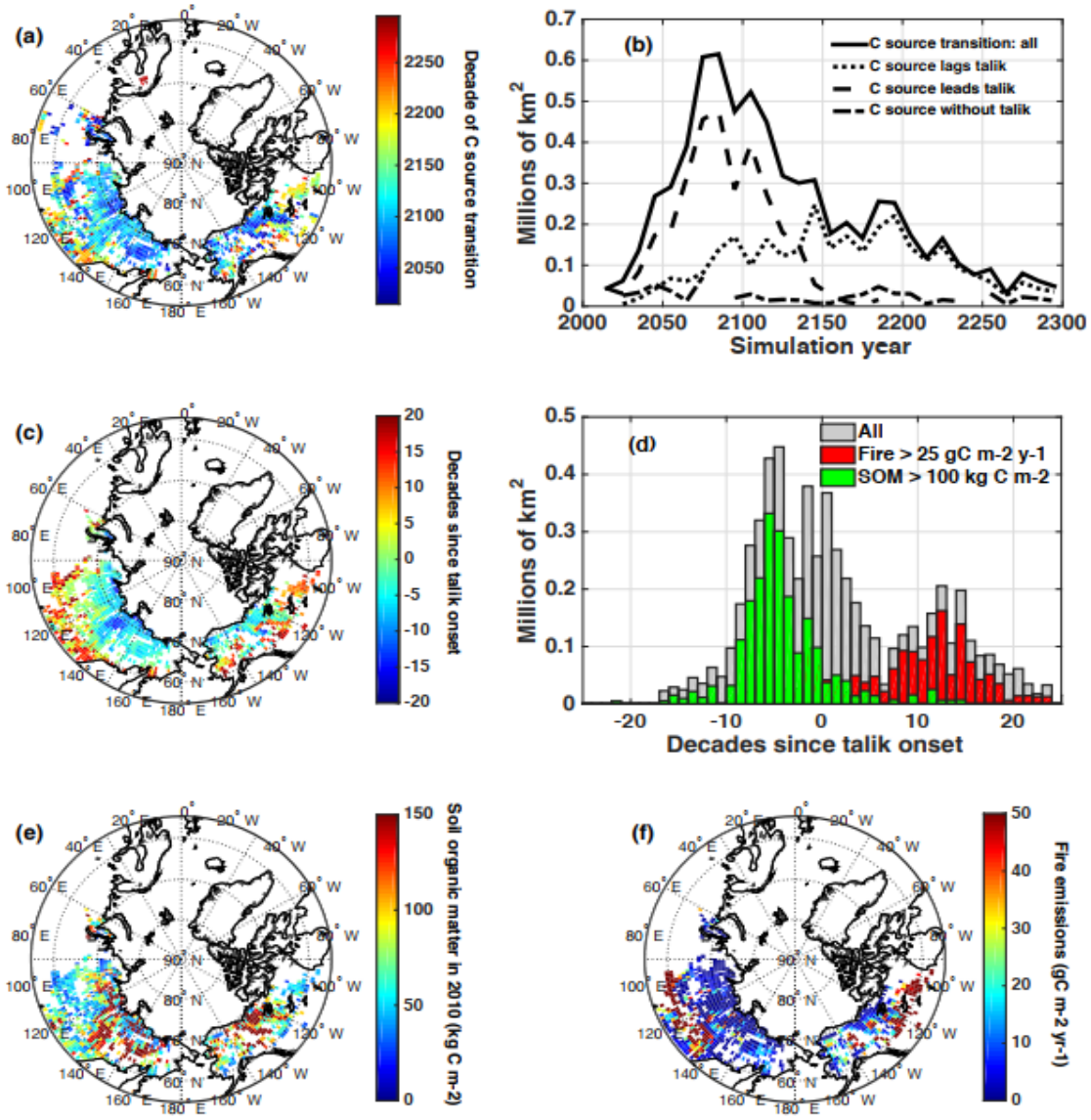


*Figure 8. C sink to source transition from 2010 to 2300 in relation to talik onset, soil C, and fire emissions under a Representative Pathway 8.5 warming scenario through 2100 and an Extended Concentration Pathway 8.5 through 2300. (a) Map of the decade of shift to C source. (b) Land area that transitions in the late 21st century and is driven by regions where the C source leads talik onset (dashed). (c) Decadal time lag from talik onset to C source shift. (d) Trimodal distribution of permafrost area as a function of decadal time lag (negative lags related to high soil organic matter (green bars and map in e) and large positive lags related to fires (red bars and map in f). Figure from Parazoo et al. (2018).*

# 3. Study area

## 3.1 Regional setting

The study area is located near Kotzebue (Qikiqtaġruk), on the north coast of the Baldwin Peninsula in north-west Alaska, surrounded by Kotzebue Sound. It is in the continuous permafrost zone, near the transition into the discontinuous zone (Jorgenson 2013; Obu et al. 2019) and part of the Bering Land Bridge (Nitze et al. 2020). The region is characterized by a subarctic continental climate with a mean annual air temperature of -4.4 °C and 289 mm annual precipitation (Kotzebue Climate station, Station USW00026616, NOAA, 1991 – 2020). The average snowfall accumulation is 163 cm $a^{-1}$, with snow persisting until middle to end of May (Macander et al. 2015). The measured ground temperatures range between -3.53 and -0.8 °C (Biskaborn et al. 2019).

The Baldwin Peninsula is a middle Pleistocene push-moraine complex at elevations from sea level to ~50 m a.s.l. with marine, fluvial and glaciogenic sediments, partly covered by loess deposits, formed during the Anaktuvuk River glaciation 500 to 600 ka BP. The region is underlain by ice rich (> 40 vol%) Yedoma permafrost with large syngenetic Pleistocene ice wedges as well as signs of strong degradation (Karlstrom 1964; Huston et al. 1990; Jorgenson et al. 2008; Jones et al. 2011; Jones et al. 2012; Jongejans et al. 2018).

It contains to the major lake districts of Alaska with lakes mostly in DTLBs from previous lake generations (Arp and Jones 2009; Jones et al. 2011; Jongejans et al. 2018; Nitze et al. 2020). The vegetation is dominated by a shrubby tundra (Walker et al. 2005) with floating vegetation on the lake margins and above water(Parsekian et al. 2011).

## 3.2 Sampling transect

This study covers a transect of ~1600 m from the inland to the coast with the four landscape units Yedoma upland (UL), thermokarst lake (L), drained lake basin (DLB) and marine (M), with elevations between 0 and 35 m a.s.l. shows the digital elevation model of the study area with the four sampling sites. The drained lake basin is a former Thermokarst lake on the Schaeffer-Tessier Family Native allotment (Illivak) near Kotzebue. It is originally made up of two lakes which coalesced till 1974 and increased with expansion rates of 0.25 – 0.35 m $a^{-1}$ up to an area of 0.54 ha in 2021 and bank heights of 2 – 4 m. The estimated average depth before the drainage is 3 – 4 m, the estimated mean permafrost thaw subsidence magnitude due active sub-lake thermokarst processes 6.5 m (Jones et al. 2023).

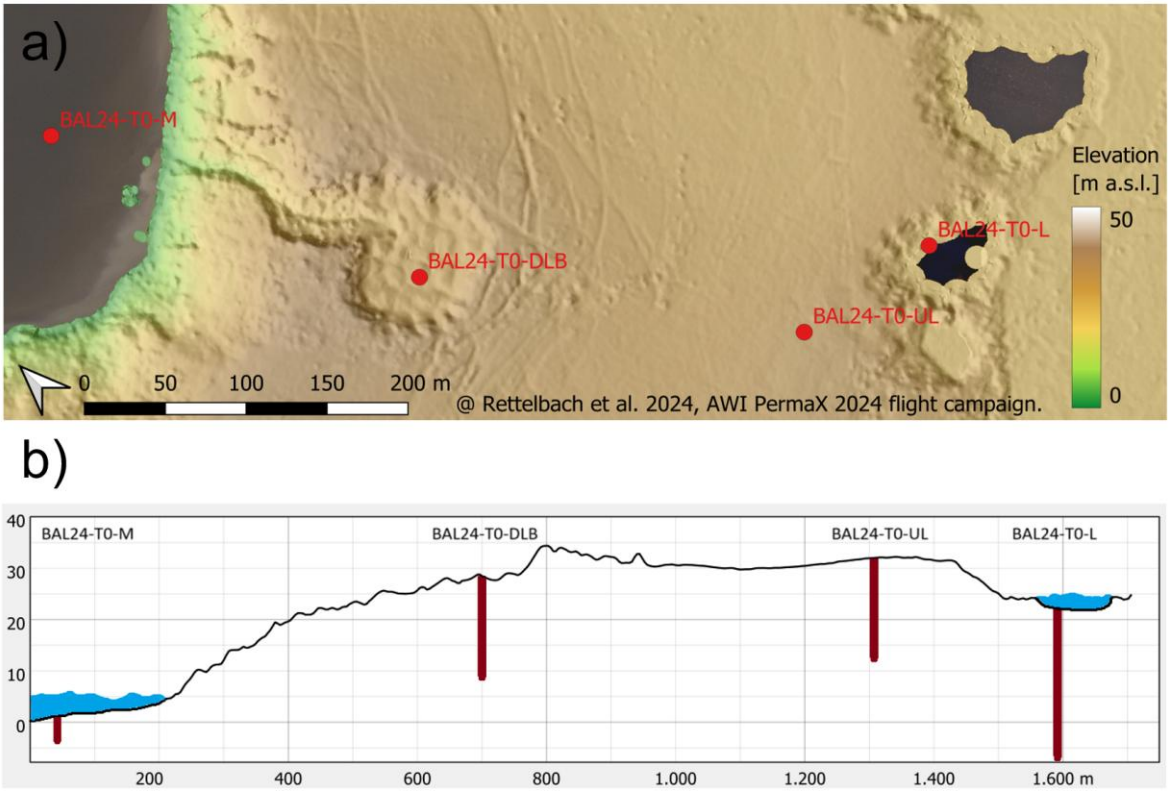


*Figure 9. (a) Digital elevation model and (b) horizontal profile of the study transect showing the marine site, the drained lake basin, the upland and the thermokarst lake. Core lengths are in the scale 1:10. Data from the AWI PermaX 2024 flight campaign (Rettelbach et al. 2024). Created with QGIS (QGIS Developement Team 2024).*

The drainage took place on 29th June 2022 and could be observed with the Native Tribal Health Consortium's LEO Network (Tessier et al. 2022). The resulting drainage tunnel, Figure 10, is 125 m long and eroded up to 14 m into the ice-rich permafrost, releasing estimated 18 500 $m^3$ water and 8 500 $m^3$ material through erosion and thaw into Kotzebue Sound. As beavers were present the days before and strongly influence thermokarst lake dynamics, they likely highly contributed to the drainage (Jones et al. 2020c; Jones et al. 2023).

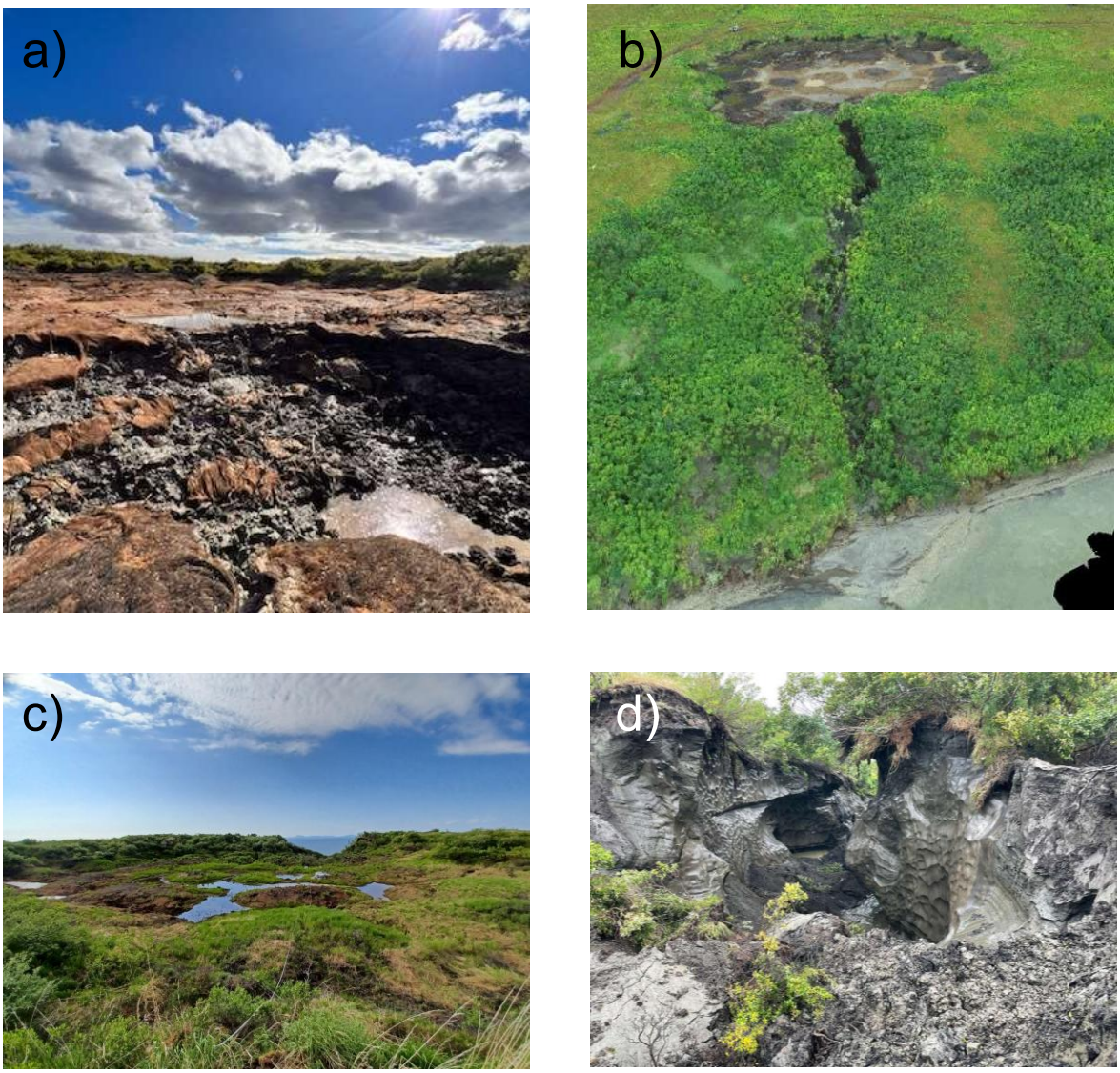


*Figure 10. (a) The drained lake basin after the drainage, picture by Susan Tessier, (b) a drone photo by Ben Jones from the drained lake basin with its gully in summer 2022, (c) the drained lake basin in summer 2024, picture by Maija Marushchak, and (d) the erosion gully in summer 2024, picture by Lutz Schirrmeister.*

# 4. Methods

To answer the research questions regarding the environmental history, OM sources, quantity and quality and its development due degradation, this study involved fieldwork, laboratory work and a statistical analysis.

## 4.1 Fieldwork

The field work took place in March 2024 during the AK-Land_2024_NWAlaska_spring Expedition (07.03.2024 – 28.03.2024) near Kotzebue on the Baldwin Peninsula, Northwest Alaska, led by Jens Strauss, as a collaboration of the University of Alaska Fairbanks and the Alfred Wegener Institute Helmholtz Centre for Polar and Marine research (AWI). For this master thesis, four cores under different landscape conditions (Table 1) were drilled on a transect from the inland to the coast (Figure 9). All sites were covered with a layer of 0.5 – 28.5 cm snow. The thermokarst lake (BAL24-T0-L) and marine site (BAL24-T0-M) were also covered by ice and water. The depth of the lake was 5.76 cm (1.26 cm ice and 4.5 cm liquid water), the ice on the marine site was 92 cm thick with 21 cm liquid water beneath. For the two frozen cores from the upland and the drained lake basin (BAL24-T0-UL and BAL24-T0-DLB), a "Snow-, Ice- and Permafrost-Establishment" (SIPRE, Ø 7.5 cm) was used. The unfrozen cores were drilled with a Vibracoring-system (WINK Vibracorer, Ø 7.5 cm) for the BAL24-T0-L and a Push Corer (Ø 7 cm) for BAL24-T0-M. The Cores BAL24-T0-UL and BAL24-T0-DLB were packed into whirlpacks and core foil, BAL24-T0-L in an aluminium tube, BAL24-T0-M in a plastic tube. They were labelled and stored below 0 °C in styrofoam boxes for the transportation to AWI Potsdam, where they were stored at around -20 °C until further analysis.

*Table 1. Characteristics of the four sites.*

| Sample ID | Landscape unit | Coordinates | Core length [cm] | Sample number | Coring device |
|---|---|---|---|---|---|
| BAL24-T0-UL | Upland permafrost ground | 66.903288°N, 162.508495°W | 213 | 39 | SIPRE (Ø 7.5 cm) |
| BAL24-T0-L | Thermokarst lake ground | 66.903148°N, 162.506359°W | 311 | 61 | VIBRA (Ø 7.5 cm) |
| BAL24-T0-DLB | Drained thermokarst lake basin | 66.905016°N, 162.511771°W | 214 | 42 | SIPRE (Ø 7.5 cm) |
| BAL24-T0-M | Marine ground | 66.907028°N, 162.513997°W | 55 | 12 | PUSH (7 cm) |
| Total | | | | 155 | |

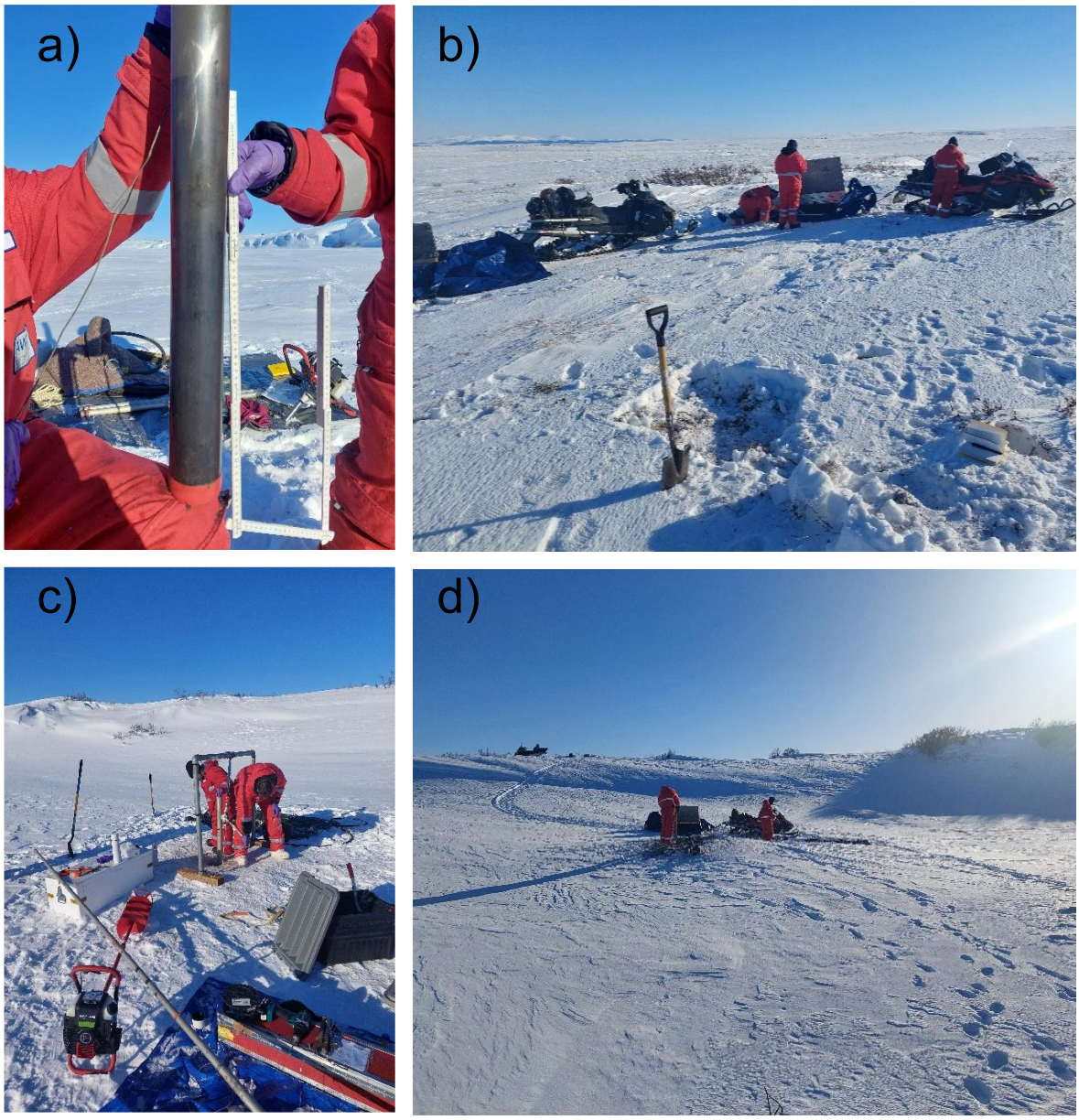


*Figure 11. Impression of the field work during the AK-Land_2024_NWAlaska_spring Expedition. (a) The marine core, BAL24-T0-M, (b) the upland study site, (c) the procedure of the virbracoring at the thermokarst lake site and (d) the drained thermokarst lake basin; Images from Fabian Seemann.*

## 4.2 Laboratory analysis

A multi-proxy approach was used for answering the different objectives, containing geochronology and sedimentology, biogeochemistry and hydrochemistry and n-alkane biomarker analysis. Figure 12 shows a schematic of the laboratory work.

The cores were subsampled in a climate chamber with around -8 °C. They were cut in half lengthwise with a band saw, resulting thawed and refrozen material was removed with knives. Afterwards the profiles were photographed and described sedimentological and cryolithological according to French and Shur (2010). One core halve was packed in core foil

and whirlpacks for the archive. The other was subsampled in approximately 2 – 10 cm increments for laboratory analyses, according to their cryostructure. From each core, three to five samples from the upper, middle and lower parts were taken for the biomarker analysis. The subsamples were then packed in labelled whirlpacks, respectively pre-burned, weighted

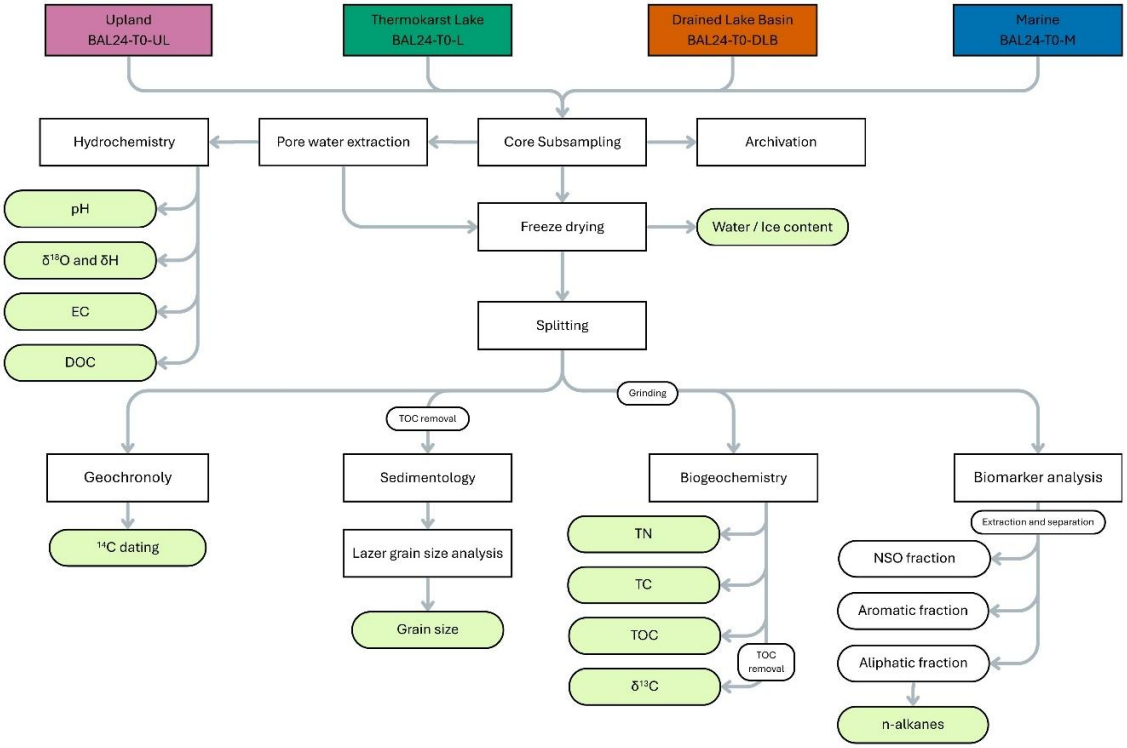


*Figure 12. Flowchart of the used laboratory methods.*

glass jars for biomarker analysis, weighted, and stored at -20°C. Figure 13 shows the subsampling of BAL24-T0-UL in the climate chamber at AWI.

A total of 155 samples was obtained for sedimentology and biogeochemistry analysis, from which 63 were additionally analysed for hydrochemistry, 14 for geochronology and 20 for biomarker analyses.

## 4.2.1 Hydrochemical analysis

63 of the subsamples were analysed for the hydrochemical parameters electrical conductivity (EC), pH-values, dissolved organic carbon (DOC) and stable water isotopes ($\delta^{18}O$ and $\delta D$). Investigating the properties of the porewater is key to understand the hydrochemical composition of the OM and the paleoenvironmental conditions as temperature, origin of water and genesis processes.

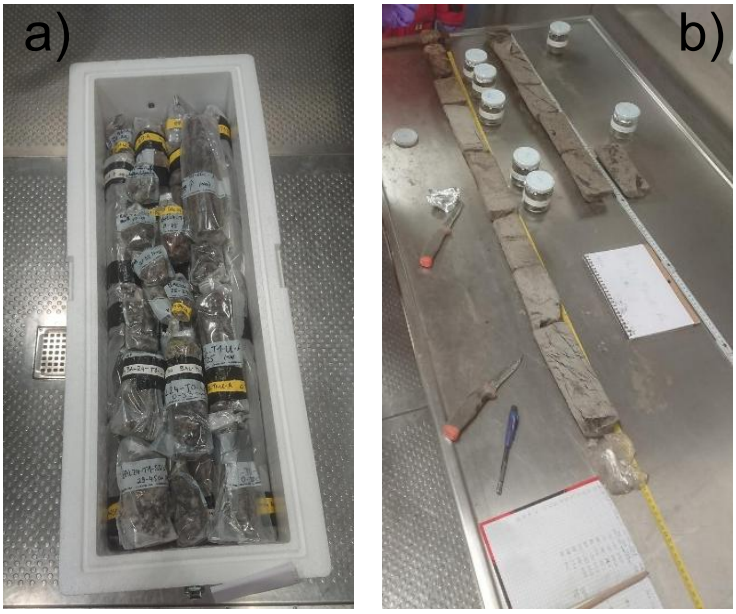


*Figure 13. (a) Transported cores stored in whirlpacks and (b) cryolithological description and subsampling of BAL24-T0-UL in the climate chamber at AWI Potsdam.*

#### 4.2.1.1 Porewater extraction

For the porewater extraction, the samples were thawed at 6 °C in the whirlpacks. Rhizomes (*RHIZONS MOM 5 and 10 cm, Rhizospheres Research Products*) were inserted into the samples and taped airtight. Then a 30 mL syringe was stacked on the rhizomes and filled with the porewater by drawing up and creating a vacuum in the whirlpack for 1 – 1.5 h (Figure 14). The extracted porewater was injected into labelled glass bottles. This procedure was repeated three – five times.

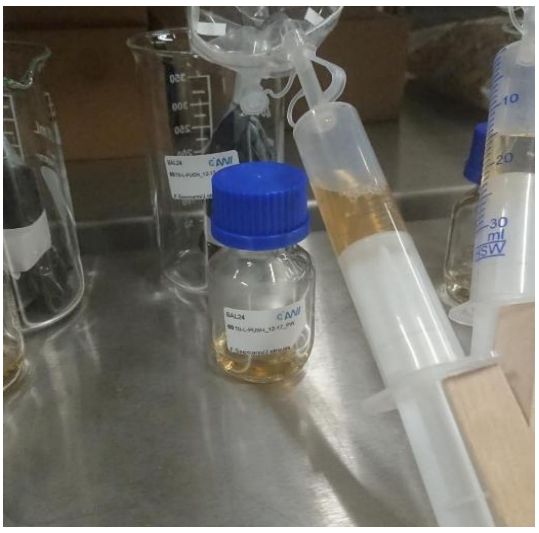

*Figure 14. Porewater extraction.*

### 4.2.1.2 Electrical conductivity and pH-value

The EC reflects the concentration of dissolved ions in the porewater. It can serve as an indicator of mineralization of the OM and thus the degradation of permafrost, as well as hydrological processes and the marine influence, as ions and salts get released into the porewater due permafrost degradation. Also repeated thaw-freeze processes can lead to an ion concentration, for example at the thawing front. The pH-value influences chemical processes and can provide information about the microbial activity and solubility of organic matter; low pH-values can limit decomposition rates (Grosse et al. 2011). As the analysis of the pH-value changes the chemistry of the porewater, it is essential to first measure the electrical conductivity. The analysis was carried out with 3 mL of the extracted porewater in a *Seal Analytics*, *Orion Versa Star Pro* laboratory robot

### 4.2.1.3 Oxygen and hydrogen isotopes

The stable water isotopes are the ratio of $^{18}O/^{16}O$ for $\delta^{18}O$ and $^{2}H/^{1}H$ for $\delta D$, respectively. As the chemical reaction or phase transition of water leads to a fractionation of the isotopes, and therefore a change in the isotopic ratio, they can be used to indicate the temperature, evaporation or moisture source of the water when infiltrated into the soil. E.g. clouds consist of the lighter isotopes due their higher vapour pressure and lakes or the ocean of the heavier isotopes. Further, the isotope fractioning is temperature depending, whereby it can be used as temperature indicator.

For the stable water isotope analytics, around 10 mL of the cooled porewater was measured with a *Finnigan MAT Delta-S Mass Spectrometer*. The values were obtained by the average of two measurements. The results were expressed in permille (‰), using the internal Standard Mean Ocean Water (SMOW) as reference (Craig 1961):

$$\delta_{sample,\ SMOW} = \left(\frac{R_{sample}}{R_{SMOW}} - 1\right) * 1000, \qquad (1)$$

where $R_{sample}$ and $R_{SMOW}$ are the isotopic ratios in the sample and SMOW reference and $\delta_{sample,\ SMOW}$ is the isotopic abundance in the sample relative to SMOW (Craig 1961).

### 4.2.1.4 Dissolved organic carbon content

The dissolved organic carbon (DOC) reflects the microbial activity and the release of OM into the environment (high = high availability, low = low mobility and stable conditions). The DOC was measured as non-purgeable organic carbon (NPOC, direct method) under the

assumption that no significant volatile organics were in the sample. For this, 10 mL of the porewater was acidified with 50 µL of 30 % hydrochloric acid (HCL) to convert the inorganic carbon (IC) component into $CO_2$ via carbonic acid. Afterwards the $CO_2$ is removed from the sample solution by purging and DOC is directly measured as NPOC by oxidation at 680 °C followed by detection. For the analysis, 10 mL of the porewater was mixed with 50 µL of 30 % HCL to preserve the samples until the measurement. The measurement was carried out with a *Shizmadzu TOC-VCPH*, the results of three to five injections were averaged. The detection limit was 0.3 mg $L^{-1}$.

## 4.2.2 Sedimentological analysis

For further analysis, all samples were freeze-dried (*Zirbus Sublimator*) at -40 °C and 0.02 MPa for 48 h and then weighted again. The water / ice content and grain size were measured for the sedimentological analysis.

### 4.2.2.1 Water / Ice content

The absolute water / ice content was obtained due the weight difference between the frozen and the freeze-dried samples after Equation ( 2 ):

$$abs.water\ content\ [wt\%] = \frac{m_w - m_d}{m_w} * 100, \qquad (2)$$

where $m_w$ is the netto wet weight [g] and $m_d$ the netto dry weight [g].

### 4.2.2.2 Grain size analysis

The grain size and its distribution give information about the transport medium and the mechanism of deposition during the sedimentation. This is important to reconstruct the sedimentological and depositional history of the study site. Further, the grain size influences soil properties and is therefore important for interpreting the biogeochemical results.

For preparation of the grain size analysis, samples with to high peat content were separated out and the OM of the remained samples was removed via oxidation. Therefore, 100 mL of 3 % hydrogen peroxide ($H_2O_2$) and 2 – 3 drops of 25 % ammonia ($NH_3$) were added to the freeze-dried samples. They were then placed on a shaker, which got slowly heated up to 60 °C after a few days, for ~4 weeks to allow all OM to react (Figure 15). 4 – 5 times a week, further 10 mL 30 % $H_2O_2$ was added, as well as ammonia or acetic acid to ensure the pH remains at near-neutral (6 – 8).

After all organic material reacted, the samples were washed out with purified water to remove the $H_2O_2$, centrifuged (*Heraeus Multifuge 3s, Heraeus Cryofuge 8500i, Heraeus Megafuge 40*) to remove supernatant liquid, freeze-dried and then manually homogenized. Approximately 1 g of the samples were mixed with 0.5 g dispersing agent (tetra-sodium pyrophosphate, $Na_4P_2O_7$) and 0.0001 % ammonia solution ($NH_3$) in a plastic jar and shaken (*RS12 Rotoshake, Gerhardt)* for at least 24 h for complete dispersion. The samples were then divided into 8 subsamples with a particle concentration of 5 – 15 % with a rotary cone sample divider (*Laborette 27, Fritsch*). To prevent damages on the laser, particles >1 mm were sieved, weighted and afterwards included in the grain size distribution, if the proportion was significant compared to the total sample.

The grain size analysis was carried out with a *Malvern Mastersizer 3000* laser. This measures the light impulses on multiple scatter light detectors after particle refraction due a red laser (633 nm) and a blue light emitting diode (470 nm). Three measurements per subsample were taken and the results averaged. The grain size statistics as the mean, mode, sorting and skewness were calculated after Folk and Ward (1957) with the software GRADISTAT v 8.0 (Blott and Pye 2001), using geometric scaling after the international ISO 14688-1:2017 (ISO 2017), with clay ≤ 2 µm, silt 2 – 63 µm and sand 63 µm – 2 mm.

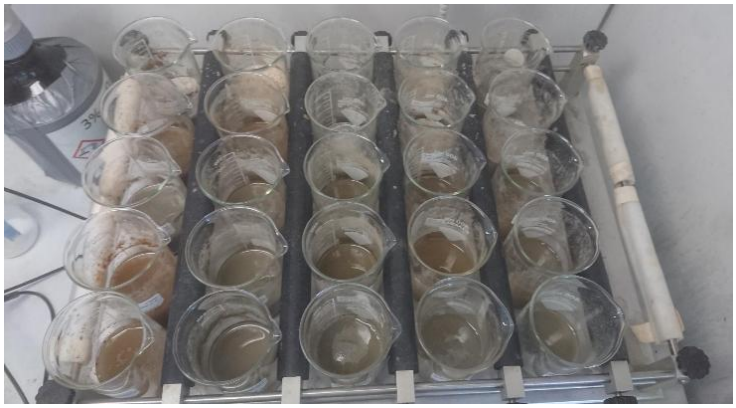

*Figure 15. Sediment samples on the shaker.*

## 4.2.3 Geochronology

Radiocarbon dating uses the decay of the radioactive carbon isotope $^{14}C$ into $^{14}N$ to determine the age of an organism. During live, the $^{14}C$ concentration in an organism remains in equilibrium with the environment, while after death, the original $^{14}C$ content decays with 5 700 ± 30 a as half-life time and thus the remaining content of $^{14}C$ indicates the time since death (Hajdas et al. 2021).

14 of the samples were selected for geochronology. The freeze-dried samples were picked

for macrofossils as leaves and branches under the microscope. The radiocarbon age was determined using the accelerator mass spectrometer *MICADAS* (*MIni CArbon Dating System, Ionplus*) at AWI Bremerhaven. To obtain a chemically unmodified fraction of the samples, they were pre-treated with the acid-base-acid (also known as acid-alkali-acid) treatment to remove contaminants as carbonates, organic acids and dissolved atmospheric carbon dioxides (Vries and Barendsen 1954; Mollenhauer et al. 2021). The samples were converted into $CO_2$ by combustion at 950 °C with an elemental analyser (*Elementar vario Isotope*), graphitized with an automated graphitization system (*AGE-3; Ionplus AG*) and then pressed into cathodes via pneumatic press, which were inserted into the linear magazine for measurement (Mollenhauer et al. 2021). The detection limit was >50 ka BP.
Afterwards the calibration software *CALIB 7.1* (Reimer et al. 2013) was used to express the determined radiocarbon ages in calibrated kilo years before present (cal. ka BP).

## 4.2.4 Biogeochemical analysis

The biogeochemical analysis gives important information about the characteristics of the OM, as the degree of decomposition and the vulnerability, as well as about the paleoenvironmental conditions. For this, the freeze-dried samples were homogenized by grinding (*Pulverisette 5 planetary mill, Fritsch*) for the further analysis.

### 4.2.4.1 Total organic carbon and nitrogen

The elemental analysis bases on combusting chromatography. For the carbon fractions, two 50 mg sub-samples per samples were weighted into stainless steel capsules and measured with an elemental analyser (*ELEMENTAR soli ToC cube*, Figure 16a). Between the three

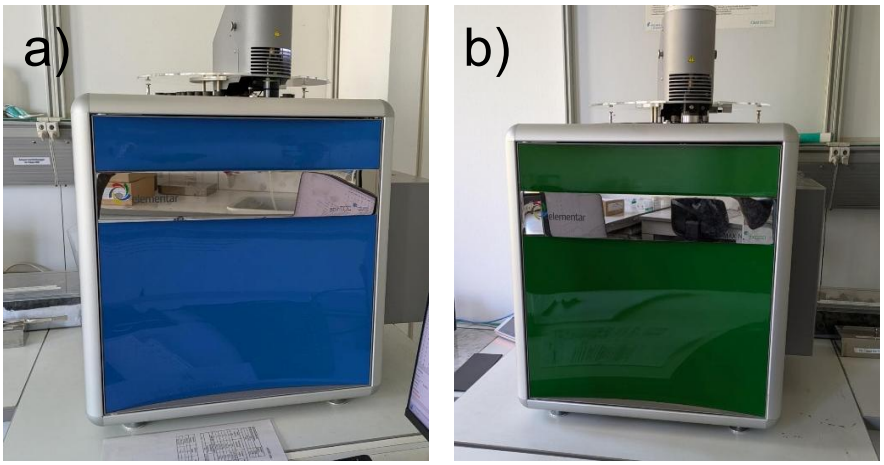


*Figure 16. (a) The Soli TOC cube and (b) the rapid Max N exceed.*

fractions total inorganic carbon (TIC), total organic carbon (TOC) and residual organic carbon (ROC) was distinguished with a temperature ramping method after DIN 19539 in a flow of oxygen-containing gas. With a heating rate of 70 °C $min^{-1}$, the sub-samples were heated to 400 °C for TOC (holding time 230 s), 600 °C for ROC (holding time 120 s) and finally 900 °C for TIC (holding time150 s).

Total nitrogen (TN) was measured with a *Rapid Max N exceed* (*Elementar*, Figure 16b) using the Dumas method (Buckee 1994). 50 mg of the samples were weighted into stainless steel capsules and heated up to 900 °C. Oxygen was introduced with a flow rate of 120 mL $min^{-1}$ for samples with a TOC content ~ 1 wt%, 140 mL $min^{-1}$ for a TOC content ~20 % and respectively 160 mL $min^{-1}$ for samples with a TOC content ~40 wt%. To detect background signals, blank capsules and calibration standards were included in the measurement for both procedures (

Table 2a for TOC and

Table 2b for TN). The detection limit of both analysers is <0.1 wt%.

*Table 2. Insertion and weighing-in instruction for soli TOC cube (left) and for Rapid Max N exceed (right).*

| Number of runs | Description | Weigh-in |
|---|---|---|
| 1x | RunIn | *set to 1 mg* |
| 2x | Blank | *set to 1 mg* |
| 3x | $CaCO_3$ 6% (TC 6 %) | 20 mg |
| 3x | IVA 2176 (TOC 15.57 %) | 50 mg |
| 1x | $CaCO_3$ 6% (TC 6 %) | 20 mg |
| 1x | $CaCO_3$ 12% (TC 12 %) | 15 mg |
| 1x | EDTA 5:45 (TOC 4.11 %) | 100 mg |
| 1x | IVA 2176 (TOC 15.57 %) | 50 mg |
| 15x (2) | Samples | 50 mg |
| | **Control block** | |
| 15x (2) | Samples | 50 mg |
| | **Control block** | |
| 2x | Blank | *set to 1 mg* |

| Number of runs | Description | Weigh-in |
|---|---|---|
| 1x | RunIn | *set to 100 mg* |
| 2x | RunIn (N 10.313 %) | *~250 mg* |
| 2x | Blank | *set to 100 mg* |
| 4x | EDTA 5:45 (N 0.960 %) | 50 mg |
| 1x | BS 1 (N 0.216 %) | 50 mg |
| 1x | BS 2 (N 0.064 %) | 50 mg |
| 1x | IVA 2150 (N 0.490 %) | 50 mg |
| 1x | IVA 2156 (N 1.360 %) | 50 mg |
| 36x (2) | Samples | 50 mg |
| | **Control block** | |
| 1x | Blank | *set to 100 mg* |

The measured TOC and TN content was further used to calculate C/N as the quotient of TOC and TN. This ratio is an indicator of degree of OM decomposition. A lower C/N indicates a higher a degree of decomposition, as the degradation changes the elemental composition of the OM components because carbon gets more removed than nitrogen during decomposition

(Kuhry and Vitt 1996; Schirrmeister et al. 2011b; Strauss et al. 2015). Furthermore, C/N can be used to distinguish the OM source, between algal (4 – 10) and land-plant (>20) input (Meyers 1994). As the source identifiers from Meyers (1994) are given in atomic C/N, they were converted into wt% with $C/N\ (wt\%) = C/N\ (atomic) * \frac{12.011\ u}{14.007\ u}$, were 14.007 u and 12.011 u are the atomic weights of N and C. This results in the values of 3.4 – 8.6 for aquatic algae and ≥ 17.1 for land plants. But as C/N is influenced by the grain size, with coarser fractions often include more visible plant remains, while finer, clay-rich fractions tend to have lower nitrogen levels because clay minerals can absorb ammonia and reduce its measurable concentration, it is important to use additionally indicators for the OM source, such as $\delta^{13}C$ or the biomarker proxies (Section 4.2.5.2) (Meyers 1994, 1997).

### 4.2.4.2 Stable carbon isotopes

The stable carbon isotopes ($\delta^{13}C$) are used to identify the source and decomposition state of the OM. Plants differ in their carbon isotope fractionation, e.g. marine (-22 to -20 ‰ vs. VDPB) vs. lacustrine and continental (~ -27 ‰ vs. VDPB) plants, allowing $\delta^{13}C$ to serve as a proxy for vegetation input, especially as it is compared to C/N not influenced by the grain-size (Meyers 1994, 1997). Furthermore, microbial decomposition preferentially uses the lighter $^{12}C$ isotope, resulting in less negative $\delta^{13}C$ values in more degraded material (Heyer et al. 1976). Thus, $\delta^{13}C$ values help to infer both past vegetation and the preservation state of OM in sediments.

The measurement of $\delta^{13}C$ was carried out with a *Finnigan MAT Delta-S* mass spectrometer combined with a *FLASH elemental analyser* and a *CONFLO IV* gas mixing system. To remove carbonate, samples were treated with 20 mL HCL (1.3 mol) and heated at 97 °C for 3 h prior measuring. Afterwards, the samples were washed with purified water to a neutral pH-value, filtered, dried at 50 °C and weighted in silver capsules depending on the sample TOC content (Equation ( 3 ).

$$target\ sample\ weight\ [mg] = \frac{20}{TOC\ [wt\%]} \qquad (3)$$

The sub-samples were combusted at 1020 °C in a $O_2$ atmosphere with chrome dioxide ($CrO_2$) as oxidant, to convert the OC into $CO_2$, which then was transferred to the mass spectrometer via the *CONFLO IV* gas mixing system. With the calculated ratio of $^{13}C$ to $^{12}C$, the $\delta^{13}C$ value was expressed in parts per thousand with the permille (‰) notation, using the internal standard Vienna Pee Dee Belemnite (VPDB), after equation ( 4 ):

$$\delta^{13}C_{sample,\ VPDB} = \left(\frac{I^{13}R_{sample}}{I^{13}R_{VPDB}}\right) - 1, \quad (4)$$

where $I^{13}R_{sample}$ and $I^{13}R_{VPDB}$ are the $^{13}C/\ ^{12}C$ ratios in the sample and VPDB reference and $\delta^{13}C_{sample,\ VPDB}$ is the isotopic abundance in the sample relative to VPDB (Hoffman and Rasmussen 2022).

### 4.2.5 Biomarker analysis

Biomarkers are characteristic molecular markers which contain important information about the OM origin and preservation. Thus, biomarker are a key indicator for paleoenvironmental reconstruction as well as proxies for the carbon source and biogeochemical processes as microbial degradation (Meyers 1997; Otto and Simpson 2005; Strauss et al. 2015). This study focuses on the aliphatic n-alkanes, lipids that contain of unbranched, long-chain hydrocarbons with mostly odd-carbon numbers. They are an important component of plant leaf-waxes and get preserved in sediments through deposition. The main source of these hydrocarbons in sediments are algae, bacteria and aquatic vascular plants within lakes, and terrestrial vascular plants (Meyers 2003). As they have a low sensibility to microbial degradation, n-alkanes are quite robust proxies for the organic matter source (Cranwell et al. 1987; Eglinton and Eglinton 2008; Zech et al. 2013). For the analysis of the lipid biomarkers, 20 samples were used: five from BAL24-T0-UL and BAL24-T0-DLB, seven from BAL24-T0-L and three from BAL24-T0-M.

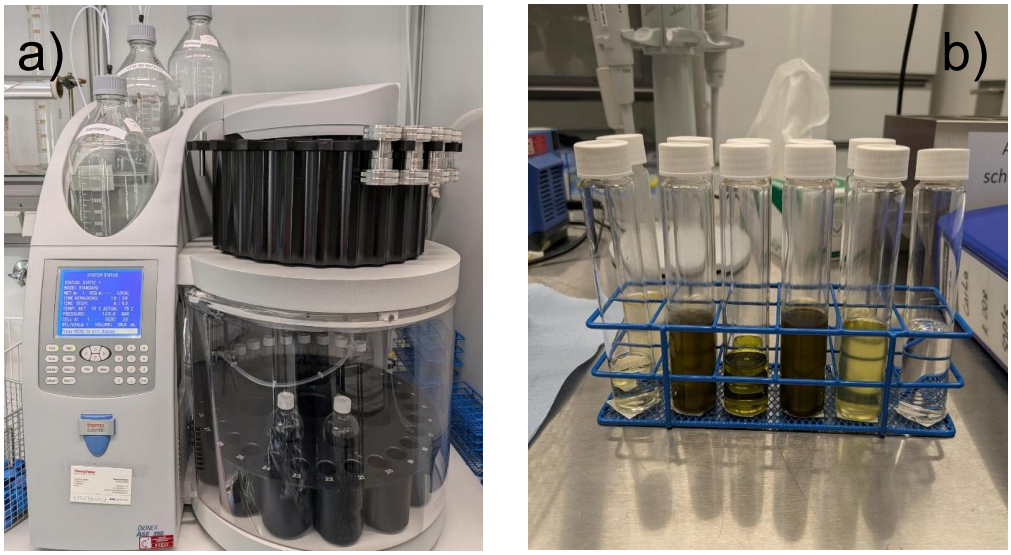


*Figure 17. (a) The ASE 350 extractor and (b) the dissolved compounds.*

### 4.2.5.1 Measurement

For the lipid biomarker analysis, samples were extracted with an accelerated solvent extraction (*ASE 350, Dionex*, Figure 17a), using a mixture of Dichloromethane and Methanol (DCM + 1%MeOH, 99:1) as extraction solvent. For this, approximately 8 g of freeze-dried and grinded sediments were weighted in the extraction cells. The samples were heated over 5 min to 75 °C, followed by a static phase of 20 min. The pressure was constant at 5 MPa. Afterwards the extraction (Figure 17b), the dissolvent compounds were concentrated with a Rocket Synergy vacuum evaporator (*Genevac SP Scientific*) at 42 °C and further dried by evaporation under a stream of nitrogen. For quantification of the compounds, 80 µL each of 4 internal standards with a concentration of 100 µg $mL^{-1}$ were added to the samples:

- 5α-androstane ($C_{19}H_{32}$) for aliphates
- ethylpyrene ($C_{18}H_{14}$) for aromatics
- 5α-androstan-17-on ($C_{19}H_{30}O$) for nitrogen-, sulfur-, oxygen- (NSO-) containing compounds
- eruic acid ($C_{22}H_{42}O_2$) for the NSO-fatty fraction

Afterwards, a large excess of n-hexane ($C_6H_{14}$) was added to remove the n-hexane-insoluble fraction ("Asphaltene precipitation") and the remaining n-hexane-soluble portion was separated into unipolar (aliphatic and aromatic hydrocarbons) and polar (hetero (NSO-) compounds) fractions using medium-pressure liquid chromatography (*MPLC, Köhnen-Willsch Chromatographie*, (Radke et al. 1980), Figure 18a). Therefore 300 µL of the samples dissolved in 1 ml n-hexane were injected into the MPLC, where the unpolar fractions were eluted with n-hexane, the polar with DCM.

The following measurement of the fractions was carried out with a gas chromatography-mass spectrometry (GC-MS, *Trace 1310 + ISQ 7000, Thermo Fisher Scientific*, Figure 18b).

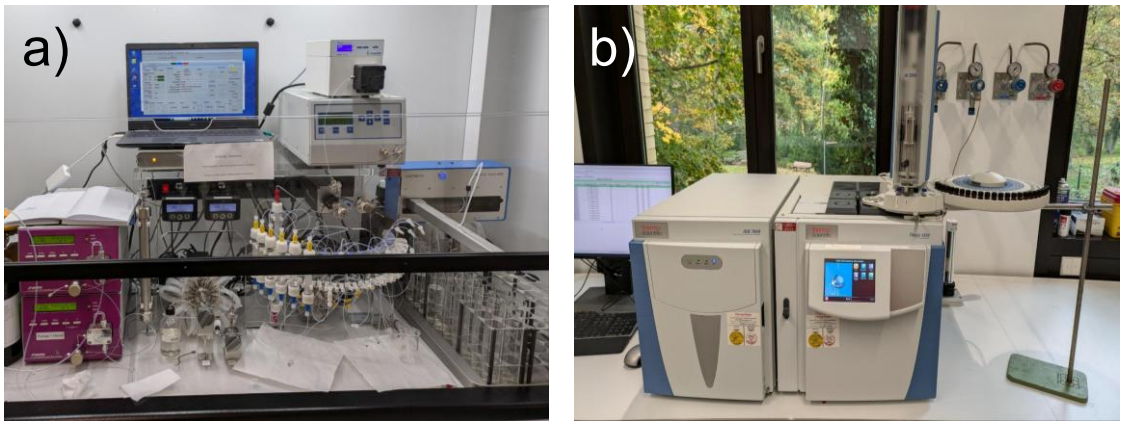


*Figure 18. (a) The MPLC and (b) the GC-MC.*

The samples were injected in the GC system and vaporized by heating from 50 °C to 300 °C with a heating rate of 10 °C min-1 and an isothermal holding time of 10 min, and then led trough a fused silica capillary column (SLB-5ms Sigma Aldrich, 60 m length, 0.25 mm diameter), using helium as carrier gas (constant flow of 1 mL/min). For the measurement, the GC was heated with a rate of 3 °C min-1 from the initial 50 °C to 310 °C, followed by an isothermal holding time of 30 min. For following compound analysis, the coupled mass spectrometer operated in electron impact ionization mode at 70 eV and 230 °C, recording a mass spectra m z-1 from 50 to 600 u at a scan rate of 2.5 scan s-1. The n-alkanes were quantified in the GC-MS chromatogram using the Xcalibur software (Thermo Fisher Scientific) by comparing the peak area of targeted compounds with the peak area of the internal standard (5α-androstane).

### 4.2.5.2 Biomarker Indices

Five biomarker indices were calculated from the n-alkane concentrations. They serve as proxies for (1) the quality (total long-chain alkane concentration and CPI), and (2) the aquatic vs. terrestrial influence and thus the source of the OM (ACL, $p_{aq}$ and $p_{wax}$).

#### Total long-chain alkane concentration

The total long-chain alkane concentration indicates the quality of the OM, with higher concentrations standing for a better quality, and was calculated as the sum of the whole range of detected long-chain n-alkanes ($C_{21\text{-}35}$):

$$Total\ alkane\ concentration_{C_{21-35}} = \sum C_i\ , \qquad (5)$$

where $i$ is the carbon number index and $C$ is concentration.

#### Carbon preference index

The carbon preference index (CPI) is the ratio of odd- to neighbouring even-numbered alkanes introduced by (Bray and Evans 1961), as a proxy of the degradation and alternation by quantifying the odd over even predominance of the carbon chains, as microbial degradation produces more even chains (Zech et al. 2013). Thus, high values reflect typically fresh, undegraded soils, whereas the lower, the more degraded the soil (Bray and Evans 1961; Marzi et al. 1993). The revised calculation by Marzi et al. (1993) and the interval $C_{23\text{-}33}$ was used:

$$CPI_{C_{23-33}} = \frac{\sum odd\ C_{23-31} + \sum odd\ C_{25-33}}{2 * \sum even\ C_{24-32}}, \quad (6)$$

where $n$ is the starting dominating chain length/2, $m$ is the ending dominating chain length/2, $i$ is the index of the carbon number, and $C$ is the concentration.

## Average chain length

The n-alkane average chain length (ACL) is calculated by the concentration-weighted sum of the different carbon chain lengths, introduced by Poynter and Eglinton (1990). While long-chain n-alkanes are typical for higher plants, with grasses and herbs dominated by 31 and 33 carbon atoms and trees and shrubs by 27 and 29 carbon atoms, short-chain n-alkanes are typical for bacteria and algae (Poynter and Eglinton 1990; Ficken et al. 1998; Zech et al. 2010; Zech et al. 2013), as seen in Figure 19. We used the long-chain interval $C_{23-33}$:

$$ACL_{C_{23-33}} = \frac{\sum i * C_i}{\sum C_i}, \quad (7)$$

where $i$ is the carbon number index and $C$ is the concentration.

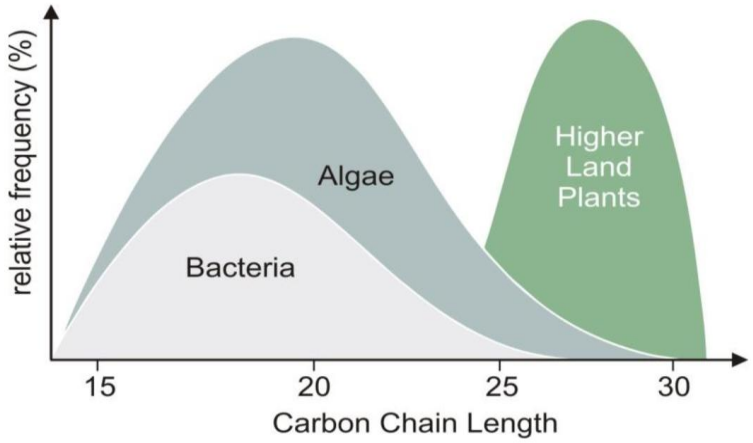


*Figure 19. Relative frequency of n-alkane chain-length in bacteria, algae and higher land plants. From Strauss et al. (2015), modified after Killops and Killops (2009).*

## Aquatic organic matter proxy

The aquatic OM proxy $p_{aq}$ was developed by Ficken et al. (2000) as followed:

$$P_{aq} = \frac{C_{23} + C_{25}}{C_{23} + C_{25} + C_{29} + C_{31}} \quad (8)$$

and can be used to indicate the aquatic influence of plant inputs by the relative proportion of mid-chain length to long-chain length homologues with values for submergent and floating plants > 0.4, emergent plants 0.1 – 0.4 and terrestrial plants < 0.1 (Ficken et al. 2000).

### Waxy organic matter proxy

The waxy OM proxy $p_{wax}$, derived by Zheng et al. (2007), reflects the relative proportion of waxy hydrocarbons derived from emergent macrophytes and terrestrial plants to total hydrocarbons and is additionally used, as the $p_{aq}$ was derived for tropical and temporal regions (Jongejans et al. 2020):

$$P_{wax} = \frac{C_{27} + C_{29} + C_{31}}{C_{23} + C_{25} + C_{27} + C_{29} + C_{31}}, \quad (9)$$

with values for submerged or floating macrophytes < 0.5, for emergent macrophytes between 0.6 and 0.7, and for terrestrial plants > 0.75 (Jongejans et al. 2020).

## 4.3 Statistical analysis

To evaluate the obtained data, the results were statistically analysed. All analysis and visualisations of the results were carried out with the free software *R v 2023.12.1.402* (Posit team 2024). To receive a first overview over the data, descriptive statistics as the minimum, maximum, mean and median was used.

As the vibracoring led to a soil compaction of 144 cm for BAL24-T0-L, especially in the upper layers, a normalized exponential depth correction after the classic compaction model of Athy (1930) with the correction method of Lisiecki and Herbert (2007) was applied for this core. For this, it was assumed that the porosity decreases, and therefore the compression increases exponentially with depth, as the top is drilled the longest and has softer soil. This is resulting in the correction formula:

$$z_t = D_p * \frac{1 - e^{-z_m/\lambda}}{1 - e^{-L_c/\lambda}}, \quad (10)$$

where $z_t$ is the true depth, $z_m$ any measured depth within the core liner, $D_p$ the penetration depth of the barrels in the sediment, $L_c$ the recovered core length and λ the exponential e-folding scale.

A λ of 100 cm was used, based on previous thermokarst und Yedoma studies regarding the water content, grain size and porosity (Anthony et al. 2014; Strauss et al. 2017). Figure A. 6 shows the resulting core correction curve for BAL-T0-L.

### 4.3.1 Correlation

A correlation matrix after Pearson was calculated to obtain an initial overview of the relationships between the parameters with the *corrplot* package (Wei and Simko 2024). Further, the relations of degradation proxies were analysed by scatterplots with linear regression models and the Pearson correlation coefficient with the *ggpubr* package (Kassamara 2023).

### 4.3.2 Significance testing

The statistical distribution was tested via the Shapiro-Wilk normality test and a quantile-quantile plot. As the distribution was non-normal, the non-parametric Kruskal-Wallis rank sum test was applied to compare the biogeochemical and biomarker parameters between the four different profiles, as well as the non-parametric Mann-Whitney-Wilcoxon test for pairwise comparison, using the packages *ggpubr* (Kassamara 2023) and *ggplot2* (Wickham 2016). The same was carried out between the three permafrost layers AL, PF and T.

### 4.3.3 Clustering analysis

Finally, a principal component analysis (PCA) was applied on the scaled data, to reduce the data dimension and to indicate underlaying patterns in the parameters, especially regarding the questions if these patterns correspond to the cores and permafrost layers. It was performed once with all parameters and once with the biomarker proxies just as supplementary data, not included in the calculation. A PCA serves to transform the variables into a smaller and uncorrelated amount of essential feature, the principal components, which mainly explain the variance in the data, by minimizing the loss of information. This can be used for a more efficient interpretation and visualization of the data (Abdi and Williams 2010; Jolliffe and Cadima 2016; Greenacre et al. 2022). Afterwards, an agglomerative (bottom-up) hierarchical clustering on principal components (HCPC) was made based on the results of the PCA to group the data in clusters of objects that are like each other while the objects in different clusters are quite different from each other. This bottom-up method begins by treating each data point as an individual cluster. Clusters are then successively merged according to their similarity, ultimately resulting in one single cluster encompassing all objects (Bridges 1966; Shetty and Singh 2021; Uchenna and Olusola 2024). The PCA and HCPC were carried out with the R package *FactoMineR* (Lê et al. 2008) and visualized in a biplot of individuals and

variables with the package *factoextra* (Kassamara and Mundt 2020). To investigate the properties of the resulting clusters, boxplots of the different groups were created and compared with each other.

# 5. Results

## 5.1 Core description

The sedimentological and cryolithological description as well as photos of the cores during subsampling in the climate chamber can be seen in Appendix Figure A. 1, Figure A. 2, Figure A. 3 and Figure A. 4.

## 5.2 Sedimentology

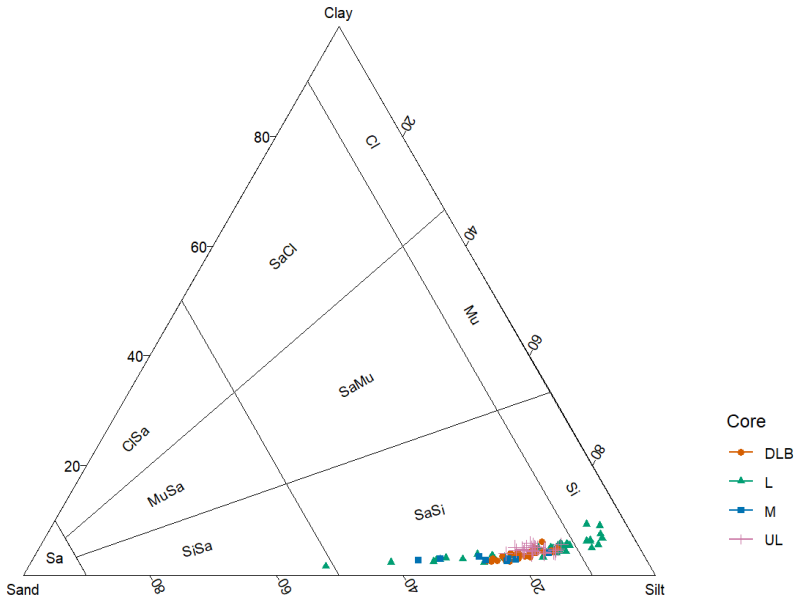


*Figure 20. Sand-Silt-Clay diagram after Folk and Ward (1957) for the four different cores.*

Figure 20 shows that most of the samples are in the section of sandy silt, also confirmed by the fact that most of the samples consist of coarse silt. Only the lake core has samples in the silt and silty sand fraction.

### Upland – BAL24-T0-UL

BAL24-T0-UL has a unimodal grain size distribution and is dominated by silt with a percentage from 74.35 to 82.28 vol%, clay is the lowest fraction with < 6 vol%. The highest volume share is at 122 cm b.s.l. and 40.1 µm, but Figure 21 shows a relatively constant grain size with depth. All samples are classified as poorly sorted coarse silt. The mean grain size is similar for all depths and ranges from 18.22 (204.5cm b.s.l.) to 26.39 µm (112 cm b.s.l.), as seen in Figure 22. Bulked biogeochemical and hydrochemical parameters for the four cores against depth. The background colours indicate the active layer (yellow), perennial

frozen ground (brown), the talik (grey) and the ice wedge (blue), according to the cryolithologically observation due the subsampling. Red arrows for the radiocarbon dating indicate infinite ages. The absolute ice content varies very strong, especially between 27 and 128 cm b.s.l. It ranges from 99.92 wt% at 128 cm b.s.l. down to 26.96 wt% at 39.5 cm b.s.l. with a mean of 56.63 wt%.

## Thermokarst Lake – BAL24-T0-L – originally unfrozen

BAL24-T0-L consists of poorly sorted coarse silt, with a shift towards medium silt between 150 and 350 cm b.s.l. and very coarse silt at the bottom. The silt fraction is highest with a share of 47.10 – 88.24 vol%, the clay faction the lowest with 4.6 vol% in average. The distribution is mostly unimodal, with a slight second peak in middle sand. The highest share of 9.6 vol% for 66.9 µm is at 444.7 cm b.s.l. (Figure 21). The mean grain size, as seen in Figure 22, ranges from 10.43 – 61.17 µm, with a mean of 22.92 µm. It is relatively homogeneous in the upper core and increasing from 230 cm b.s.l with a peak of 61.17 µm at 444.7 cm b.s.l. The absolute water content shows strong variations in the upper part with wt% from 37.47 at the top to 67.48 at 155.4 cm b.s.l., while it gets more homogeneous in the lower part, ranging between 22.3 and 35.45 vol% at the bottom.

## Drained Lake Basin – BAL24-T0-DLB

The sediments of BAL24-T0-M are mainly classified as poorly sorted coarse silt with some samples consisting of very coarse silt at the bottom. Silt ranges between 72.01 – 82.00 vol%, while the clay content is not higher than 6 vol%. Figure 21 shows a maximum volume share with 6.3 vol% and a grain size of 40.1 µm at 144.5 cm b.s.l. but the unimodal distribution is quite constant over depth.

The mean grain size is on average 26.19 µm and shows a slightly increasing trend with depth, ranging from 18.79 to 32.36 µm. The absolute water / ice content is highest at top with 72.31 wt% and rapidly decreasing to 38.31 wt% at 25 cm b.s.l. after which it stabilized between 27.59 and 37.63 wt% (Figure 22).

## Marine core – BAL24-T0-M – originally unfrozen

The marine samples are classified as poorly sorted coarse to very coarse silt, dominated by silt with a share between 61.18 and 81.16 % and a clay content smaller than 4 vol%. The distribution is unimodal and quite constant over depth with a peak at 30.5 cm b.s.l. and a share of 7.05 vol% for the grain size 40.1 µm. The mean grain size ranges from 22.51 to

39.61 µm with a slightly increase with depth. The absolute water content decreases from 47.55 wt% at the top down to 24.11 wt% at 49.5 cm b.s.l.

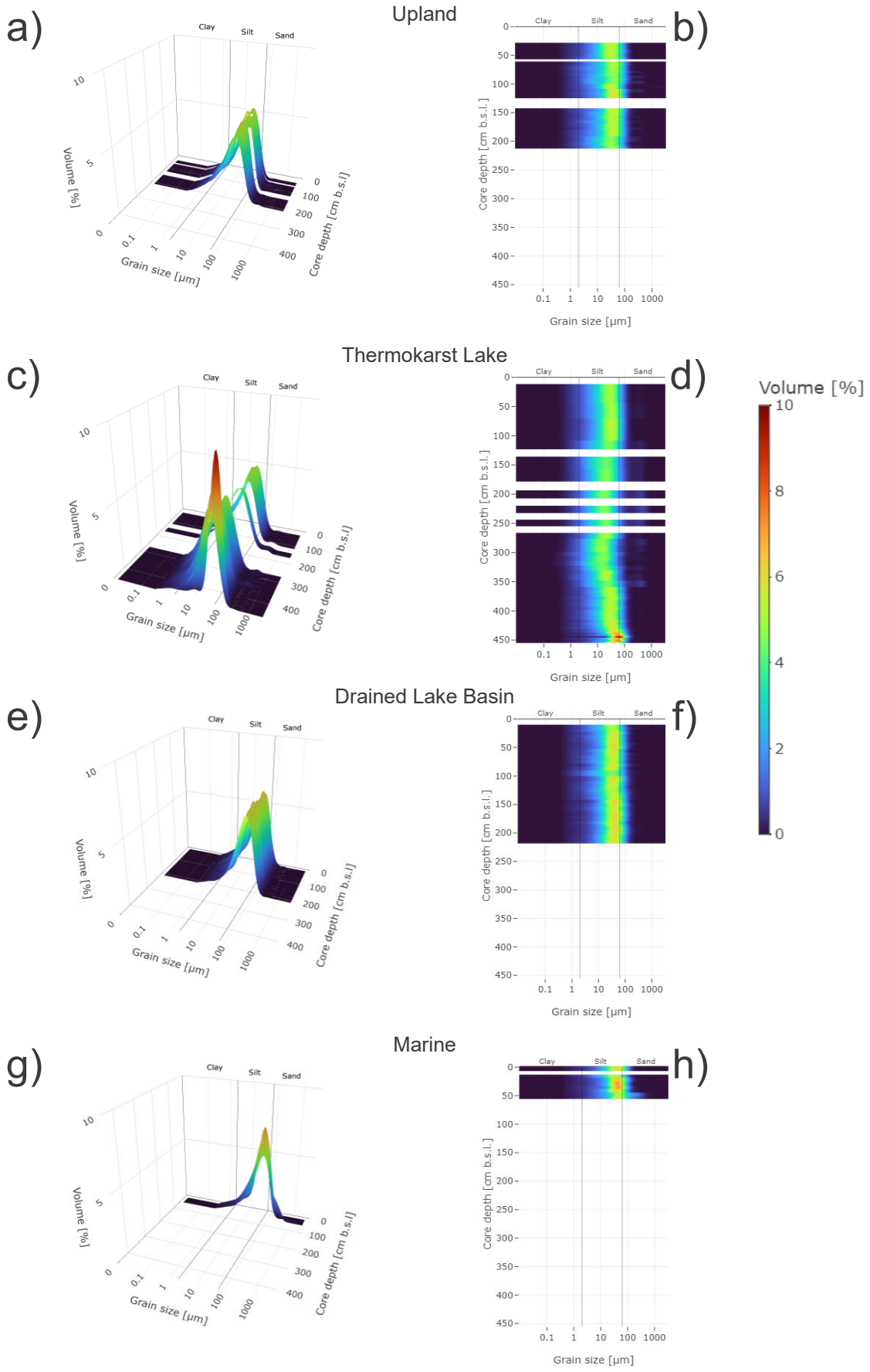


*Figure 21. Grain size distribution of the four cores against profile depth with a view from (a, c, e, g) the side and (b, d, f, h) above.*

## 5.3 Geochronology

*Table 2. Calibrated radiocarbon ages.*

| Core | Mean Depth [cm b.s.l.] | $^{14}$C ages mean [cal. ka BP] | $^{14}$C ages min. [cal. ka BP] | $^{14}$C ages max. [cal. ka BP] | Range [ka] |
|---|---|---|---|---|---|
| UL | 21.0 | 0.086 | 0.032 | 0.14 | 0.108 |
| | 62.0 | 30.2915 | 30.175 | 30.408 | 0.233 |
| | 101.5 | 34.385 | 34.198 | 34.572 | 0.374 |
| | 146.0 | 34.4765 | 34.29 | 34.663 | 0.373 |
| | 199.0 | 32.7775 | 32.269 | 33.286 | 1.017 |
| L | 6.0 | 1.7815 | 1.721 | 1.842 | 0.121 |
| | 35.5 | 0.2975 | 0.287 | 0.308 | 0.021 |
| | 97.0 | 0.3965 | 0.36 | 0.433 | 0.073 |
| | 138.5 | 0.4805 | 0.458 | 0.503 | 0.045 |
| | 199.5 | 2.27 | 2.24 | 2.3 | 0.060 |
| | 242.5 | 11.9155 | 11.829 | 12.002 | 0.173 |
| | 309.0 | 1.5335 | 1.517 | 1.55 | 0.033 |
| DLB | 12.0 | 1.1155 | 1.054 | 1.177 | 0.123 |
| | 57.0 | > 50.000 | | | |
| | 107.0 | > 50.000 | | | |
| | 153.0 | > 50.000 | | | |
| | 211.5 | > 38.086 | | | |
| M | 11.5 | 0.8 | 0.684 | 0.916 | 0.232 |
| | 53.5 | 28.221 | 27.678 | 28.764 | 1.086 |

*Note.* Ages >50 are infinite.

All four cores show a trend with a young sediment layer on top <2 cal. ka BP. While BAL24-T0-L has young sediments in all depth ranging between 0.3 and 2 cal. ka BP, except a peak at 242.5 cm b.s.l. with 12 cal. ka BP, the other three cores have older sediments below the surface layer. There the calibrated ages of BAL24-T0-UL and BAL24-T0-M are ~30 cal. ka BP, while BAL24-T0-DLB has the oldest sediments with infinite ages > 50 cal. ka BP.

## 5.4 Bulked biochemical parameters

A visualization of the bulked parameters for all for cores is shown in Figure 22. The corresponding statistical parameters can be seen in Table 3, Table 4, Table 5 and Table 6.

### Upland – BAL24-T0-UL

BAL24-T0-UL has the highest values for TOC, TN and C/N in the upper 40 cm b.s.l. with maximum values up to 44.42 wt%, 2.01 wt% and 42.02 respectively. Underneath, the values stay relatively constant around 5 wt%, 0.4 wt% and 7 with a slightly increasing trend with depth and a small peak at 59 cm b.s.l. $\delta^{13}$C rises strongly in the upper 40 cm b.s.l. from around -30 to -27 ‰ vs. VPDB, where after it slowly approaches values around -26‰ vs. VPDB in the depth.

The values of the water isotopes $\delta^{18}O$ and $\delta D$ are decreasing in the upper half from -15 and -112 ‰ vs. SMOW, except a jump above the ice wedge, followed by a strong decrease in the ice wedge layers after which the values stay around -20 and -150 ‰ vs. SMOW. The DOC value variates between 5 and 250 mg $L^{-1}$ in the upper part till the end of the ice wedge, where after it rises to the maximum of 1707 mg $L^{-1}$. The same is true for the EC with an increase from 43 to 2379 µg $cm^{-1}$ below the ice wedge. The pH-value is the lowest in the top, increasing with depth to its maximum in the ice wedge and decreasing again afterwards.

*Table 3. Biogeochemical and hydrochemical parameters for BAL24-T0-UL.*

| BAL24-T0-UL | Parameter | n.valid | min | med | max | mean | sd |
|---|---|---|---|---|---|---|---|
| Biogeochemistry | TOC [wt%] | 39 | 1.85 | 4.75 | 44.42 | 8.42 | 10.88 |
| | TN [wt%] | 39 | 0.11 | 0.39 | 2.01 | 0.50 | 0.40 |
| | C/N [-] | 39 | 9.07 | 12.26 | 42.02 | 14.28 | 6.23 |
| | $\delta^{13}C$ [‰ vs. VPDB] | 32 | -29.76 | -26.27 | -25.81 | -26.58 | 0.85 |
| Hydrochemistry | $\delta^{18}O$ [‰ vs. SMOW] | 14 | -20.36 | -18.14 | -14.63 | -17.83 | 2.10 |
| | $\delta D$ [‰ vs. SMOW] | 14 | -160.21 | -139.43 | -112.28 | -137.89 | 17.11 |
| | mean d excess | 14 | -3.06 | 4.61 | 10.76 | 4.74 | 3.85 |
| | DOC [mg $L^{-1}$] | 15 | 5.78 | 159.10 | 1707.00 | 457.70 | 566.58 |
| | EC [µS $cm^{-1}$] | 15 | 43.41 | 205.90 | 2379.00 | 679.89 | 831.28 |
| | pH [-] | 15 | 4.87 | 6.74 | 7.43 | 6.58 | 0.69 |

## Thermokarst Lake – BAL24-T0-L

TOC in BAL24-T0-L has strong variations in the upper half with a range between 4.4 and 24.4 wt%, after which it decreases continuous with depth to 0.6 wt%. TN and C/N show the same pattern with values between 0.11 to 1.28 wt% and 9.26 to 21.08, respectively, with 6 samples below the detection limit. $\delta^{13}C$ varies over depth with a minimum of -28.61 ‰ vs. VPDB at 318.5 cm b.s.l. $\delta^{18}O$ and $\delta D$ are highest at the top and the bottom with values around -17 and -134 ‰ vs. SMOW, respectively and are continuous decreasing towards the bottom part with a final increase at the bottom. DOC, EC and pH stay constant around 155 mg $L^{-1}$, 623 µS $cm^{-1}$ and 7.8 over the profile.

*Table 4. Biogeochemical and hydrochemical parameters for BAL24-T0-L.*

| BAL24-T0-L | Parameter | n.valid | min | med | max | mean | sd |
|---|---|---|---|---|---|---|---|
| Biogeochemistry | TOC [wt%] | 61 | 0.60 | 2.79 | 24.40 | 6.30 | 6.57 |
| | TN [wt%] | 61 | 0.01 | 0.21 | 1.28 | 0.39 | 0.36 |
| | C/N [-] | 55 | 9.26 | 13.61 | 21.08 | 14.08 | 2.85 |
| | $\delta^{13}C$ [‰ vs. VPDB] | 55 | -28.61 | -26.80 | -24.74 | -26.78 | 0.73 |
| Hydrochemistry | $\delta^{18}O$ [‰ vs. SMOW] | 17 | -18.95 | -18.56 | -17.03 | -18.30 | 0.62 |
| | δD [‰ vs. SMOW] | 17 | -152.39 | -147.70 | -133.24 | -146.07 | 6.01 |
| | mean d excess | 17 | -1.17 | -0.11 | 6.95 | 0.29 | 1.85 |
| | DOC [mg $L^{-1}$] | 22 | 113.80 | 151.55 | 213.50 | 155.35 | 29.63 |
| | EC [µS $cm^{-1}$] | 22 | 91.00 | 626.40 | 862.60 | 623.25 | 176.29 |
| | pH [-] | 22 | 7.22 | 7.74 | 8.22 | 7.75 | 0.23 |

## Drained Lake Basin – BAL24-T0-DLB

TOC and TN drop in the upper 15 cm b.s.l. from the maximum of 18.4 and 1.6 wt% and remain at values below 8.1 and 0.1 wt%, whereby two samples are below the detection limit. C/N stays below 15.9 with small variations. $\delta^{13}C$ ranges between -26.3 and -24.5 ‰ vs. VDPB with strong fluctuations over depth. $\delta^{18}O$ and δD have their maximum at the top with -17.7 and -112.2 ‰ vs. SMOW with a strong decrease afterwards up to -19.6 and -146.4 ‰ vs. SMOW. DOC, EC and pH have small changes over the profile around 189.2 mg $L^{-1}$, 909.4 µS $cm^{-1}$ and 8.

*Table 5. Biogeochemical and hydrochemical parameters for BAL24-T0-DLB.*

| BAL24-T0-DLB | Parameter | n.valid | min | med | max | mean | sd |
|---|---|---|---|---|---|---|---|
| Biogeochemistry | TOC [wt%] | 43 | 1.19 | 2.76 | 18.38 | 3.12 | 2.69 |
| | TN [wt%] | 43 | 0.01 | 0.22 | 1.57 | 0.24 | 0.23 |
| | C/N [-] | 41 | 10.19 | 12.25 | 15.88 | 12.50 | 1.29 |
| | $\delta^{13}C$ [‰ vs. VPDB] | 37 | -26.34 | -25.31 | -24.45 | -25.37 | 0.51 |
| Hydrochemistry | $\delta^{18}O$ [‰ vs. SMOW] | 12 | -19.57 | -18.71 | -14.25 | -17.70 | 2.02 |
| | δD [‰ vs. SMOW] | 12 | -146.35 | -142.17 | -112.15 | -135.20 | 12.82 |
| | mean d excess | 12 | 1.30 | 6.46 | 14.60 | 6.40 | 4.13 |
| | DOC [mg $L^{-1}$] | 17 | 46.63 | 211.25 | 312.25 | 189.22 | 71.11 |
| | EC [µS $cm^{-1}$] | 17 | 733.90 | 923.70 | 1071.00 | 909.42 | 103.35 |
| | pH [-] | 17 | 7.62 | 7.97 | 8.41 | 7.96 | 0.18 |

## Marine – BAL24-T0-M

The values for TOC and TN are slightly decreasing with depth from 3 and 0.2 wt% at the top to 1.5 and 0.1 wt% at the bottom, with 5 samples in the bottom under the detection limit for TN. C/N varies between 11.9 and 19.7 over the profile. $\delta^{13}C$ is increasing in the depth, with a small decrease at the bottom around -26.7 ‰ vs. VDPB. $\delta^{18}O$, $\delta D$, DOC and pH have values around -13.3‰ vs. SMOW, -102.1‰ vs. SMOW, 0.1 mg $L^{-1}$ and 7.7, while EC is increasing with depth up to 19020 µS $cm^{-1}$.

*Table 6. Biogeochemical and hydrochemical parameters for BAL24-T0-M.*

| BAL24-T0-M | Parameter | n.valid | min | med | max | mean | sd |
|---|---|---|---|---|---|---|---|
| Biogeochemistry | TOC [wt%] | 12 | 1.14 | 1.95 | 3.03 | 1.95 | 0.64 |
| | TN [wt%] | 12 | 0.01 | 0.12 | 0.21 | 0.09 | 0.08 |
| | C/N [-] | 7 | 11.85 | 14.48 | 19.74 | 14.88 | 2.52 |
| | $\delta^{13}C$ [‰ vs. VPDB] | 9 | -26.63 | -26.32 | -25.88 | -26.27 | 0.28 |
| Hydrochemistry | $\delta^{18}O$ [‰ vs. SMOW] | 3 | -13.42 | -13.28 | -13.14 | -13.28 | 0.14 |
| | $\delta D$ [‰ vs. SMOW] | 3 | -102.51 | -102.25 | -101.57 | -102.11 | 0.48 |
| | mean d excess | 3 | 3.57 | 3.74 | 5.09 | 4.13 | 0.84 |
| | DOC [mg $L^{-1}$] | 12 | 0.01 | 0.12 | 0.21 | 0.09 | 0.08 |
| | EC [µS $cm^{-1}$] | 3 | 17290.00 | 19380.00 | 20390.00 | 19020.00 | 1581.04 |
| | pH [-] | 3 | 7.47 | 7.83 | 7.99 | 7.76 | 0.27 |

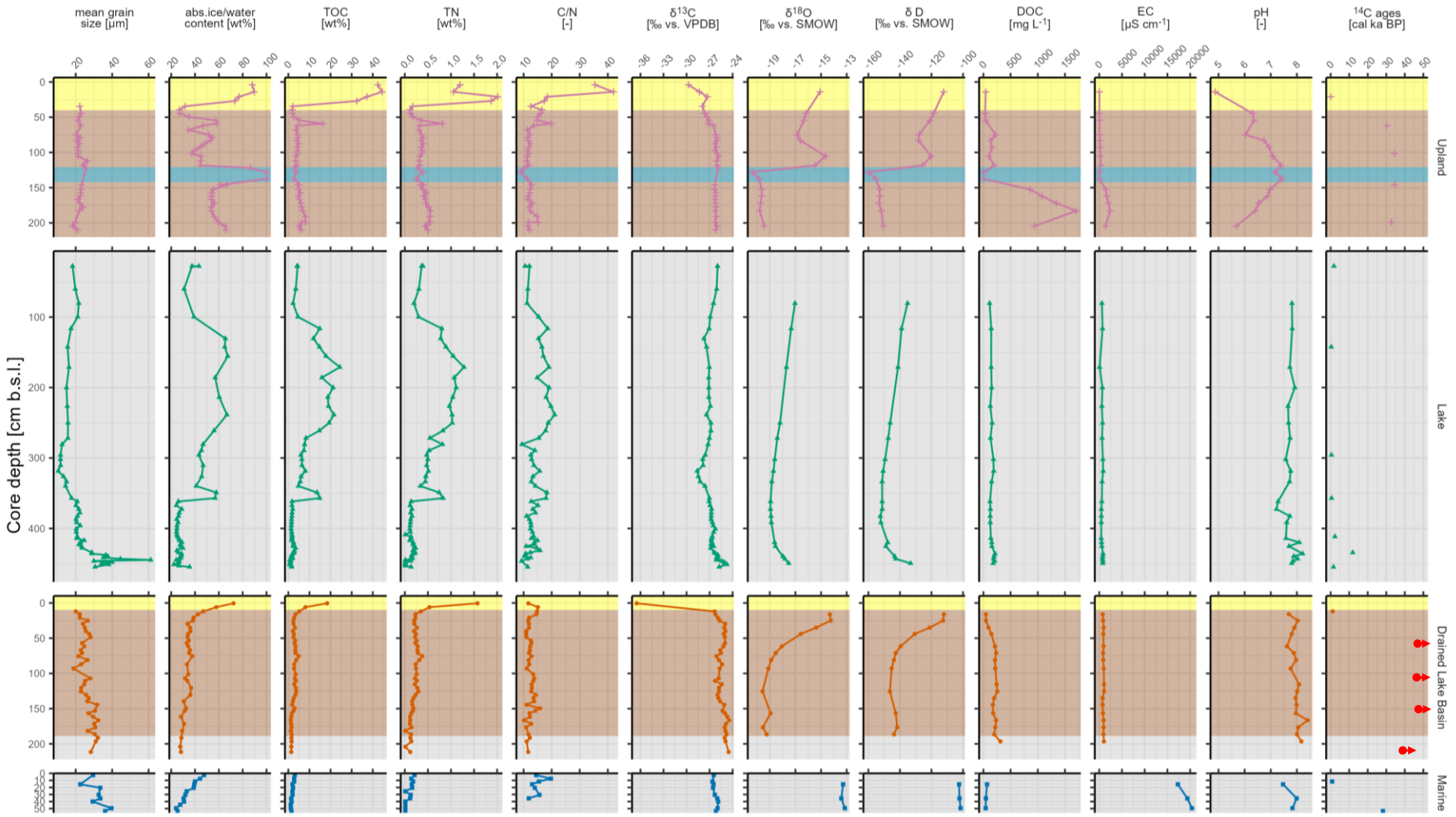


*Figure 22. Bulked biogeochemical and hydrochemical parameters for the four cores against depth. The background colours indicate the active layer (yellow), perennial frozen ground (brown), the talik (grey) and the ice wedge (blue), according to the cryolithologically observation due the subsampling. Red arrows for the radiocarbon dating indicate infinite ages.*

## 5.5 Biomarker

The visualization of the biomarker proxies for all cores is displayed in Figure 23.

### Upland – BAL24-T0-UL

The total long chain alkane concentration is 1115.2 µg $g^{-1}$ Sed and 3439.1 µg $g^{-1}$ TOC in the top sample where after it drops to values below 12 µg $g^{-1}$ Sed and 600 µg $g^{-1}$ TOC. The same trend is true for CPI with 76.9 on the top and values below 13.6 beneath. $P_{aq}$ is increasing in the upper part from 0.02 to values around 0.5, $p_{wax}$ shows the opposite trend, as the ACL with values greater than 26.

### Thermokarst Lake – BAL24-T0-L

The total long chain alkane concentration for the Thermokarst Lake varies strongly with depth without a trend between 1.6 and 160 µg $g^{-1}$ Sed and 94.8 and 896.8 µg $g^{-1}$ TOC. The CPI shows a similar pattern ranging around 18. $P_{aq}$ is first decreasing and then increasing in depth between 0.05 and 0.56, vice versa for $p_{wax}$ and ACL with values higher than 26.7.

### Drained Lake Basin BAL24-T0-DLB

The concentration of the long chain alkanes of BAL24-T0-DLB varies slightly from 0.4 and 30.5 to 11 µg $g^{-1}$ Sed and 201.6 µg $g^{-1}$ TOC, with highest concentration at the top. $P_{aq}$ is increasing with depth and slightly decreases in the bottom, opposite for $p_{wax}$. The CPI decreases with depth from 14.8 to 4.0, while the ACL stays around 27.6.

### Marine – BAL24-T0-M

The marine core has a long chain alkane concentration between 3.1 and 8 µg $g^{-1}$ Sed, and 146.2 and 412.4 µg $g^{-1}$ TOC. The $p_{aq}$ is slightly increasing from the top to the bottom to 0.5, while the CPI varies around 7.1 and the ACL decreases with a mean of 27.6.

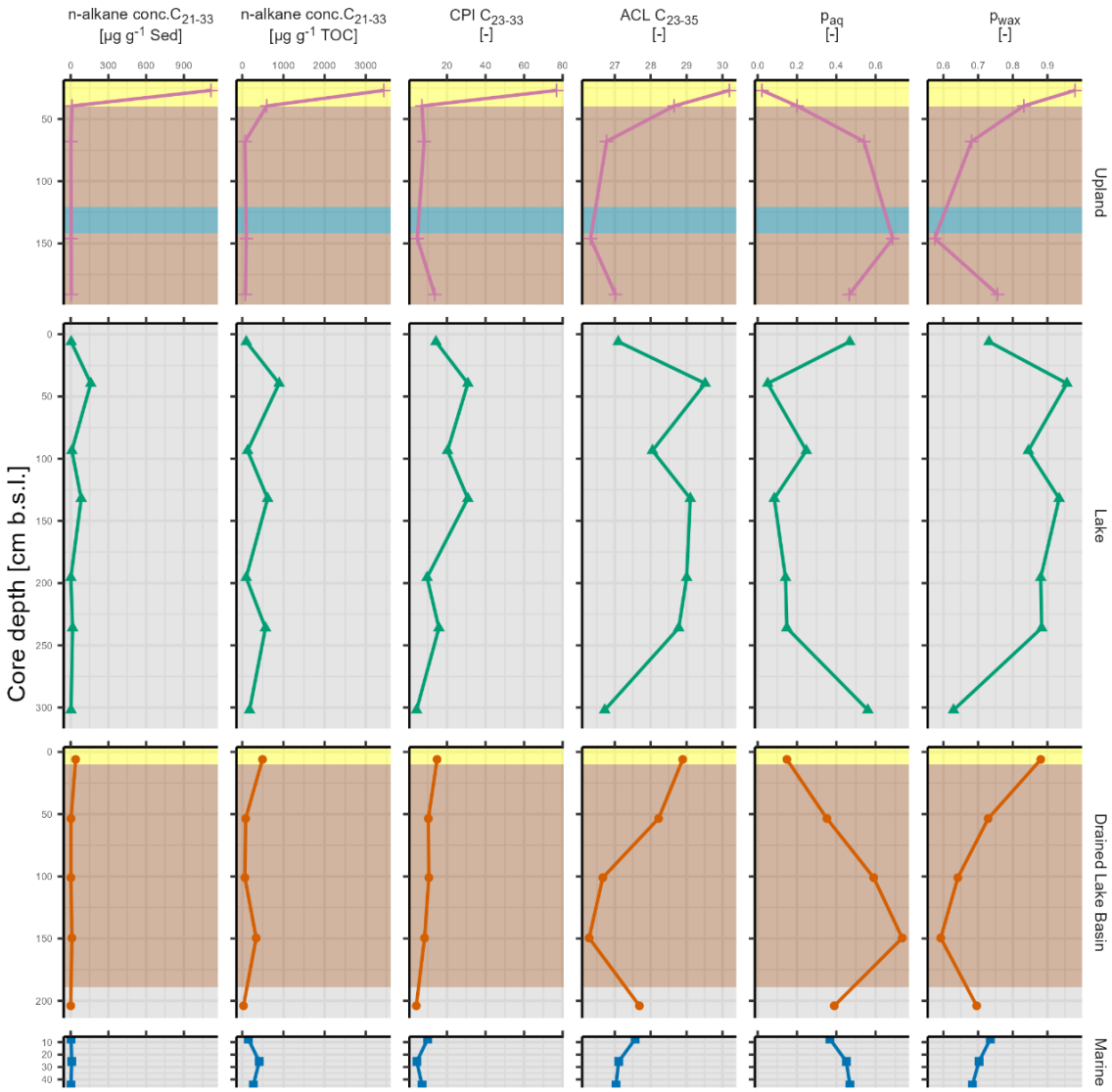


*Figure 23. Biomarker parameters of the four cores against depth. The background colours indicate the active layer (yellow), perennial frozen ground (brown), the talik (grey) and the ice wedge (blue), according to the cryolithologically observation due the subsampling.*

## 5.6 Statistical analysis

### 5.6.1 Correlations

The correlation matrix of all parameters can be seen in the Appendix Figure A. 7. Figure 24 shows the scatterplots of selected OM degradation markers and their correlation among each other. There is a clear correlation between TOC and C/N as well as ACL and C/N (R = 0.67 and R = 0.54) and a very strong correlation between TOC and CPI (R = 0.97). The correlation between C/N and CPI is moderate, whereby the p-value is under the significance level of 0.05 (R = 0.4).

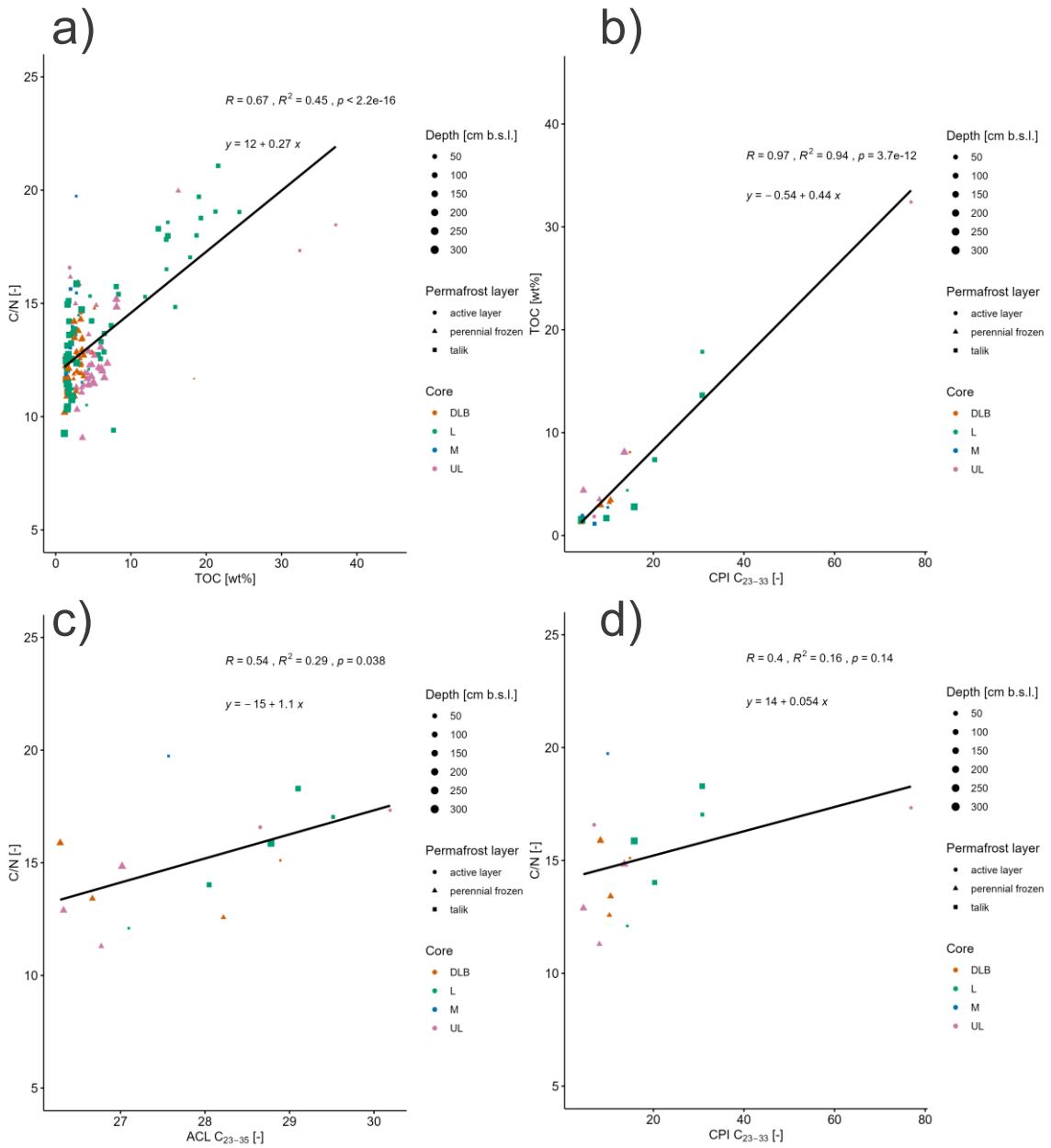


*Figure 24. Scatter plots of selected OM degradation proxies. The regression equations, R, $R^2$ and the p-values are each shown at the top of the plots. The samples of AL are shown as circles, of PF at triangles and of T as squares.*

## 5.6.2 Significance testing

### Difference-testing between the cores

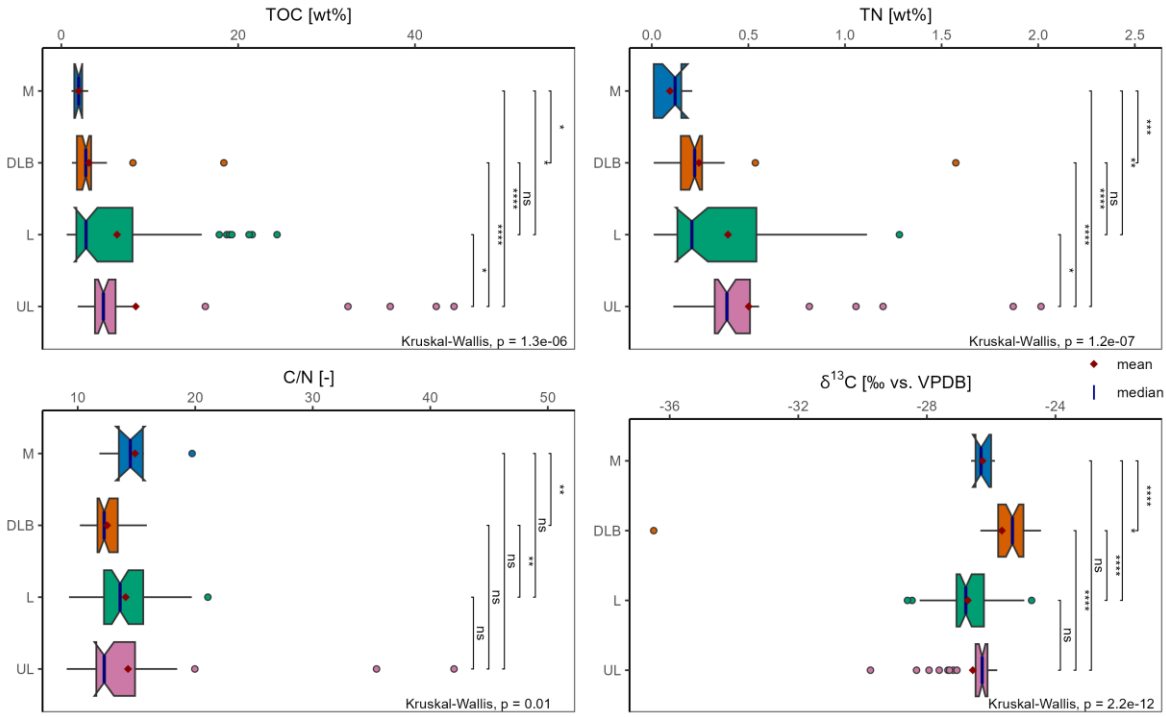


*Figure 25. Boxplot of the biogeochemistry for the four sites. The length of the box is defined by the interquartile range (25-75%), the whiskers show the data range with outliers as points. The notches indicate the 95% confidence interval of the median (Overlapping between groups indicates no difference). The median is marked by the blue line, the mean by the red diamond. The statistical differences are shown by the bars on the right (Wilcoxon-test) and in the bottom-right corner (Kruskal-Wallis-test) with ns = not significant, * for p < 0.05, ** for p < 0.01, *** for p < 0.001, **** for p < 0.0001.*

According to the biochemical parameters, the p-value of the Kruskal-Wallis-Test is under the significance level of 0.05 for all parameters (Figure 25). Therefore, significant differences between the cores exist. TOC is decreasing along the transect from UL to M, supported by the Wilcoxon test showing statistically significant differences between all cores except for L-DLB. The same applies for TN, though here TN is lower in median for L than for DLB. C/N varies more heterogenic across the transect with lower medians for UL and DLB, although UL has the highest values >40. The differences are statistically significant for DLB-L and DLB-M. $\delta^{13}C$ is similar for UL, L and M in median (-26.8 to -26.27) with lowest values for UL, but higher in median for DLB. However, the pairwise differences are statistically significant for UL-DLB, L-M and DLB-M. As already seen in Figure 22, the range is the highest for all parameters in UL.

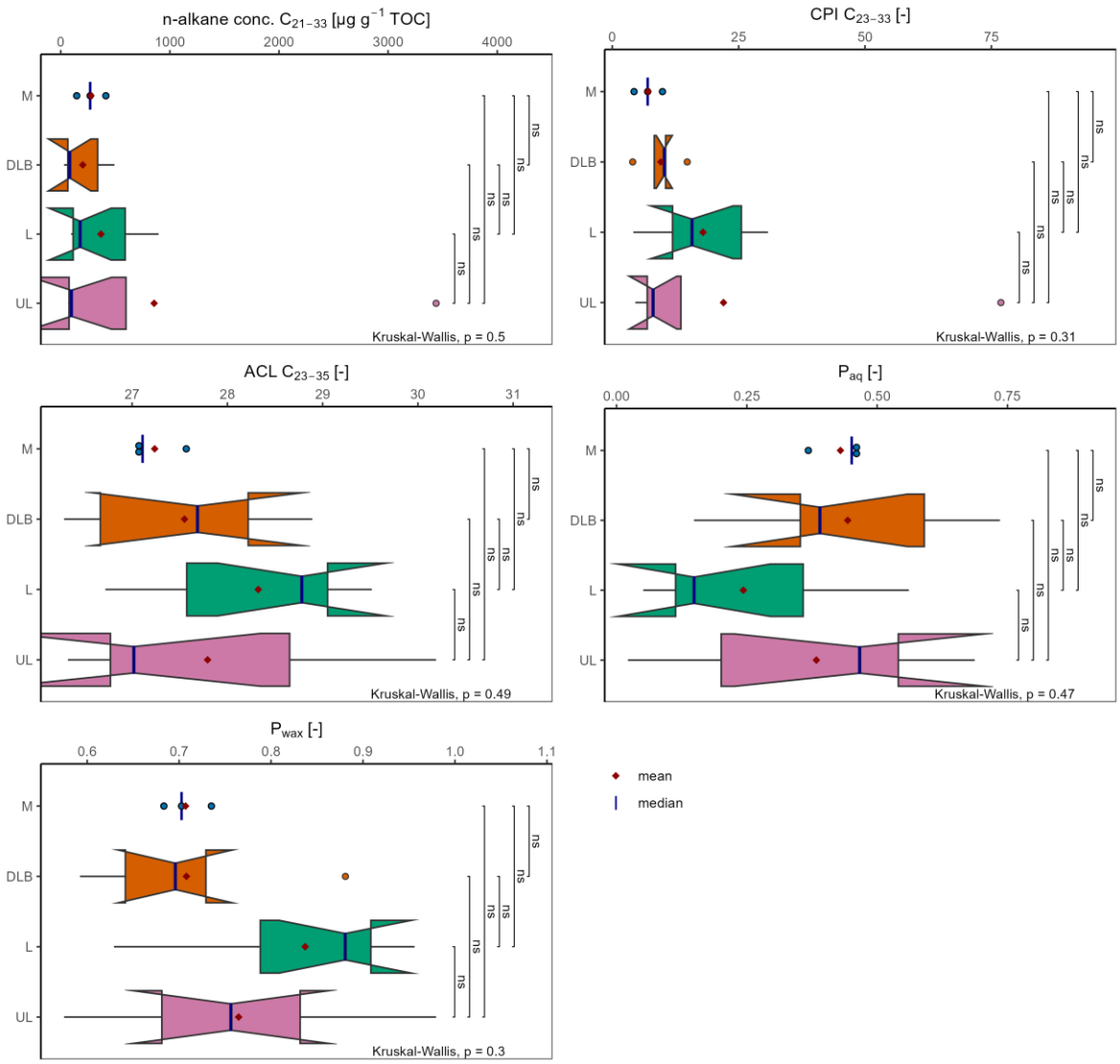


*Figure 26. Boxplot of the biomarker proxies for the four sites. The length of the box is defined by the interquartile range (25-75%), the whiskers show the data range with outliers as points. The notches indicate the 95% confidence interval of the median (Overlapping between groups indicates no difference). The median is marked by the blue line, the mean by the red diamond. The statistical differences are shown by the bars on the right (Wilcoxon-test) and in the bottom-right corner (Kruskal-Wallis-test) with ns = not significant, * for p < 0.05, ** for p < 0.01, *** for p < 0.001, **** for p < 0.0001.*

For the biomarker proxies, Figure 26, the Kruskal-Wallis-test doesn't show a statistically significant differences for the medians as the p-value is higher than the significance level of 0.05 for all parameters, yet the value range varies strongly between the cores. The same is true for the pairwise Wilcoxon-Test with p-values >0.05. While UL has the highest values for the long-chain alkane concentration, followed by L and DLB, the cores are quite alike in median. This is the same for CPI, ACL, though L is highest in median, followed by DLB. $P_{wax}$ (and vice versa $p_{aq}$) shows a similar pattern with highest range for UL, but highest median for L.

## Difference-testing between the permafrost layers

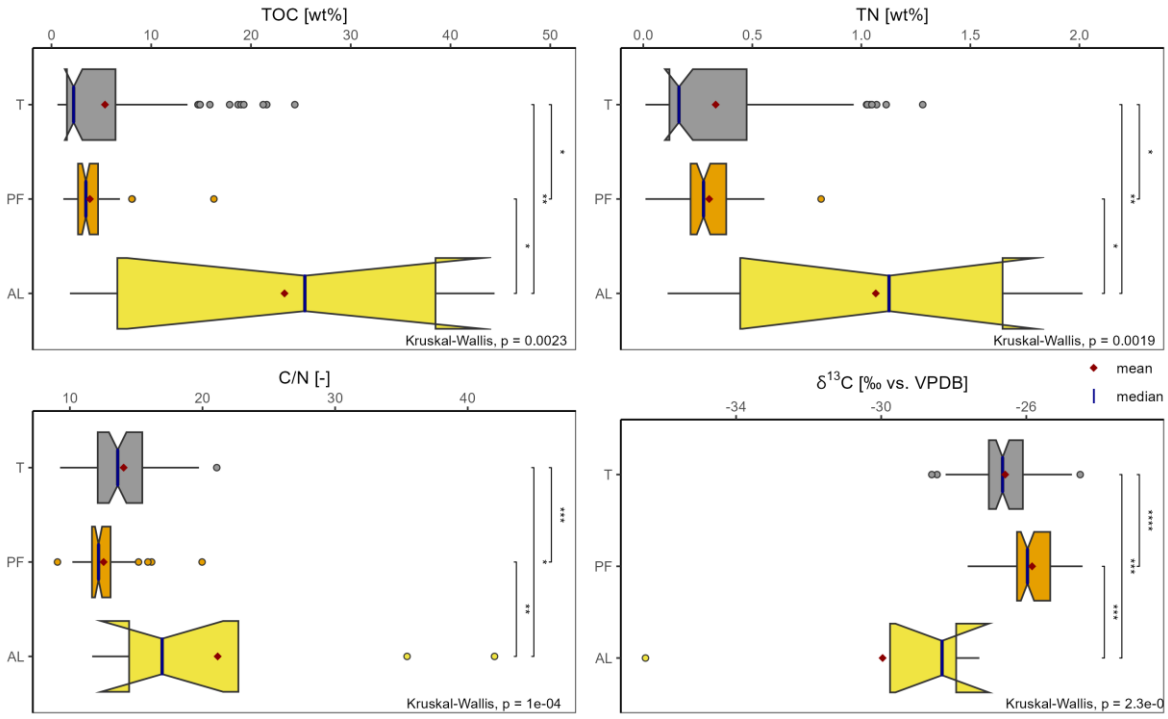


*Figure 27. Boxplot biogeochemistry for the different permafrost layers (T = talik, PF = perennial frozen, AL = active layer). The length of the box is defined by the interquartile range (25-75%), the whiskers show the data range with outliers as points. The notches indicate the 95% confidence interval of the median (Overlapping between groups indicates no difference). The median is marked by the blue line, the mean by the red diamond. The statistical differences are shown by the bars on the right (Wilcoxon-test) and in the bottom-right corner (Kruskal-Wallis-test) with ns = not significant, * for p < 0.05, ** for p < 0.01, *** for p < 0.001, **** for p < 0.0001.*

Regarding the biochemical parameters in Figure 27 , TOC, TN and C/N have the highest range and values in median in the active layer (1.85 – 44.42 wt% with a mean of 23.36 wt% for TOC). The perennial frozen samples are lowest in average (3.45 wt% for TOC), the talik samples the lowest in median (2.22, with a mean of 5.37 wt% for TOC). The pattern for $\delta^{13}C$ is vice versa, with the highest range for the active layer, but the lowest mean and median (-29.96 and -28.32 ‰ vs. VDPB). According to the Kruskal-Wallis and Wilcoxon-Test, the differences for all parameters are statistically significant (As a whole and pairwise between the layers).

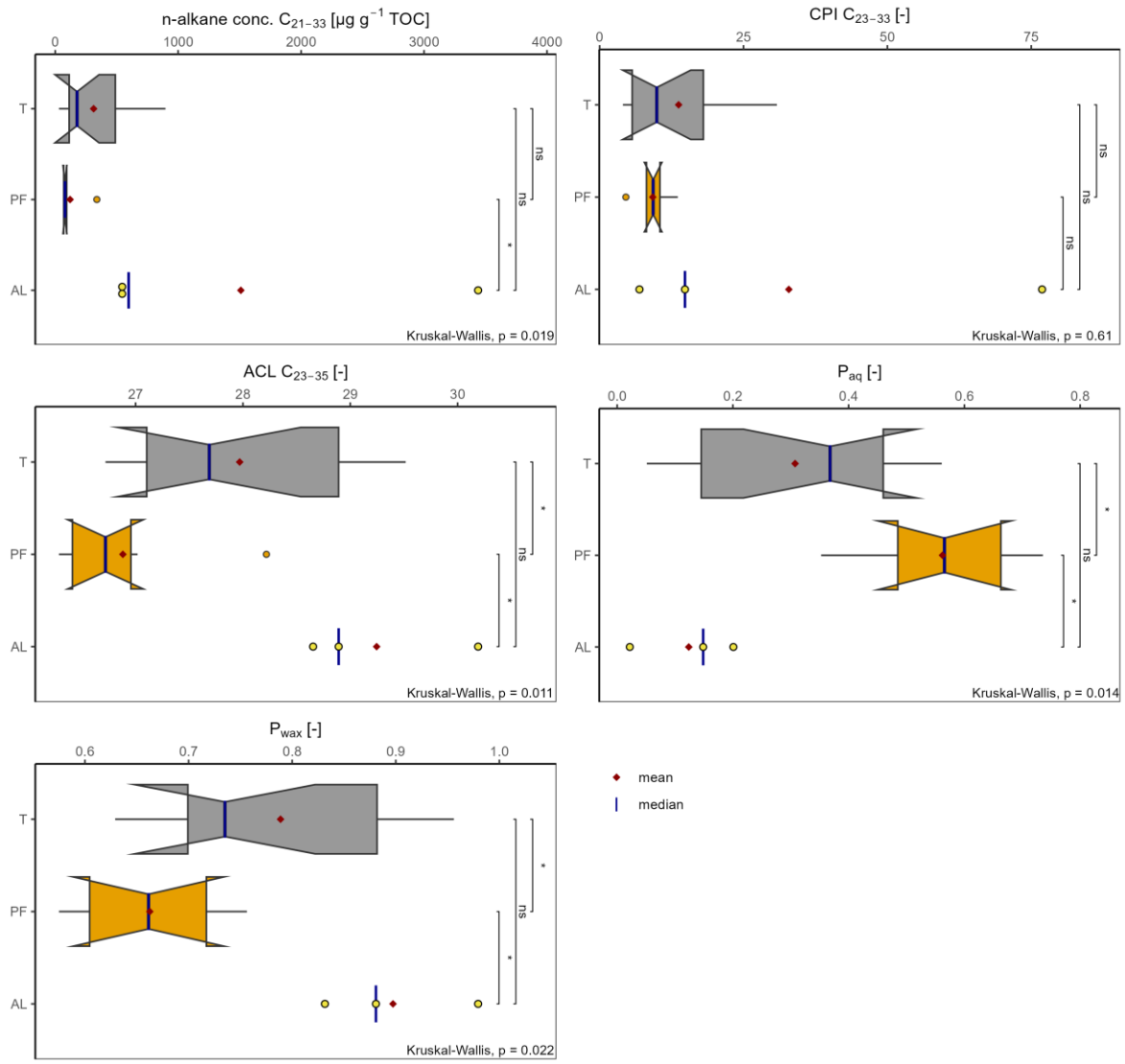


*Figure 28. Boxplot of the biomarker proxies for the different permafrost layers (T = talik, PF = perennial frozen, AL = active layer). The length of the box is defined by the interquartile range (25-75%), the whiskers show the data range with outliers as points. The notches indicate the 95% confidence interval of the median (Overlapping between groups indicates no difference). The median is marked by the blue line, the mean by the red diamond. The statistical differences are shown by the bars on the right (Wilcoxon-test) and in the bottom-right corner (Kruskal-Wallis-test) with ns = not significant, * for $p < 0.05$, ** for $p < 0.01$, *** for $p < 0.001$, **** for $p < 0.0001$.*

All biomarker proxies (despite $p_{aq}$) are in median and average the highest for the active layer and the lowest for the perennial frozen samples, as visualised in Figure 28. The range for the total long-chain n-alkane concentration and CPI are the highest in the active layer, for ACL, $p_{wax}$ and $p_{aq}$ in the talik. The p-values of the Kruskal-Wallis-test are <0.05 for all parameters, except for CPI (p=0.61), indicating statistically significant differences. The Wilcox-Cock-ney-test reveals a difference between the perennial frozen and the active layer samples. For ACL, $p_{wax}$ and $p_{aq}$, the differences are statistically significant between the active layer and perennial frozen samples, as well as between the perennial frozen and talik samples, but not between the active layer and the talik samples. For CPI, there are no statistically significant differences.

## 5.6.3 Principal component analysis and hierarchical clustering

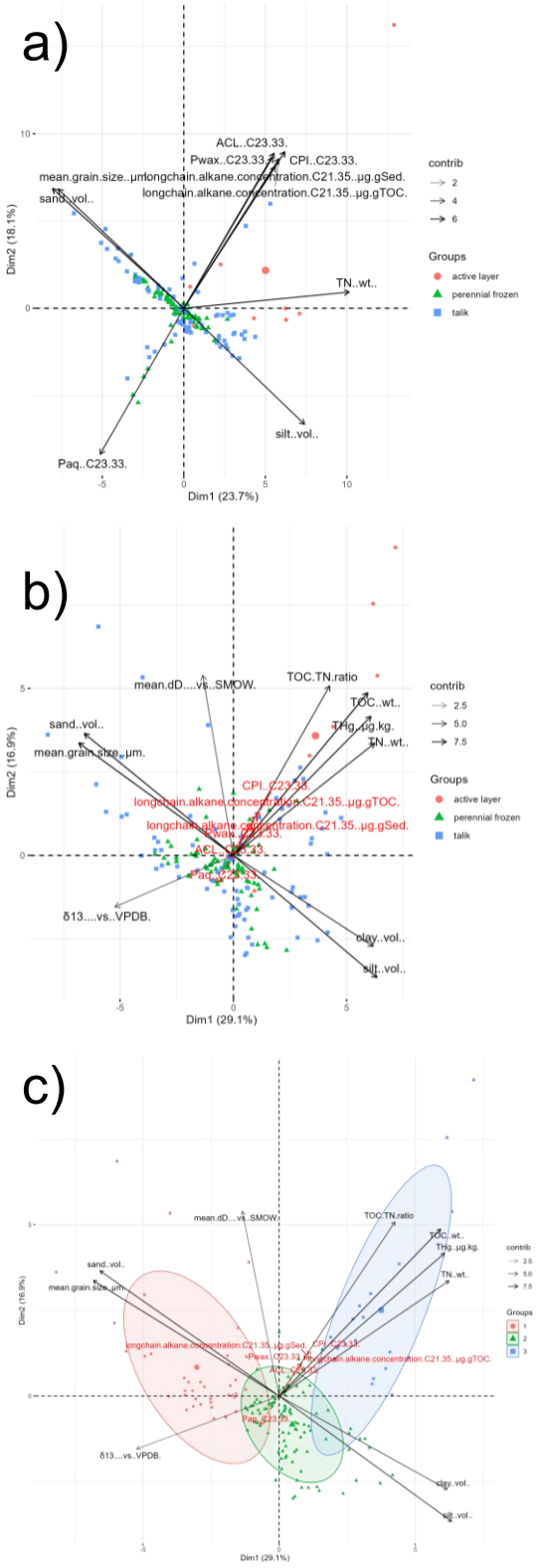


*Figure 29. Biplots of the PCA. (a) PCA with all variables, (b) and (c) PCA with biomarker proxies as supplementary variables, while (c) additionally with clusters.*

The diagram of the PCA with all variables (Figure 29a) explains 41.8% (23.7% + 18.1%) of the total data set variance. The variables mean grain size, CPI and ALC have the strongest contribution, followed by $p_{wax}$, sand content and long-chain alkane concentration. For the PCA with die biomarker proxies as supplementary variables (Figure 29b), 46 % (29.1 % + 16.9 %) of the total data set variance is explained by the diagram. Mean grain size, sand content and TOC content have strongest contribution, followed by silt and TN. The biomarker proxies are consistent with TOC und TN content, despite $p_{aq}$. Both diagrams show no clear separation between the different thermal statuses. The PF samples are slightly more centred than the T samples, while the AL samples mostly cluster to the area of Dim1 and Dim2 > 1. The HCPC divides the data set mostly accordingly towards grain size (Cluster 1), the TOC content (Cluster 3) and the centred samples with a smaller grain size (Cluster 2) (Figure 29c). The distribution between the samples after the thermal status doesn't show a clear trend. While the third cluster is mainly dominated by the T samples, the first and second are dominated by the PF and T samples (Figure A. 9).

Figure 30 shows the characteristics of the resulting cluster. The boxplots confirm the contribution of the variable's variance. Strong differences for the biomarker proxies between the second and the third cluster can be seen, as well as for the grain sizes and the radiocarbon age. Furthermore, is the third group characterized by the higher TOC and TN values.

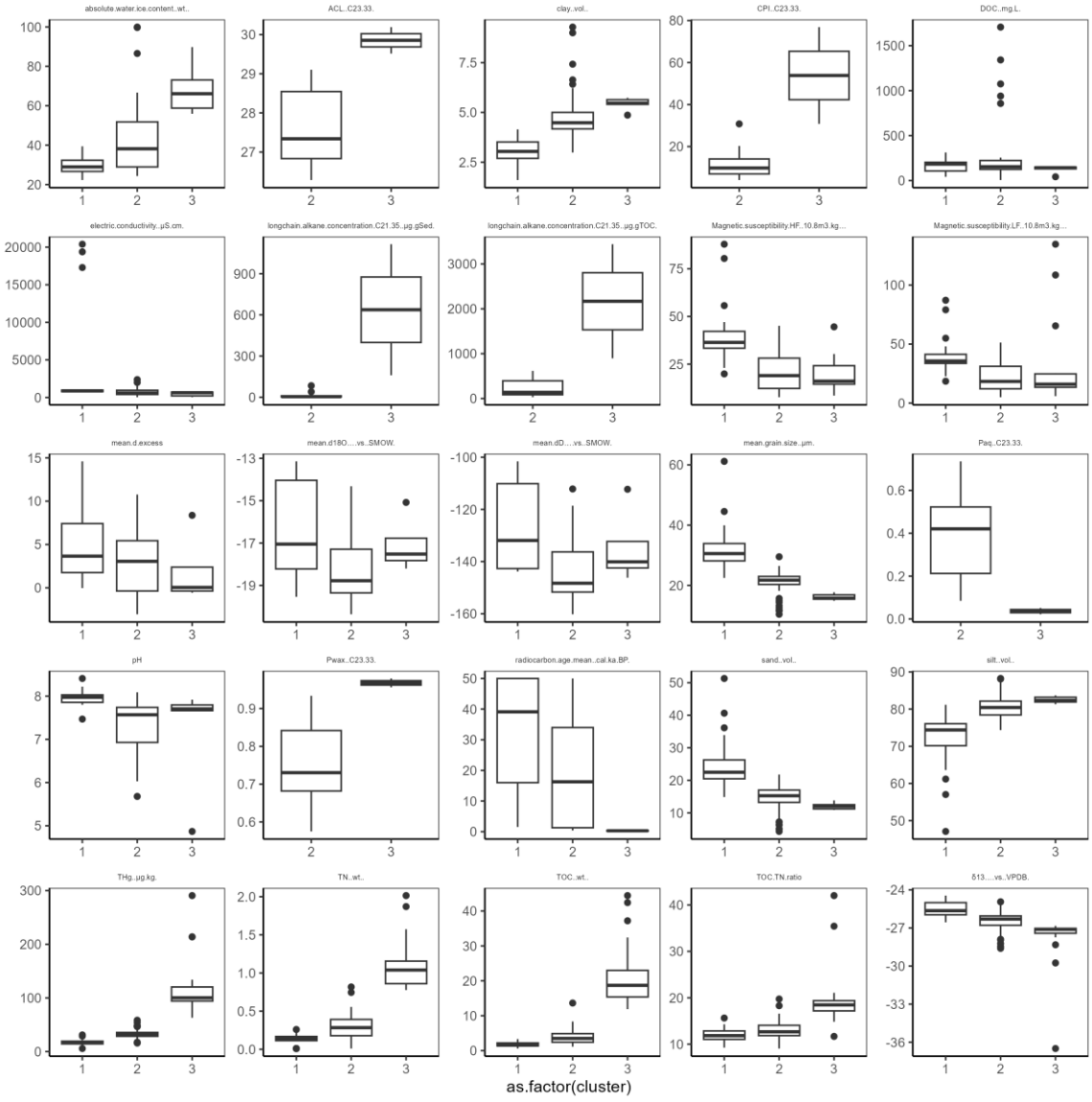


*Figure 30. Boxplot of the parameters from the resulting cluster.*

# 6. Discussion

To evaluate the obtained results, this section synthesises the findings regarding the research objectives (1) the reconstruction of the paleoenvironment and (2) the carbon characteristics. The discussion focuses on variations in OM quantity, source and quality and how these relate to permafrost dynamics and degradation processes.

## 6.1 Landscape history

### 6.1.1 Deposition mechanism at the study area

The grain size distribution shows a similar signal in all cores, indicating the same material origin at all sites. The sediments are mostly composed of poorly sorted coarse silt with a low clay content below 10 vol% and unimodal distribution, indicating aeolian processes as the dominating deposition mechanism (Strauss et al. 2012; Jongejans et al. 2018). However, the cores show a slightly bimodal distribution with a second peak at medium sand in some depths. This composition is in line with sediments from the west of the Baldwin Peninsula and indicates a slight influence of a second transport mechanism (Jongejans et al. 2018). While the sediments are stronger unimodal then found in Siberian Yedoma deposits, which showed polygenetic deposition processes with alluvial, fluvial and niveo-aeolian transport (Strauss et al. 2012; Strauss et al. 2015; Schirrmeister et al. 2020), similar patterns were found in Alaska (Jongejans et al. 2018; Schirrmeister et al. 2020). The grain size distribution with a slight shift towards finer material points towards loessal silts, which are according to Schirrmeister et al. (2025) primary aeolian deposits of coarse silt and fine sand, which were secondary redeposited. Additionally with the high massive ground ice contents up to 90 % and organic-rich layers, the syngenetic ice wedge, founded macro remains and radiocarbon ages of more than 50 cal. ka PB for DLB and 30 cal. ka BP for UL and the deeper marine samples are typically characteristics of late Pleistocene Yedoma (Schirrmeister et al. 2025).

### 6.1.2 Landscape evolution at the four study sites

#### BAL24-T0-UL

The radiocarbon dating of the upland indicates a constant deposition age of ~30 cal. ka BP with a modern top layer. The isotopic porewater composition (Figure 31) of the ice wedge and below shows a Pleistocene signal in the range of other late Pleistocene ice wedges in

Alaska (CREEL Fox tunnel and the Chatanika River valley near Fairbanks (Lachniet et al. 2012; Schirrmeister et al. 2016) and the Barrow permafrost tunnel in Barrow ((Meyer et al. 2010)) and snow in this region (Meyer et al. unpublished data), implying a syngenetic formation. In contrast, the isotopes above the ice wedge show a Holocene and mixed signal of rain and snow (Meyer et al. 2010). The decrease of the isotopes together with the relatively strongly increasing DOC and EC concentration below the ice wedge indicate former thaw- and freezing cycles from both site due a mitigation of ions towards the freezing front, indicating earlier thermokarst processes (Lenz et al. 2016b). The isotopic composition of the active layer sample is in the same range as active layer data from the Seward Peninsula, indicating a summer rain signal (Lenz et al. 2016b). A slightly peat layer with higher TOC and TN contents is located between 57 and 61 cm b.s.l. Strauss et al. (2012) described similar layers in Yedoma deposits in Northeast Sibiria as “paleocryosol”, as patches with plant and wood enrichment. These patches can be caused by more humid and plant growth favouring conditions in the Middle Weichselian 50 – 30 ka BP or in ponding water or boggy environments with increased bioproductivity and low OM decomposition (Schirrmeister et al. 2002; Wetterich et al. 2009; Schirrmeister et al. 2011a; Strauss et al. 2012). This correspondents to the pattern of the stable water isotopes and the DOC and EC concentrations, suggesting former thermokarst processes in the upland (e.g. relict talik), which also explains the slight aquatic influence visible in the biomarker proxies (Section 6.2.2). Grosse et al. (2007) also found fluvial and lacustrine sediments beneath Yedoma in Sibiria). Additionally, the lenticular and horizontal structures, as well as ice veins, as seen in Figure A. 1, indicate a degraded permafrost influences by cryoturbation, frost heave and ice wedge growth. This is in line with the OM proxies showing a decrease in C/N and corresponding increase in $\delta^{13}C$ with depth and general quite low values for CPI and ACL compared to the other sites (Section 6.2.3).

### BAL24-T0-L

The thermokarst lake shows a strong change in the sedimentology and biochemistry, with high water, TOC and TN content, finer grain sizes and stronger lamination above 360 cm b.s.l. and lower water, TOC and TN contents with increasing grain size below. This indicates a shifting input, similar like more aquatic signals in the biomarker proxies (Section 6.2.2), with the end of the lake sediments. This paleo active layer also explains the decrease and subsequent increase of the stable water isotopes. The ages with 0.3 – 2 cal. ka BP point towards the young history of the lake in the Holocene, not older than 0.5 ka as the first

sample above the paleo active layer. Only the sample in 434 cm depth has an age at the border to the Pleistocene with 12 cal. ka BP. As all other depth above and below are much younger, this is more reasonable relocated or reworked material during the lake phase as reworking is unusual in syngenetic sedimentation, but more likely in taliks due volume loss (Jongejans et al. 2018; Jongejans et al. 2020; Farquharson et al. 2022). Along with this is it usual for thermokarst sediments to contain due thaw- and freezing processes radiocarbon ages outside the stratigraphic order (Grosse et al. 2007; Wetterich et al. 2009; Jongejans et al. 2018; Jenrich et al. 2021). Also, the biochemical and biomarker parameters portend to a young lake phase with fast deposition. Their strong variations point to a mixing input during the lake phase. While the partly high C/N, $\delta^{13}C$ and $p_{aq}$, as well as the laminations above the paleo active layer indicate an emergent to terrestrial input due shoreline erosion and thus input of mostly top layers with higher and more recent OM content, there are also layers with more aquatic signals with higher $p_{aq}$ and lower C/N and $\delta^{13}C$ values, resulting from bio productivity in the lake (Anthony et al. 2014; Jongejans et al. 2018). The much coarser material at the bottom is a sign of fluvial influence or ancient thermokarst processes like in the upland, also found in Siberian Yedoma (Grosse et al. 2007; Schirrmeister et al. 2011b; Jongejans et al. 2018; Jenrich et al. 2021) and could represent the glaciomarine and glaciafluvial environment documented in Huston et al. (1990).

### BAL24-T0-DLB

The ages of the DLB are with 50 ka BP the oldest, as deep layers could be reached due the subsidence, with a recent Holocene top layer. Even though DTLBs provide favourable conditions for fast peat accumulation (Jones et al. 2022), the modern peat-layer of DLB with high terrestrial OM ($p_{wax}$ ~9) is with 10 – 15 cm typical low, as it drained just a few years ago (Section 3.2). Similar to UL, DLB shows signs of thaw- and freeze cycles and permafrost degradation as frost-heave and cryoturbation, especially in the active layer with frost cracking and frost desiccation holes. This is in line with the observations from Jones et al. (2023) that the basin was covered with a microtopography indicating melting ice wedges and degrading polygon centres up to 1 m. The unfrozen part on the bottom is the relict of the subaquatic talik during the lake phase, which is not refrozen yet. The massive structure without ice structures in the talik indicate that the whole core column was unfrozen during the lake phase, while the ice veins and lenses indicate refreezing and ice wedge growth after drainage. The shift in the water isotopes from heavier to lighter isotopes confirm a refreezing from top to bottom (Lenz et al. 2016b). The core shows very few signs of the lacustrine phase with

few laminations (Figure A. 3), low OM content and mostly terrestrial inputs ($p_{wax}$ > 0.6, section 6.2.2), which fits to the findings of Jones et al. (2023) that the lake in 1951 still consisted of two small lakes, which coalesced in 1974. Although a talik of more than 2 m is quite large for this short lake phase, it coincides with fast sub-aquatic talik formation, especially at the beginning of the lake phase, with depths of around 10 m after 50 a modelled by Ling and Zhang (2003) and (Kessler et al. (2012). Further floating ice conditions of the former lake could have allowed a year-round talik growth. Only the layer between 13 and 27 cm depth implies a short lacustrine phase, with more macro remains and a horizontal and laminated structure (Figure A. 3). As the depth of 12 cm still has an age of >1 cal. ka BP, this is more likely eroded material from the lake margins. While the stable water isotopes in the bottom half point to a snow, and Pleistocene input, the upper half has a mixed signal between rain and snow with heavier, Holocene signals due the ion mitigation towards the freezing front under the active layer (Figure 31) (Meyer et al. 2010; Lenz et al. 2016b).

### BAL24-T0-M

The top of the marine layer has with the turbated cryostructure visible signs of wave action (Figure A. 4). The high C/N and low $\delta^{13}C$ (14.9 and -26.3 ‰ vs. VPDB in average) in all depths show a clear terrestrial input and thus a deposition under terrestrial conditions. $P_{wax}$ is slightly decreasing with depth, but always >0.68 and thus indicates a terrestrial – palustrine environment more in a slump or flat pond rather than marine, confirmed by the brackish signal of $\delta^{18}O$ and $\delta D$ with mean values of -18.3 and -146.1 ‰ vs. SMOW, respectively (Figure 31). This suggests the sediments were deposited under terrestrial conditions and afterwards overprinted by the ocean due the marine transgression or shoreline erosion, as the Arctic coast has an erosion rate of 0.5 m/a in average and the core shows lamination between 15 and 22 cm b.s.l. This is also confirmed by the EC of the porewater, indicating water of secondary marine infiltration, not during the deposition. The marine core was token beneath the erosion gully of the DLB, therefore the eroded sediments, also indicated by the laminations, could originated from the drainage event, as the sedimentological and biochemical values are similar to DLB. The large pebbles at the bottom of the core are therefore more likely resulting from ancient fluvial or thermokarst processes as also found in UL and TKL (Grosse et al. 2007; Schirrmeister et al. 2011b; Jongejans et al. 2018; Jenrich et al. 2021), than “original” marine sediments due to wave action or tidal forces.

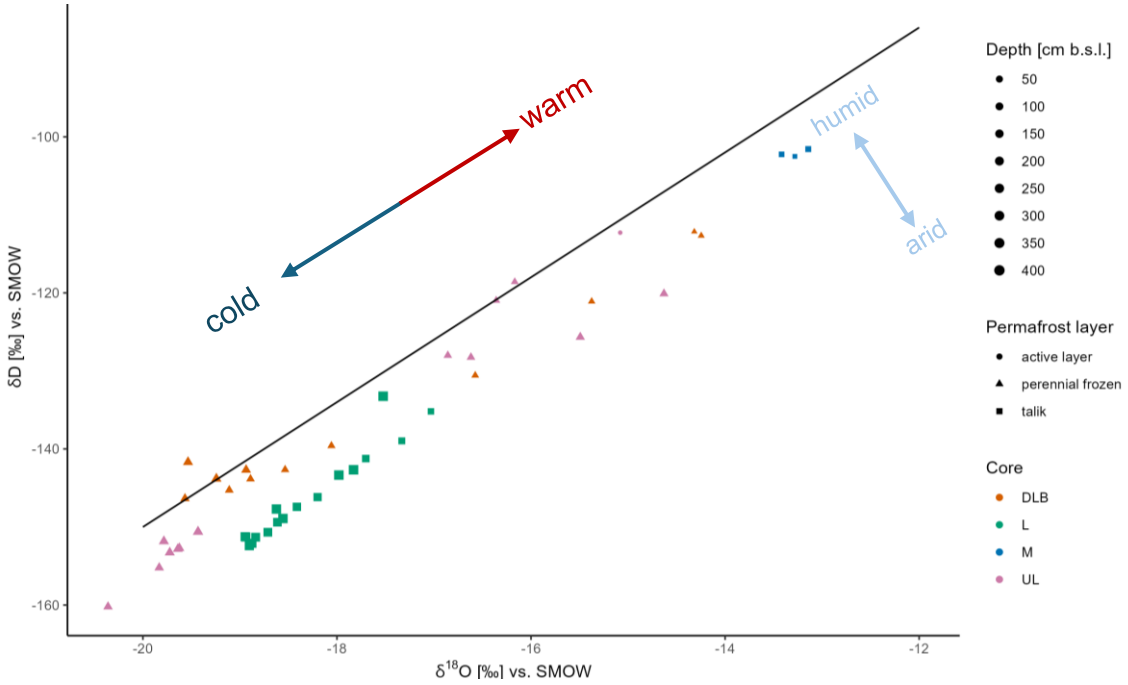


*Figure 31. The δ18O – δD diagram of the four cores compared with the global mean water line (GMWL) after Craig, 1961.*

## 6.2 Organic carbon

The quantity and quality of the OM strongly influences its future degradability (Knoblauch et al. 2013; Strauss et al. 2013; Stapel et al. 2016; Jongejans et al. 2018). Therefore, it is essential not just to know how much carbon is stored, but also the source and quality of it. While the TOC content provides information about the carbon amount, the source can be indicated by C/N and $\delta^{13}C$ as well as the distribution of the n-alkanes by the proxies ACL, $p_{aq}$ and $p_{wax}$, as C/N and $\delta^{13}C$ can be affected by mineralization and degradation (Meyers 1994). Since ACL in this study is also slightly impacted by degradation (Figure 32), this proxy should also be viewed with caution.

### 6.2.1 Organic carbon quantity

As seen in Figure 22. Bulked biogeochemical and hydrochemical parameters for the four cores against depth. The background colours indicate the active layer (yellow), perennial frozen ground (brown), the talik (grey) and the ice wedge (blue), according to the cryolithologically observation due the subsampling. Red arrows for the radiocarbon dating indicate infinite ages.  in section 5.4, the TOC is highest in the terrestrial upland core, with the highest measurement > 40 wt% in the active layer, and decreasing along the transect, with statisti-

cally significant differences between the cores, except DLB and L. The upland has the generally highest TOC values in the active layer and thus the top 100 cm due the active input of recent plants, but even in the bottom half the values are still higher compared to the same depth of the other cores, with a mean of 5.1 ± 1.53 below 100 cm. While the upper half is with 12.28 ± 15.23 wt% in the range of the upland from a study from Fuchs et al. (2019) in North Alaska (29.1 ± 9.7 wt%), the lower half is much lower (28.8 ± 2.2 wt%). Considering the whole core of UL, the mean is with 8.42 wt% much higher than in comparable studies in Alaska (1.95 and 4.66 wt% (Strauss et al. 2013; Giest et al. 2025) and Siberia (3.2, 2.4 and 1.9 wt% (Strauss et al. 2013; Jongejans et al. 2018)), resulting from the high TOC content in the active layer. Regarding therefore the median with 4.75 wt%, the TOC content is similar or slightly higher to other Yedoma sites. The mean TOC of the lake core is with 6.35 wt% in the range of other lake sediment studies in Alaska from Lenz et al. (2016a) (1.6, 7.0 and 5.6 wt% in depth 0 – 100cm), (Giest et al. 2025)5.37 wt%) and (Strauss et al. 2013). The much higher content in the lake sediments (11.32 wt% in upper 352 cm) are likely due the erosion of organic rich active layers in the lake, a higher bioproductivity during the lake phase as well as slow decomposition rates due the cold lake conditions (Strauss et al. 2015; Jongejans et al. 2018) and coincide to the TOC in the upper 30 cm lake sediments from Jongejans et

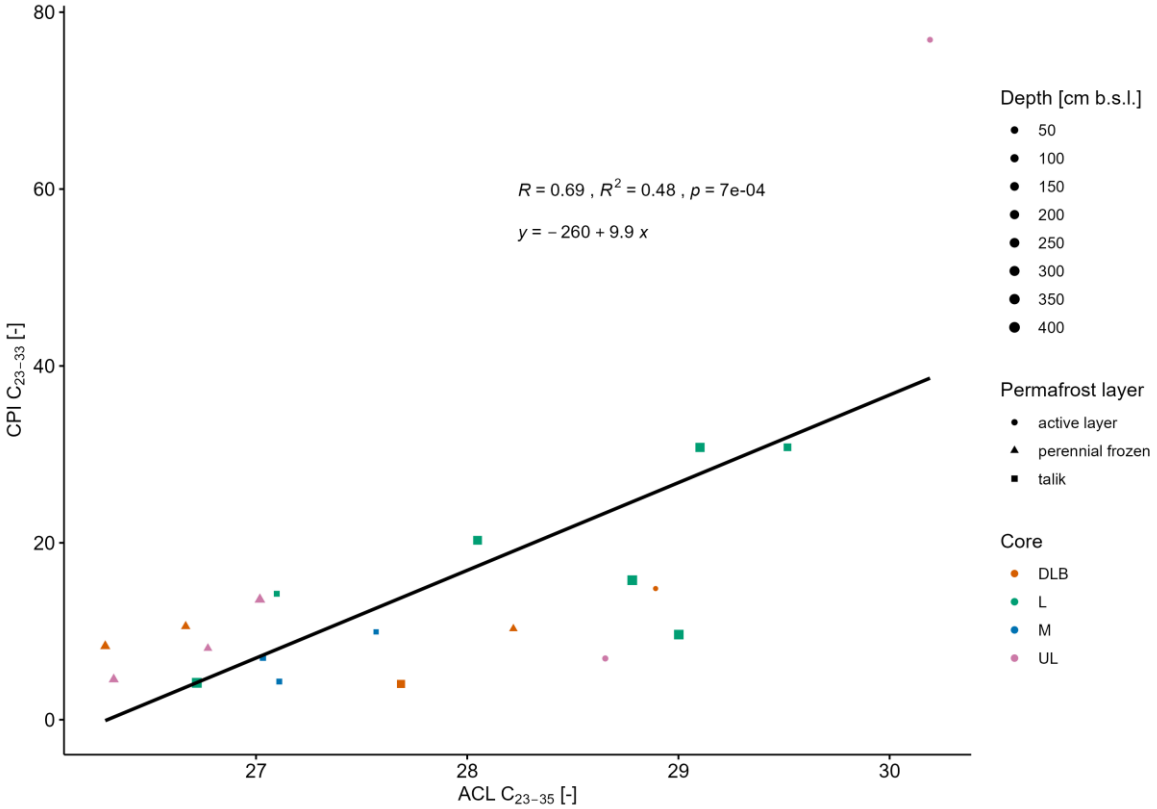


*Figure 32. Scatter plot CPI against ACL. The regression equation, R, $R^2$ and the p-values are shown at the top. The samples of AL are shown as circles, of PF at triangles and of T as squares.*

al. (2018) with a mean of 14.4 wt%. The DLB samples have with 3.12 wt% compared to other studies in North Alaska with 9.75 wt% (Fuchs et al. 2019) and 7.65 wt% (Giest et al. 2025) low TOC contents. The upper 100 cm in particular has significantly lower values with 4.16 ± 3.60 wt% against 11.8 wt% (Giest et al. 2025) and 16 ± 12 wt% (Fuchs et al. 2019). This can be explained by the recent drainage and thus short time for peat accumulation, as Jones et al. (2012) investigated that revegetation starts 5 – 10 years and peat accumulation only 10 – 20 years after drainage. Consequently, the peat layer of our DLB is quite thin with ~10 cm, while Fuchs et al. (2019) measured peat layers of up to 42 cm in old basins (against 12.4 cm in ancient basins) and Giest et al. (2025) of 23 cm in the drained lake basin. The marine core has the lowest TOC concentration with a mean of 1.95 wt% and agrees to the marine sample of Giest et al. (2025) with 1.3 wt%. Furthermore, Jenrich et al. (2021) measured similar concentration in the top 200 cm in a semi-closed lagoon in Northeast Sibiria (1.9 wt%). Comparing the different permafrost layers, TOC is in average with 23.35 wt% highest in the active layer with a large range of 1.85 – 44.42 wt%. In contrast, PF shows the lowest mean TOC content (3.85 wt%), while the mean TOC of T is with 5.7 wt% slightly higher. But even if the values for T and PF are much lower than for AL, they are still in the range of other studies for thermokarst and Yedoma sediments (5.10 wt% for taliks in Alaska (Giest et al. 2025), 6.48 wt% for thermokarst deposits, 3.02 wt% for Yedoma deposits (Strauss et al. 2013)).

### 6.2.2 Organic carbon source

According to Meyers (1994, 1997), our samples are with C/N values from 9.07 to 14.28 between the range of vascular land plants (> 17) and algae (3-9), as seen in Figure 33, while the AL samples from UL are with a C/N > 35 strong terrestrial. General, the samples are less terrestrial the deeper in the soil. This is likely because of degradation then the source (Strauss 13). Our samples fall outside the clear areas of Meyers (1994, 1997), but the same pattern was found in other permafrost studies in Siberia and Alaska (Lenz et al. 2016a; Jongejans et al. 2018; Bischoff 2023; Giest et al. 2025). While the C/N for L and DLB are on median in the range of the ones from Giest et al. (2025) with 13.61 and 12.25 against 14.28 and 13.95, the values for UL and M are much smaller (12.25 vs. 17.57 and 14.48 vs. 25.93). Still the mean values of 14.28, 14.08 and 12.50 for UL, L and DLB are slightly smaller than them from Giest et al. (2025) with 18.45, 14.39 and 17.5. Taking also $\delta^{13}C$ in account with a mean value of -26.36 ‰ vs. VPDB, all samples are in order of land plants (Meyers 1994, 1997)

and similar to the upland and thermokarst lake samples from Giest et al. (2025) with mean values of -27.75 vs. -26.58 (UL) and -28.22 vs. -26.78 ‰ vs. VPDB (L), however the DLB samples of this study have smaller values (25.4 vs. 27.52 ‰ vs. VDPB). Figure 33 exemplifies how the DLB samples are more distributed above (and thus more marine) and the L samples below (more lacustrine) the regression line, while the UL, apart from the two outliers, and M samples are clustered in the middle. However, this variations among the cores could indicate less different OM sources and changing influences than a stronger degradation of the OM (Section 6.2.3), as it was discussed before in section 6.1 that the sites have the same sediment origin. Therefore the OM source will be further discussed based on the biomarker indices ACL, $p_{aq}$ and $p_{wax}$, which are more robust against alteration due degradation (Meyers 1997).

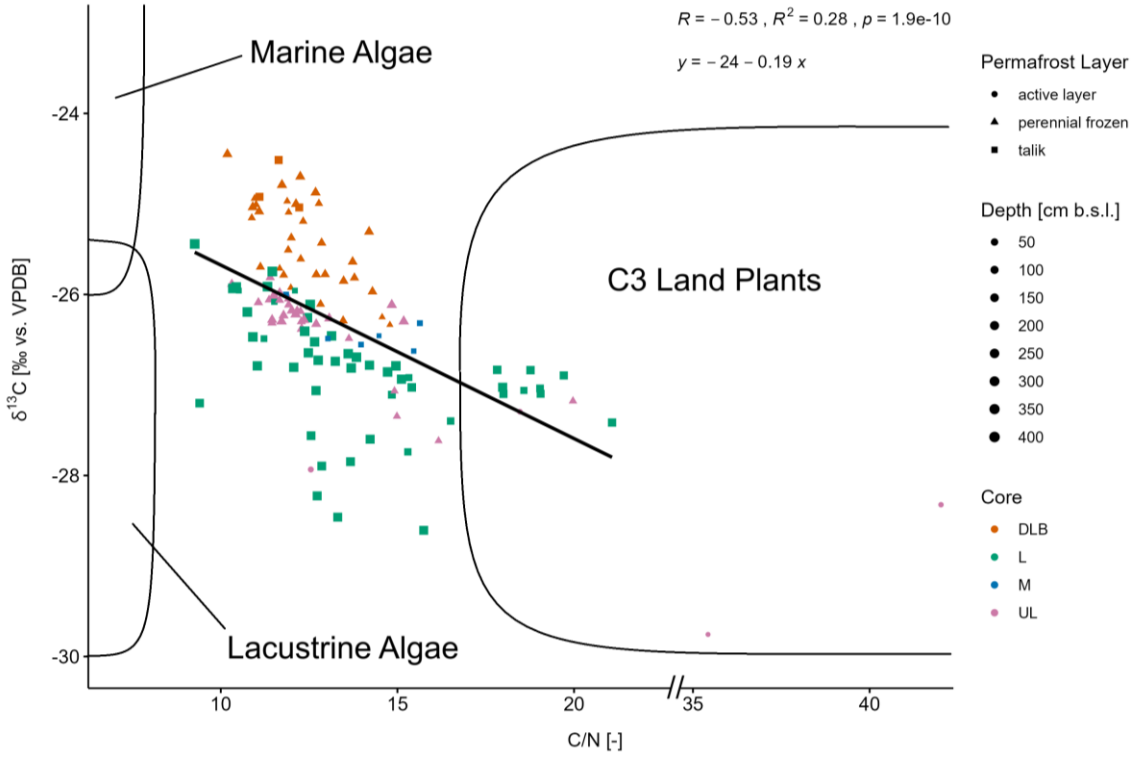


*Figure 33. Scatter plot of $\delta^{13}C$ against C/N. The regression equation, R, $R^2$ and the p-values are shown at the top. The samples of AL are shown as circles, of PF at triangles and of T as squares, the colours represent the cores. Attention for the x-axis break. Regression without AL samples from UL. After Meyer et al. 1997, but identifiers converted with 1.167 * atomic C/N ≈ wt% C/N. DLB sample at 0.5 cm b.s.l. is for clarify reasons not included (δ13C = -36.50 ‰ vs. VPDB and C/N = 11.68).*

Concerning the biomarker proxies for the OM source, illustrates that the odd-and long-chained n-alkanes are dominating, indicating higher land Figure 34 plants, mostly trees and shrubs (27 and 29) and grasses and herbes (31 and 33) for AL, but also some of the L samples, suggesting a tundra vegetation (Poynter and Eglinton 1990; Ficken et al. 1998; Killops and Killops 2009; Zech et al. 2010; Zech et al. 2013). This is confirmed by the ACL which varies between 26 and 30, with the lowest mean value for M and highest mean value for L.

The samples of M, UL and DLB below 100 cm have a similar ACL, while it fluctuates for L between 27 and 31, indicating the different OM inputs in the lake and potential shoreline erosion of fresher, more terrestrial soil with ACL in the range of the top layers of UL and DLB. The slightly increase at the bottom of the DLB and UL cores could be a pointer of the changing hydrological conditions, but also multiple thermokarst generations as discussed in section 6.1. As it could also indicate a vegetational succession from grasses to shrubs, this is unlikely here, as it would be much faster than the sedimentation. The further source proxies $p_{aq}$ and $p_{wax}$ confirm this pattern, $p_{aq}$ vice versa to ACL and $p_{wax}$. The strong correlation between $p_{wax}$ and ACL is shown in Figure 35 and much stronger than between CPI and ACL (Figure 32), indicating ACL here is more a indicator for the OM source than its degeneration. The AL samples as well as most of the deeper L samples are located in the more terrestrial top-right border with high ACL and $p_{wax}$ values, while the deeper UL and DLB and the M

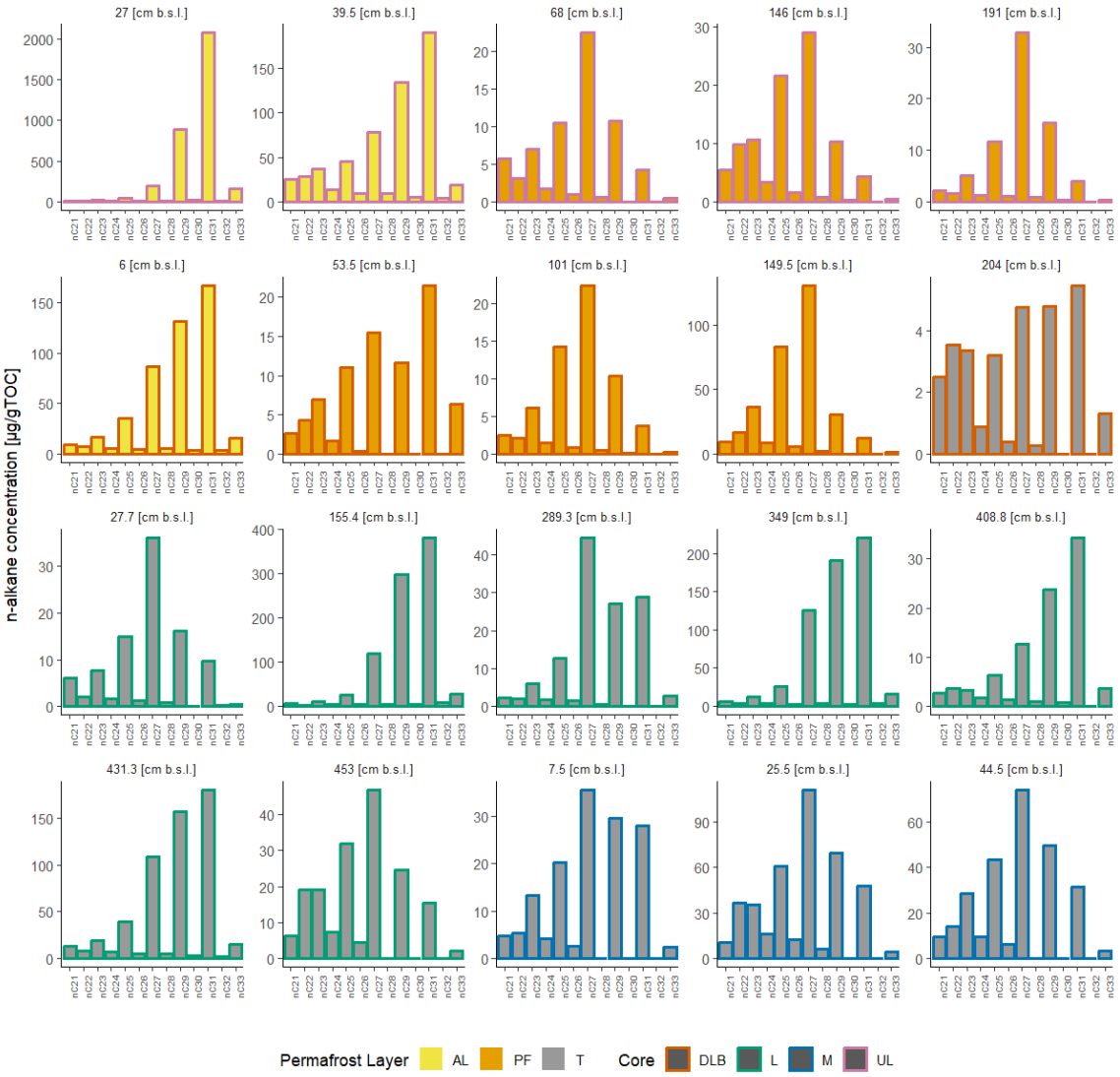


*Figure 34. Chain-length distributions of n-alkanes. The envelope colour displays the related core, the filling colour the related permafrost layer. Note the x-axis scales are independent from each other for better visualization.*

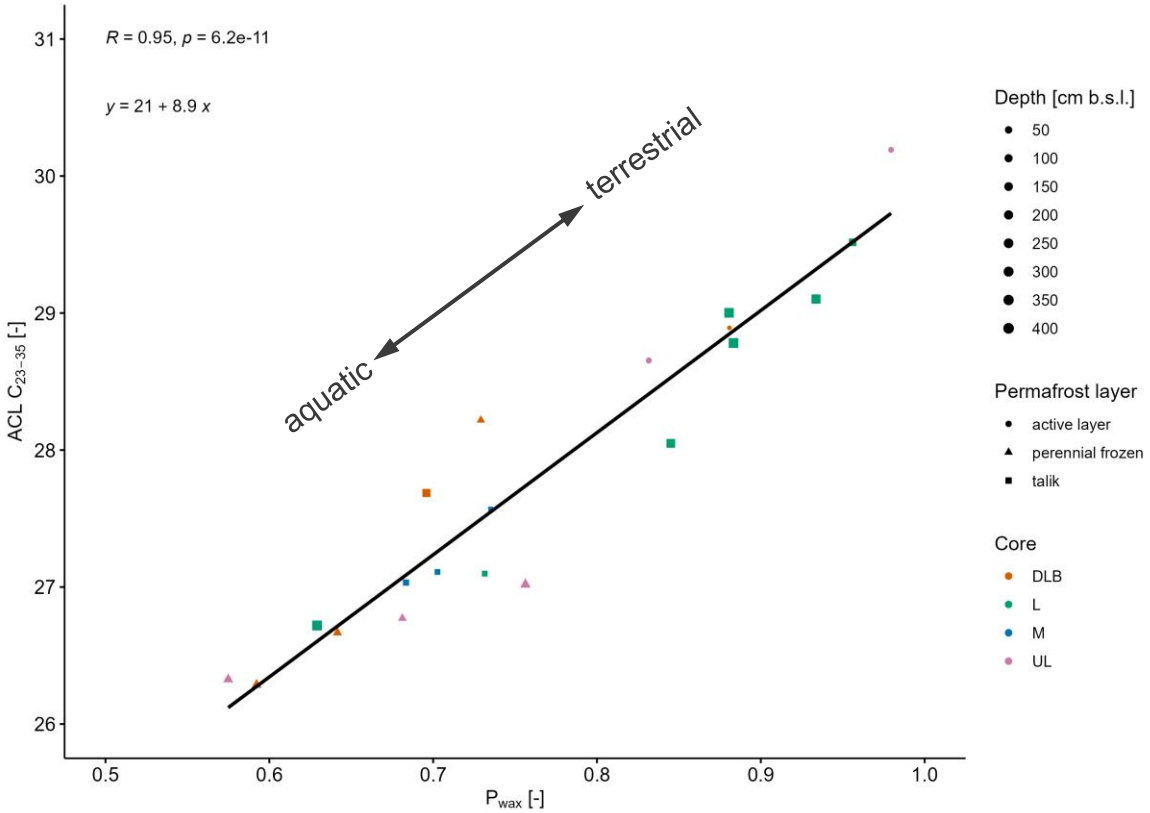


*Figure 35. Scatter plot of ACL against $p_{wax}$. The regression equation, R, $R^2$ and the p-values are shown at the top. The samples of AL are shown as circles, of PF at triangles and of T as squares, the colours represent the cores.*

and the bottom L sample are scattered towards the more aquatic influence with low ALC and $p_{wax}$ values. However, even the values vary between the cores, the differences are not statistically significant for ACL, $p_{wax}$ and $p_{aq}$, neither between all groups as a whole, nor in pairs between the individual groups. This corresponds to the assumptions from section 6.1 assuming the same parent material for all cores. In contrast, the differences between the three permafrost layers in total as well as paired between PF and both the AL and T are statistically significant (Figure 28). The AL samples have the highest terrestrial input (ACL in average 29.25 and $p_{wax}$ in average 0.9), the ones of PF the lowest (26.88 and 0.66). The samples of T are in between with the highest range (26.72 – 29.52 for ACL and 0.63 – 0.96 for $p_{wax}$), but even the PF samples are in the range of terrestrial plants, with a slight influence of emergent macrophytes (Meyers 1997).

## 6.2.3 Organic carbon quality

As discussed in section 6.2.2, C/N and $\delta^{13}C$ are near the range of other studies, but different between the sites. According to the biomarker source proxies, these variances in C/N and $\delta^{13}C$ are more likely because of the OM degradation. OM is selectively degraded, as carbon is more lost as $CO_2$ while nitrogen tends to remain in the sediment, therefore the C/N alters

with decomposition, with higher values suggesting better preservation and lower ratios higher degradation (Strauss et al. 2015). $\delta^{13}C$ becomes less negative with increasing decomposition, as the lighter carbon isotope $^{12}C$ is favoured for microbial decomposition, leading to an enrichment of the heavier isotope $^{13}C$ in the OM. Thus, higher $\delta^{13}C$ values indicate more strongly degraded OM, while lower (more negative) reflects better preserved, less degraded OM (Strauss et al. 2015; Heyer et al. 1976; Skrzypek et al. 2007).

The differences of C/N and $\delta^{13}C$ along all sites were statistically significant but not paired for UL-DLB and L-M (C/N) and UL-M ($\delta^{13}C$). While UL, L and M are on average quite alike (14.08 – 14.88) and higher than for DLB with 12.5, UL has a much lower median with 12.26, and thus even lower than DLB (12.25). This is consistent with the variability for $\delta^{13}C$, where DLB is on median and average higher and statistically significant different from the others. Correspondently to this results, Strauss et al. (2015) also found higher C/N and lower $\delta^{13}C$ mean and median and thus higher quality for thermokarst deposits than for Yedoma.

Additional, Schirrmeister et al. (2011b) states that low TOC and C/N and high $\delta^{13}C$ values are common for Yedoma deposits, as they were deposited in glacial or stadial periods with low bioproductivity (Jongejans et al. 2018).

Regarding the biomarker proxies, the CPI is quite similar for all cores between 8 and 16 in median, while again the lake core shores the best quality. However, the active layer sample in the upland has with 3 442 µg $gTOC^{-1}$ and 76.88 an extremely high n-alkane concentration and CPI compared to other studies. Even though it was taken from the peat layer with high organic content, Ficken et al. (1998) found CPI values only up to 20 for peat soils and fresh bog plants. Jongejans et al. (2018) also found n-alkane concentrations in the range of this sample (1 800 and 16 000 µg $gTOC^{-1}$), but with significantly lower CPI between 5 and 15. Thus, it is possible that the sample could not be completely degreased during extraction because of the very high organic content. This is also supported by the fact that the sample was still very greasy after extraction.

Between the permafrost layers, C/N and $\delta^{13}C$ are statistically significant different, with the highest C/N and lowest $\delta^{13}C$ in the active layer, where the OM is the most fresh and undegraded, as AL is composed of young OM due high input by recent plants and with contemporary peat accumulation and DTLBs favour fast peat accumulation and C sequestration (Jones et al. 2012). The PF shows the strongest degradation with values of 12.55 for C/N and -25.84 ‰ for $\delta^{13}C$ in average, indicating old, degraded OM. The higher quality of the talik compared to the perennial frozen samples may be due (1) shoreline erosion and thus input of fresh material and (2) the consistence of young material, as also shown by the young

$^{14}C$ ages. This is confirmed by the CPI, which shows the same pattern, even though without significant differences. The CPI for the perennial frozen samples is in median 9.3, with values between 4.56 and 13.59, while it is 14.83 (32.88 ± 38.31 on average) and 9.93 (13.73 on average) for the active layer and talik, respectively. And as the PCA reveals, physical properties as grain size and grain size distribution has the strongest impact on variances in the data, it was expected that the differences wouldn't be that high, as the cores have the same origin and thus sedimentology with no clear separation in the PCAs along the cores and permafrost layers, which is also confirmed by the PCAs, where no really separation along the cores and permafrost layers. The slighter higher quality of thermokarst deposits could be explained due a compensation of the degradation processes by input of fresh OM during the Holocene (Strauss et al. 2015). But even though the OM quality proxies differ among the permafrost layers, they are all in median and average higher than 9 in the range of high quality OM (Brassell et al. 1978; Strauss et al. 2015). However, despite that, it should not be neglected that the soil, especially those of the L and M, have due the currently still undecomposed OM a high GHG release potential under further climate warming due the talik formation, especially as they thereby reach the deep, undegraded layers of the permafrost (Strauss et al. 2015).

# 7. Conclusion

Four this study, four cores from the primary permafrost units along a degradation transect were investigated to draw conclusions about the paleoenvironment and the evolution of this thermokarst affected landscape as well as the characterisation of the stored organic matter to access its vulnerability facing a changing Arctic.

The multidisciplinary analysis of permafrost cores from an upland to the coast on the Baldwin Peninsula reveals a consistent sedimentological signal indicating a common sediment origin and a predominance of aeolian deposition. Grain size distributions across all cores are largely unimodal and dominated by poorly sorted coarse silt with slightly secondary peaks in medium sand, confirming loessal origin with minor influences from ancient fluvial or reworked thermokarst processes. The presence of massive ground ice, organic-rich layers, and radiocarbon ages beyond 30–50 ka BP in the deeper cores aligns with characteristics of late Pleistocene Yedoma deposits.

The upland site represents a stable accumulation zone of Pleistocene deposition around 30 cal. ka BP with syngenetic ice-wedge formation and evidence of former thermokarst activity. Layers enriched in peat and TOC between 57–61 cm b.s.l. are similar to Yedoma paleocryosols reported for mid-Weichselian ponding conditions. Cryoturbation features and stable isotope shifts indicate past thaw–freeze cycles and aquatic influences. The thermokarst lake shows a clear transition between the lake and former-lake phase, with finer, laminated sediments with high TOC, TN and aquatic biomarker signals pointing to a young Holocene Lake (0.3–2 ka BP). The anomalously old 12 cal. ka BP sample at 434 cm likely reflects reworked material. Post-lake sedimentation includes terrestrial input through shoreline erosion as well as a high bioproductivity during the lake phase. The drained lake basin allows access to deep Yedoma layers due to thaw subsidence and therefore shows the oldest sediments with ages >50 cal. ka BP but has only a shallow modern peat layer due to its recent drainage. Its soil structure shows frost cracking and cryoturbation. The lower core retains an unfrozen talik as a relic from the former lake, while upper ice veins show renewed permafrost.

The marine core reflects terrestrial deposition later altered by coastal erosion and marine overprint, yet its biomarker and isotopic signatures still point to predominantly terrestrial organic matter. Large basal pebbles likely reflect ancient fluvial or thermokarst processes rather than original marine deposition.

The organic carbon content varies significant between the sites and permafrost layers, with

the highest values in the active layer of the upland and lowest in the marine core. Across permafrost layers, TOC is highest in the active layer and lowest in perennial permafrost. Despite differences in carbon quantity, the origin of organic matter remains dominantly terrestrial, supported by C/N ratios, $\delta^{13}C$ values, and biomarker indices (ACL, $p_{aq}$, $p_{wax}$). Degradation proxies show thermokarst layers generally preserve slightly higher quality OM than cold-stored Yedoma sediments, likely due to high Holocene terrestrial input compensating microbial loss. Nevertheless, all sites show a high-quality OM. The variations between the cores likely reflect differing degradation states rather than fundamentally different OM sources. The Biomarkers support the assumption that all cores derive from a common parent material, consistent with physical sedimentology.

This study enriches the understanding of OM characteristics in thermokarst affected permafrost landscapes by combining sedimentary processes with biochemical indicators. It underlines the vulnerability of former frozen carbon pools in a warming Arctic and supports the need for further approaches to evaluate future carbon feedback as incubation experience or in-situ gas measurements. Especially when regarding the predicted shift from a lake to drained lake landscape in the Artic, it is key to investigate carbon release in drained lake basins to estimate future GHG emissions.

# References

Abdi, Hervé; Williams, Lynne J. (2010): Principal component analysis. In *WIREs Computational Stats* 2 (4), pp. 433–459. DOI: 10.1002/wics.101.

Anthony, K. M. Walter; Zimov, S. A.; Grosse, G.; Jones, M. C.; Anthony, P. M.; Chapin, F. S. et al. (2014): A shift of thermokarst lakes from carbon sources to sinks during the Holocene epoch. In *Nature* 511 (7510), pp. 452–456. DOI: 10.1038/nature13560.

Aré, F. E. (1988a): Thermal abrasion of sea coasts (part I). In *Polar Geography and Geology* 12 (1), p. 1. DOI: 10.1080/10889378809377343.

Aré, F. E. (1988b): Thermal abrasion of sea coasts (Part II). In *Polar Geography and Geology* 12 (2), p. 87. DOI: 10.1080/10889378809377352.

Arp, Christopher D.; Jones, Benjamin M. (2009): Geography of Alaska lake districts: Identification, description, and analysis of lake-rich regions of a diverse and dynamic state. Scientific Investigations Report 2008-5215, 40 pp.

Athy, L. F. (1930): Density, Porosity, and Compaction of Sedimentary Rocks. In *Bulletin* 14. DOI: 10.1306/3D93289E-16B1-11D7-8645000102C1865D.

Ballinger, T. J.; Overland, J. E.; Wang, M.; Bhatt, U. S.; Hanna, E.; Hanssen-Bauer, I. et al. (2020): Arctic Report Card 2020: Surface Air Temperature.

Beer, E.; Eisenman, I.; Wagner, T. J. W. (2020): Polar Amplification Due to Enhanced Heat Flux Across the Halocline. In *Geophysical research letters* 47 (4), Article e2019GL086706. DOI: 10.1029/2019GL086706.

Bintanja, R.; Graversen, R. G.; Hazeleger, W. (2011): Arctic winter warming amplified by the thermal inversion and consequent low infrared cooling to space. In *Nat. Geosci.* 4 (11), pp. 758–761. DOI: 10.1038/ngeo1285.

Bischoff, Verena (2023): Carbon degradation and potential greenhouse gas production in a changing Arctic thermokarst landscape – a case study from drained lake basins on the Yukon Coastal Plain, Canada. Master Thesis. RWTH Aachen University, Alfred-Wegener-Institute. Institute of Geology and Geochemistry of Petroleum and Coal. Available online at https://hdl.handle.net/10013/epic.b1e03365-4db9-4e79-b0ec-8d88225dfac2.

Biskaborn, Boris K.; Smith, Sharon L.; Noetzli, Jeannette; Matthes, Heidrun; Vieira, Gonçalo; Streletskiy, Dmitry A. et al. (2019): Permafrost is warming at a global scale. In

*Nature communications* 10 (1), p. 264. DOI: 10.1038/s41467-018-08240-4.

Blott, Simon J.; Pye, Kenneth (2001): GRADISTAT: a grain size distribution and statistics package for the analysis of unconsolidated sediments. In *Earth Surf Processes Landf* 26 (11), pp. 1237–1248. DOI: 10.1002/esp.261.

Brassell, S. C.; Eglinton, G.; Maxwell, JR; Philp, R. P. (1978): Natural background of alkanes in the aquatic environment. In : Aquatic pollutants: Elsevier, pp. 69–86.

Bray, E.E; Evans, E.D (1961): Distribution of n-paraffins as a clue to recognition of source beds. In *Geochimica et Cosmochimica Acta* 22 (1), pp. 2–15. DOI: 10.1016/0016-7037(61)90069-2.

Bridges, Cecil C. (1966): Hierarchical Cluster Analysis. In *Psychol Rep* 18 (3), pp. 851–854. DOI: 10.2466/pr0.1966.18.3.851.

Buckee, G. K. (1994): Determination of total Nitrogen in Barley, Malt and Beer by Kjeldahl procedures and the dumas combusting method - Collarborative trial. In *Journal of the Institute of Brewing* 100 (2), pp. 57–64. DOI: 10.1002/jib.1994.100.2.57.

Burn, C. R. (2002): Tundra lakes and permafrost, Richards Island, western Arctic coast, Canada. In *Can. J. Earth Sci.* 39 (8), pp. 1281–1298. DOI: 10.1139/e02-035.

Burn, C. R. (2005): Lake-bottom thermal regimes, western Arctic coast, Canada. In *Permafrost and Periglacial Processes* 16 (4), pp. 355–367. DOI: 10.1002/PPP.542.

Burn, Christopher R. (2020): Permafrost Landscape Features. In : Encyclopedia of the World's Biomes: Elsevier, pp. 303–320.

Casas-Prat, Mercè; Wang, Xiaolan L. (2020): Projections of Extreme Ocean Waves in the Arctic and Potential Implications for Coastal Inundation and Erosion. In *JGR Oceans* 125 (8), Article e2019JC015745. DOI: 10.1029/2019JC015745.

Craig, H. (1961): Isotopic Variations in Meteoric Waters. In *Science (New York, N.Y.)* 133 (3465), pp. 1702–1703. DOI: 10.1126/science.133.3465.1702.

Cranwell, P. A.; Eglinton, G.; Robinson, N. (1987): Lipids of aquatic organisms as potential contributors to lacustrine sediments—II. In *Organic Geochemistry* 11 (6), pp. 513–527. DOI: 10.1016/0146-6380(87)90007-6.

Creel, Roger; Guimond, Julia; Jones, Benjamin M.; Nielsen, David M.; Bristol, Emily; Tweedie, Craig E.; Overduin, Pier Paul (2024): Permafrost thaw subsidence, sea-level

rise, and erosion are transforming Alaska's Arctic coastal zone. In *Proceedings of the National Academy of Sciences* 121 (50), e2409411121. DOI: 10.1073/pnas.2409411121.

Dai, Aiguo; Luo, Dehai; Song, Mirong; Liu, Jiping (2019): Arctic amplification is caused by sea-ice loss under increasing CO2. In *Nature communications* 10 (1), p. 121. DOI: 10.1038/s41467-018-07954-9.

Eglinton, Timothy I.; Eglinton, Geoffrey (2008): Molecular proxies for paleoclimatology. In *Earth and Planetary Science Letters* 275 (1-2), pp. 1–16. DOI: 10.1016/j.epsl.2008.07.012.

Farquharson, Louise M.; Romanovsky, Vladimir E.; Kholodov, Alexander; Nicolsky, Dmitry (2022): Sub-aerial talik formation observed across the discontinuous permafrost zone of Alaska. In *Nat. Geosci.* 15 (6), pp. 475–481. DOI: 10.1038/s41561-022-00952-z.

Fedorov, A. N.; Ivanova, R. N.; Park, H.; Hiyama, T.; Iijima, Y. (2014): Recent air temperature changes in the permafrost landscapes of northeastern Eurasia. In *Polar Science* 8 (2), pp. 114–128. DOI: 10.1016/j.polar.2014.02.001.

Ficken, K. J.; Barber, K. E.; Eglinton, G. (1998): Lipid biomarker, δ13C and plant macrofossil stratigraphy of a Scottish montane peat bog over the last two millennia. In *Organic Geochemistry* 28 (3-4), pp. 217–237. DOI: 10.1016/S0146-6380(97)00126-5.

Ficken, K.J; Li, B.; Swain, D.L; Eglinton, G. (2000): An n-alkane proxy for the sedimentary input of submerged/floating freshwater aquatic macrophytes. In *Organic Geochemistry* 31 (7-8), pp. 745–749. DOI: 10.1016/S0146-6380(00)00081-4.

Folk, R. L.; Ward, W. C. (1957): Brazos River bar [Texas]; a study in the significance of grain size parameters. In *Journal of Sedimentary Research* 27 (1), pp. 3–26. DOI: 10.1306/74D70646-2B21-11D7-8648000102C1865D.

French, H.; Shur, Yuri (2010): The principles of cryostratigraphy. In *Earth-Science Reviews* 101 (3), pp. 190–206. DOI: 10.1016/j.earscirev.2010.04.002.

Fuchs, Matthias; Lenz, Josefine; Jock, Suzanne; Nitze, Ingmar; Jones, Benjamin M.; Strauss, Jens et al. (2019): Organic Carbon and Nitrogen Stocks Along a Thermokarst Lake Sequence in Arctic Alaska. In *Journal of geophysical research. Biogeosciences* 124 (5), pp. 1230–1247. DOI: 10.1029/2018JG004591.

Giest, Frieda P.; Jenrich, Maren; Grosse, Guido; Jones, Benjamin M.; Mangelsdorf, Kai;

Windirsch, Torben; Strauss, Jens (2025): Organic carbon, mercury, and sediment characteristics along a land–shore transect in Arctic Alaska. In *Biogeosciences* 22 (12), pp. 2871–2887. DOI: 10.5194/bg-22-2871-2025.

Greenacre, Michael; Groenen, Patrick J. F.; Hastie, Trevor; D'Enza, Alfonso Iodice; Markos, Angelos; Tuzhilina, Elena (2022): Principal component analysis. In *Nat Rev Methods Primers* 2 (1). DOI: 10.1038/s43586-022-00184-w.

Grosse, G.; Jones, B.; Arp, C. (2013): 8.21 Thermokarst Lakes, Drainage, and Drained Basins. In : Treatise on Geomorphology: Elsevier, pp. 325–353.

Grosse, Guido; Harden, Jennifer; Turetsky, Merritt; McGuire, A. David; Camill, Philip; Tarnocai, Charles et al. (2011): Vulnerability of high-latitude soil organic carbon in North America to disturbance. In *J. Geophys. Res.* 116. DOI: 10.1029/2010JG001507.

Grosse, Guido; Schirrmeister, Lutz; Siegert, Christine; Kunitsky, Viktor V.; Slagoda, Elena A.; Andreev, Andrei A.; Dereviagyn, Alexander Y. (2007): Geological and geomorphological evolution of a sedimentary periglacial landscape in Northeast Siberia during the Late Quaternary. In *Geomorphology* 86 (1-2), pp. 25–51. DOI: 10.1016/j.geomorph.2006.08.005.

Hajdas, Irka; Ascough, Philippa; Garnett, Mark H.; Fallon, Stewart J.; Pearson, Charlotte L.; Quarta, Gianluca et al. (2021): Radiocarbon dating. In *Nat Rev Methods Primers* 1 (1). DOI: 10.1038/s43586-021-00058-7.

Heslop, J. K.; Walter Anthony, K. M.; Sepulveda-Jauregui, A.; Martinez-Cruz, K.; Bondurant, A.; Grosse, G.; Jones, M. C. (2015): Thermokarst lake methanogenesis along a complete talik profile. In *Biogeosciences* 12 (14), pp. 4317–4331. DOI: 10.5194/bg-12-4317-2015.

Heyer, J.; Hübner, H.; Maaβ, I. (1976): Isotopenfraktionierung des Kohlenstoffs bei der mikrobiellen Methanbildung. In *Isotopenpraxis Isotopes in Environmental and Health Studies* 12 (5), pp. 202–205. DOI: 10.1080/10256017608543912.

Hinkel, Kenneth M.; Jones, Benjamin M.; Eisner, Wendy R.; Cuomo, Chris J.; Beck, Richard A.; Frohn, Robert (2007): Methods to assess natural and anthropogenic thaw lake drainage on the western Arctic coastal plain of northern Alaska. In *J. Geophys. Res.* 112 (F2), Article 2006JF000584. DOI: 10.1029/2006JF000584.

Hoffman, David W.; Rasmussen, Cornelia (2022): Absolute Carbon Stable Isotope Ratio in

the Vienna Peedee Belemnite Isotope Reference Determined by 1H NMR Spectroscopy. In *Analytical chemistry* 94 (13), pp. 5240–5247. DOI: 10.1021/acs.analchem.1c04565.

Hugelius, G.; Strauss, J.; Zubrzycki, S.; Harden, J. W.; Schuur, E. A. G.; Ping, C.-L. et al. (2014): Estimated stocks of circumpolar permafrost carbon with quantified uncertainty ranges and identified data gaps. In *Biogeosciences* 11 (23), pp. 6573–6593. DOI: 10.5194/bg-11-6573-2014.

Hugelius, Gustaf; Loisel, Julie; Chadburn, Sarah; Jackson, Robert B.; Jones, Miriam; MacDonald, Glen et al. (2020): Large stocks of peatland carbon and nitrogen are vulnerable to permafrost thaw. In *Proceedings of the National Academy of Sciences* 117 (34), pp. 20438–20446. DOI: 10.1073/pnas.1916387117.

Hussey, K. M.; Michelson, R. W. (1966): Tundra relief features near Point Barrow, Alaska. In *Arctic* 19, pp. 162–184. Available online at http://www.jstor.org/stable/40507315.

Huston, Matt M.; Brigham-Grette, Julie; Hopkins, David M. (1990): Paleogeographic Significance of Middle Pleistocene Glaciomarine Deposits on Baldwin Peninsula, Northwest Alaska. In *Ann. Glaciol.* 14, pp. 111–114. DOI: 10.3189/S0260305500008375.

IPCC (Ed.) (2023a): Climate Change 2021: The Physical Science Basis. Contribution of Working Group I to the Sixth Assessment Report of the Intergovernmental Panel on Climate Change. With assistance of V. Masson-Delmotte, P. Zhai, A. Pirani, S. L. Connors, et al.: Cambridge University Press.

IPCC (2023b): Global Carbon and Other Biogeochemical Cycles and Feedbacks. In IPCC (Ed.): Climate Change 2021: The Physical Science Basis. Contribution of Working Group I to the Sixth Assessment Report of the Intergovernmental Panel on Climate Change. With assistance of V. Masson-Delmotte, P. Zhai, A. Pirani, S. L. Connors, et al.: Cambridge University Press, pp. 673–816.

IPCC (2023c): Summary for Policymakers. In IPCC (Ed.): Climate Change 2021: The Physical Science Basis. Contribution of Working Group I to the Sixth Assessment Report of the Intergovernmental Panel on Climate Change. With assistance of V. Masson-Delmotte, P. Zhai, A. Pirani, S. L. Connors, et al.: Cambridge University Press, pp. 3–32.

Irrgang, Anna M.; Bendixen, Mette; Farquharson, Louise M.; Baranskaya, Alisa V.; Erikson, Li H.; Gibbs, Ann E. et al. (2022): Drivers, dynamics and impacts of changing Arctic coasts. In *Nat Rev Earth Environ* 3 (1), pp. 39–54. DOI: 10.1038/s43017-021-00232-1.

# References

ISO, E. (2017): 14688-1: 2017: Geotechnical Investigation and Testing-Identification and Classification of Soil-Part 1: Identification and Description. 2nd ed.: International Organization for Standardization, Geneva.

Jackson, Robert B.; Lajtha, Kate; Crow, Susan E.; Hugelius, Gustaf; Kramer, Marc G.; Piñeiro, Gervasio (2017): The Ecology of Soil Carbon: Pools, Vulnerabilities, and Biotic and Abiotic Controls. In *Annu. Rev. Ecol. Evol. Syst.* 48 (1), pp. 419–445. DOI: 10.1146/annurev-ecolsys-112414-054234.

Jenrich, Maren; Angelopoulos, Michael; Grosse, Guido; Overduin, Pier Paul; Schirrmeister, Lutz; Nitze, Ingmar et al. (2021): Thermokarst Lagoons: A Core-Based Assessment of Depositional Characteristics and an Estimate of Carbon Pools on the Bykovsky Peninsula. In *Front. Earth Sci.* 9, Article 637899. DOI: 10.3389/feart.2021.637899.

Jenrich, Maren; Angelopoulos, Michael; Liebner, Susanne; Treat, Claire; Knoblauch, Christian; Yang, Sizhong et al. (2025): Greenhouse Gas Production and Microbial Response During the Transition From Terrestrial Permafrost to a Marine Environment. In *Permafrost and Periglacial Processes* 36 (1), pp. 63–82. DOI: 10.1002/ppp.2251.

Jolliffe, Ian T.; Cadima, Jorge (2016): Principal component analysis: a review and recent developments. In *Philosophical transactions. Series A, Mathematical, physical, and engineering sciences* 374 (2065), p. 20150202. DOI: 10.1098/rsta.2015.0202.

Jones, B. M.; Grosse, G.; Arp, C. D.; Jones, M. C.; Walter Anthony, K. M.; Romanovsky, V. E. (2011): Modern thermokarst lake dynamics in the continuous permafrost zone, northern Seward Peninsula, Alaska. In *J. Geophys. Res.* 116. DOI: 10.1029/2011JG001666.

Jones, B. M.; Irrgang, A. M.; Farquharson, L. M.; Lantuit, H.; Whalen, D.; Ogorodov, S. et al. (2020a): Arctic Report Card 2020: Coastal Permafrost Erosion.

Jones, Benjamin M.; Arp, Christopher D.; Grosse, Guido; Nitze, Ingmar; Lara, Mark J.; Whitman, Matthew S. et al. (2020b): Identifying historical and future potential lake drainage events on the western Arctic coastal plain of Alaska. In *Permafrost and Periglacial Processes* 31 (1), pp. 110–127. DOI: 10.1002/ppp.2038.

Jones, Benjamin M.; Grosse, Guido; Farquharson, Louise M.; Roy-Léveillée, Pascale; Veremeeva, Alexandra; Kanevskiy, Mikhail Z. et al. (2022): Lake and drained lake basin systems in lowland permafrost regions. In *Nat Rev Earth Environ* 3 (1), pp. 85–98. DOI: 10.1038/s43017-021-00238-9.

Jones, Benjamin M.; Schaeffer Tessier, Susan; Tessier, Tim; Brubaker, Michael; Brook, Mike; Schaeffer, Jackie et al. (2023): Integrating local environmental observations and remote sensing to better understand the life cycle of a thermokarst lake in Arctic Alaska. In *Arctic, Antarctic, and Alpine Research* 55 (1), Article 2195518. DOI: 10.1080/15230430.2023.2195518.

Jones, Benjamin M.; Tape, Ken D.; Clark, Jason A.; Nitze, Ingmar; Grosse, Guido; Disbrow, Jeff (2020c): Increase in beaver dams controls surface water and thermokarst dynamics in an Arctic tundra region, Baldwin Peninsula, northwestern Alaska. In *Environ. Res. Lett.* 15 (7), p. 75005. DOI: 10.1088/1748-9326/ab80f1.

Jones, Miriam C.; Grosse, Guido; Jones, Benjamin M.; Walter Anthony, Katey (2012): Peat accumulation in drained thermokarst lake basins in continuous, ice-rich permafrost, northern Seward Peninsula, Alaska. In *J. Geophys. Res.* 117 (G2), Article 2011JG001766. DOI: 10.1029/2011JG001766.

Jongejans, Loeka L.; Mangelsdorf, Kai; Schirrmeister, Lutz; Grigoriev, Mikhail N.; Maksimov, Georgii M.; Biskaborn, Boris K. et al. (2020): n-Alkane Characteristics of Thawed Permafrost Deposits Below a Thermokarst Lake on Bykovsky Peninsula, Northeastern Siberia. In *Front. Environ. Sci.* 8, Article 118. DOI: 10.3389/fenvs.2020.00118.

Jongejans, Loeka L.; Strauss, Jens; Lenz, Josefine; Peterse, Francien; Mangelsdorf, Kai; Fuchs, Matthias; Grosse, Guido (2018): Organic matter characteristics in yedoma and thermokarst deposits on Baldwin Peninsula, west Alaska. In *Biogeosciences* 15 (20), pp. 6033–6048. DOI: 10.5194/bg-15-6033-2018.

Jorgenson, M. T. (2013): 8.20 Thermokarst Terrains. In : Treatise on Geomorphology: Elsevier, pp. 313–324.

Jorgenson, M. T.; Yoshikawa, K.; Kaneveskiy, M.; Shur, Y. L.; Romanovsky, V. E.; Marchenko, S. S. et al. (Eds.) (2008): Permafrost Characteristics of Alaska. The Ninth International Conference on Permafrost. Fairbanks, Alaska, June 29-July 3, 2008: M. T. Jorgenson, K. Yoshikawa, M. Kaneveskiy, Y. L. Shur, V. E. Romanovsky, S. Marchenko, B. Jones.

Jorgenson, M. Torre; Romanovsky, Vladimir; Harden, Jennifer; Shur, Yuri; O'Donnell, Jonathan; Schuur, Edward A. G. et al. (2010): Resilience and vulnerability of permafrost to climate changeThis article is one of a selection of papers from The Dynamics of Change

in Alaska's Boreal Forests: Resilience and Vulnerability in Response to Climate Warming. In *Can. J. For. Res.* 40 (7), pp. 1219–1236. DOI: 10.1139/X10-060.

Jorgenson, M. Torre; Shur, Yuri L.; Pullman, Erik R. (2006): Abrupt increase in permafrost degradation in Arctic Alaska. In *Geophysical research letters* 33 (2), Article 2005GL024960. DOI: 10.1029/2005GL024960.

Kanevskiy, M.; Shur, Y.; Fortier, D.; Jorgenson, M. T.; Stephani, E. (2011): Cryostratigraphy of late Pleistocene syngenetic permafrost (yedoma) in northern Alaska, Itkillik River exposure. In *Quat. res.* 75 (3), pp. 584–596. DOI: 10.1016/j.yqres.2010.12.003.

Kanevskiy, Mikhail; Jorgenson, Torre; Shur, Yuri; O'Donnell, Jonathan A.; Harden, Jennifer W.; Zhuang, Qianlai; Fortier, Daniel (2014): Cryostratigraphy and Permafrost Evolution in the Lacustrine Lowlands of West-Central Alaska. In *Permafrost and Periglacial Processes* 25 (1), pp. 14–34. DOI: 10.1002/ppp.1800.

Karlstrom, T.N.V. (1964): Surficial Geology of Alaska. U.S. Geological Survey Miscellaneous Geologic Investigations Map 357: Karlstrom, T.N.V.

Kassamara, Alboukadel (2023): ggpubr: 'ggplot2' Based Publication Ready Plots. Version R package version 0. 6. 0. Available online at https://CRAN.R-project.org/package=ggpubr.

Kassamara, Alboukadel; Mundt, Fabian (2020): factoextra: Extract and Visualize the Results of Multivariate Data Analyses. Version R package version 1. 0. 7. Available online at https://CRAN.R-project.org/package=factoextra.

Kessler, M. A.; Plug, L. J.; Walter Anthony, K. M. (2012): Simulating the decadal- to millennial-scale dynamics of morphology and sequestered carbon mobilization of two thermokarst lakes in NW Alaska. In *J. Geophys. Res.* 117 (G2), Article 2011JG001796. DOI: 10.1029/2011JG001796.

Killops, S. D.; Killops, V. J. (2009): Introduction to organic geochemistry: John Wiley & Sons.

Knoblauch, Christian; Beer, Christian; Sosnin, Alexander; Wagner, Dirk; Pfeiffer, Eva-Maria (2013): Predicting long-term carbon mineralization and trace gas production from thawing permafrost of Northeast Siberia. In *Global Change Biology* 19 (4), pp. 1160–1172. DOI: 10.1111/gcb.12116.

Kuhry, Peter; Vitt, Dale H. (1996): Fossil Carbon/Nitrogen Ratios as a Measure of Peat Decomposition. In *Ecology* 77 (1), pp. 271–275. DOI: 10.2307/2265676.

Lachniet, Matthew S.; Lawson, Daniel E.; Sloat, Alison R. (2012): Revised 14 C dating of ice wedge growth in interior Alaska (USA) to MIS 2 reveals cold paleoclimate and carbon recycling in ancient permafrost terrain. In *Quat. res.* 78 (2), pp. 217–225. DOI: 10.1016/j.yqres.2012.05.007.

Lantuit, Hugues; Overduin, Pier Paul; Couture, Nicole; Wetterich, Sebastian; Aré, Felix; Atkinson, David et al. (2012): The Arctic Coastal Dynamics Database: A New Classification Scheme and Statistics on Arctic Permafrost Coastlines. In *Estuaries and Coasts* 35 (2), pp. 383–400. DOI: 10.1007/s12237-010-9362-6.

Lantz, Trevor C.; Kokelj, Steven V. (2008): Increasing rates of retrogressive thaw slump activity in the Mackenzie Delta region, N.W.T., Canada. In *Geophysical research letters* 35 (6), Article 2007GL032433. DOI: 10.1029/2007GL032433.

Lê, Sébastien; Josse, Julie; Husson, François (2008): FactoMineR : An R Package for Multivariate Analysis. In *J. Stat. Soft.* 25 (1). DOI: 10.18637/jss.v025.i01.

Lenz, Josefine; Jones, Benjamin M.; Wetterich, Sebastian; Tjallingii, Rik; Fritz, Michael; Arp, Christopher D. et al. (2016a): Impacts of shore expansion and catchment characteristics on lacustrine thermokarst records in permafrost lowlands, Alaska Arctic Coastal Plain. In *Arktos* 2 (1). DOI: 10.1007/s41063-016-0025-0.

Lenz, Josefine; Wetterich, Sebastian; Jones, Benjamin M.; Meyer, Hanno; Bobrov, Anatoly; Grosse, Guido (2016b): Evidence of multiple thermokarst lake generations from an 11 800-year-old permafrost core on the northern S eward P eninsula, A laska. In *Boreas* 45 (4), pp. 584–603. DOI: 10.1111/bor.12186.

Lim, M.; Whalen, D.; Martin, J.; Mann, P. J.; Hayes, S.; Fraser, P. et al. (2020): Massive Ice Control on Permafrost Coast Erosion and Sensitivity. In *Geophysical research letters* 47 (17), Article e2020GL087917. DOI: 10.1029/2020GL087917.

Ling, Feng; Zhang, Tingjun (2003): Numerical simulation of permafrost thermal regime and talik development under shallow thaw lakes on the Alaskan Arctic Coastal Plain. In *J. Geophys. Res.* 108 (D16), Article 2002JD003014. DOI: 10.1029/2002JD003014.

Lisiecki, Lorraine E.; Herbert, Timothy D. (2007): Automated composite depth scale construction and estimates of sediment core extension. In *Paleoceanography* 22 (4), Article

2006PA001401. DOI: 10.1029/2006PA001401.

Macander, Matthew J.; Swingley, Christopher S.; Joly, Kyle; Raynolds, Martha K. (2015): Landsat-based snow persistence map for northwest Alaska. In *Remote Sensing of Environment* 163, pp. 23–31. DOI: 10.1016/j.rse.2015.02.028.

Malenfant, François; Whalen, D.; Fraser, P.; van Proosdij, D. (2022): Rapid coastal erosion of ice-bonded deposits on Pelly Island, southeastern Beaufort Sea, Inuvialuit Settlement Region, western Canadian Arctic. In *Can. J. Earth Sci.* 59 (11), pp. 961–972. DOI: 10.1139/cjes-2021-0118.

Marzi, R.; Torkelson, B. E.; Olson, R. K. (1993): A revised carbon preference index. In *Organic Geochemistry* 20 (8), pp. 1303–1306. DOI: 10.1016/0146-6380(93)90016-5.

McGuire, A. David; Lawrence, David M.; Koven, Charles; Clein, Joy S.; Burke, Eleanor; Chen, Guangsheng et al. (2018): Dependence of the evolution of carbon dynamics in the northern permafrost region on the trajectory of climate change. In *Proceedings of the National Academy of Sciences* 115 (15), pp. 3882–3887. DOI: 10.1073/pnas.1719903115.

Meyer, Hanno; Schirrmeister, Lutz; Andreev, Andrei; Wagner, Dirk; Hubberten, Hans-W.; Yoshikawa, Kenji et al. (2010): Lateglacial and Holocene isotopic and environmental history of northern coastal Alaska – Results from a buried ice-wedge system at Barrow. In *Quaternary Science Reviews* 29 (27-28), pp. 3720–3735. DOI: 10.1016/j.quascirev.2010.08.005.

Meyers, Philip A. (1994): Preservation of elemental and isotopic source identification of sedimentary organic matter. In *Chemical Geology* 114 (3-4), pp. 289–302. DOI: 10.1016/0009-2541(94)90059-0.

Meyers, Philip A. (1997): Organic geochemical proxies of paleoceanographic, paleolimnologic, and paleoclimatic processes. In *Organic Geochemistry* 27 (5-6), pp. 213–250. DOI: 10.1016/S0146-6380(97)00049-1.

Meyers, Philip A. (2003): Applications of organic geochemistry to paleolimnological reconstructions: a summary of examples from the Laurentian Great Lakes. In *Organic Geochemistry* 34 (2), pp. 261–289. DOI: 10.1016/S0146-6380(02)00168-7.

Miesner, F.; Overduin, P. P.; Grosse, G.; Strauss, J.; Langer, M.; Westermann, S. et al. (2023): Subsea permafrost organic carbon stocks are large and of dominantly low reactivity. In

*Scientific reports* 13 (1), p. 9425. DOI: 10.1038/s41598-023-36471-z.

Mollenhauer, Gesine; Grotheer, Hendrik; Gentz, Torben; Bonk, Elizabeth; Hefter, Jens (2021): Standard operation procedures and performance of the MICADAS radiocarbon laboratory at Alfred Wegener Institute (AWI), Germany. In *Nuclear Instruments and Methods in Physics Research Section B: Beam Interactions with Materials and Atoms* 496, pp. 45–51. DOI: 10.1016/j.nimb.2021.03.016.

Moon, Twila A.; Tedesco, M.; Box, J. E.; Cappelen, J.; Fausto, R. S.; Fettweis, X. et al. (2020): Arctic Report Card 2020: Greenland Ice Sheet.

Morgenstern, A.; Grosse, G.; Günther, F.; Fedorova, I.; Schirrmeister, L. (2011): Spatial analyses of thermokarst lakes and basins in Yedoma landscapes of the Lena Delta. In *The Cryosphere* 5 (4), pp. 849–867. DOI: 10.5194/tc-5-849-2011.

Nitze, Ingmar; Cooley, Sarah W.; Duguay, Claude R.; Jones, Benjamin M.; Grosse, Guido (2020): The catastrophic thermokarst lake drainage events of 2018 in northwestern Alaska: fast-forward into the future. In *The Cryosphere* 14 (12), pp. 4279–4297. DOI: 10.5194/tc-14-4279-2020.

Obu, Jaroslav; Lantuit, Hugues; Grosse, Guido; Günther, Frank; Sachs, Torsten; Helm, Veit; Fritz, Michael (2017): Coastal erosion and mass wasting along the Canadian Beaufort Sea based on annual airborne LiDAR elevation data. In *Geomorphology* 293, pp. 331–346. DOI: 10.1016/j.geomorph.2016.02.014.

Obu, Jaroslav; Westermann, Sebastian; Bartsch, Annett; Berdnikov, Nikolai; Christiansen, Hanne H.; Dashtseren, Avirmed et al. (2019): Northern Hemisphere permafrost map based on TTOP modelling for 2000–2016 at 1 km2 scale. In *Earth-Science Reviews* 193, pp. 299–316. DOI: 10.1016/j.earscirev.2019.04.023.

Ohara, Noriaki; Jones, Benjamin M.; Parsekian, Andrew D.; Hinkel, Kenneth M.; Yamatani, Katsu; Kanevskiy, Mikhail et al. (2022): A new Stefan equation to characterize the evolution of thermokarst lake and talik geometry. In *The Cryosphere* 16 (4), pp. 1247–1264. DOI: 10.5194/tc-16-1247-2022.

Olefeldt, D.; Goswami, S.; Grosse, G.; Hayes, D.; Hugelius, G.; Kuhry, P. et al. (2016): Circumpolar distribution and carbon storage of thermokarst landscapes. In *Nature communications* 7, p. 13043. DOI: 10.1038/ncomms13043.

Otto, Angelika; Simpson, Myrna J. (2005): Degradation and Preservation of Vascular Plant-

derived Biomarkers in Grassland and Forest Soils from Western Canada. In *Biogeochemistry* 74 (3), pp. 377–409. DOI: 10.1007/s10533-004-5834-8.

Parazoo, Nicholas C.; Koven, Charles D.; Lawrence, David M.; Romanovsky, Vladimir; Miller, Charles E. (2018): Detecting the permafrost carbon feedback: talik formation and increased cold-season respiration as precursors to sink-to-source transitions. In *The Cryosphere* 12 (1), pp. 123–144. DOI: 10.5194/tc-12-123-2018.

Parsekian, Andrew D.; Grosse, Guido; Walbrecker, Jan O.; Müller-Petke, Mike; Keating, Kristina; Liu, Lin et al. (2013): Detecting unfrozen sediments below thermokarst lakes with surface nuclear magnetic resonance. In *Geophysical research letters* 40 (3), pp. 535–540. DOI: 10.1002/grl.50137.

Parsekian, Andrew D.; Jones, Benjamin M.; Jones, Miriam; Grosse, Guido; Walter Anthony, Katey M.; Slater, Lee (2011): Expansion rate and geometry of floating vegetation mats on the margins of thermokarst lakes, northern Seward Peninsula, Alaska, USA. In *Earth Surf Processes Landf* 36 (14), pp. 1889–1897. DOI: 10.1002/esp.2210.

Perovich, Donald; Meier, W.; Tschudi, M.; Hendricks, S.; Petty, A. A.; Divine, D. et al. (2020): Arctic Report Card 2020: Sea Ice.

Péwé, Troy Lewis (1975): Quaternary Geology of Alaska. U.S. Govt. Print. Off. (Professional Paper, 835).

Ping, C. L.; Jastrow, J. D.; Jorgenson, M. T.; Michaelson, G. J.; Shur, Y. L. (2015): Permafrost soils and carbon cycling. In *SOIL* 1 (1), pp. 147–171. DOI: 10.5194/soil-1-147-2015.

Pithan, Felix; Mauritsen, Thorsten (2014): Arctic amplification dominated by temperature feedbacks in contemporary climate models. In *Nat. Geosci.* 7 (3), pp. 181–184. DOI: 10.1038/NGEO2071.

Posit team (2024): RStudio: Integrated Developement Environment for R. Version 2023.12.1.402. Boston, MA: Posit Software, PBC. Available online at http://www.posit.co/.

Poynter, J.; Eglinton, G. (1990): Molecular Composition of Three Sediments from Hole 717C: The Bengal Fan. In J. R. Cochran, D.A.V. Stow (Eds.): Proceedings of the Ocean Drilling Program, 116 Scientific Results, vol. 116: Ocean Drilling Program (Proceedings of the Ocean Drilling Program, 116).

# References

Radke, M.; Willsch, H.; Welte, D. W. (1980): Preparative hydrocarbon group type determination by automatic medium pressure liquid chromatography. In *Analytical chemistry* 52 (3), pp. 406–411.

Rantanen, Mika; Karpechko, Alexey Yu.; Lipponen, Antti; Nordling, Kalle; Hyvärinen, Otto; Ruosteenoja, Kimmo et al. (2022): The Arctic has warmed nearly four times faster than the globe since 1979. In *Commun Earth Environ* 3 (1). DOI: 10.1038/s43247-022-00498-3.

Reimer, Paula J.; Bard, Edouard; Bayliss, Alex; Beck, J. Warren; Blackwell, Paul G.; Ramsey, Christopher Bronk et al. (2013): IntCal13 and Marine13 Radiocarbon Age Calibration Curves 0–50,000 Years cal BP. In *Radiocarbon* 55 (4), pp. 1869–1887. DOI: 10.2458/azu_js_rc.55.16947.

Rey, David M.; Walvoord, Michelle A.; Minsley, Burke J.; Ebel, Brian A.; Voss, Clifford I.; Singha, Kamini (2020): Wildfire-Initiated Talik Development Exceeds Current Thaw Projections: Observations and Models From Alaska's Continuous Permafrost Zone. In *Geophysical research letters* 47 (15), Article e2020GL087565. DOI: 10.1029/2020GL087565.

Romanovskii, N. N.; Hubberten, H. W.; Gavrilov, A. V.; Tumskoy, V. E.; Kholodov, A. L. (2004): Permafrost of the east Siberian Arctic shelf and coastal lowlands. In *Quaternary Science Reviews* 23 (11-13), pp. 1359–1369. DOI: 10.1016/j.quascirev.2003.12.014.

Schaeffer, Kevin; Zhang, Tinjun; Bruhwiler, Lori, Barrett, Andrew. P (2011): Amount and timing of permafrost carbon release in response to climate warming. In *Tellus B* 63 (2), pp. 165–180. DOI: 10.1111/j.1600-0889.2011.00527.x.

Schirrmeister, L.; Froese, D.; Tumskoy, V.; Grosse, G.; Wetterich, S. (2013): PERMAFROST AND PERIGLACIAL FEATURES | Yedoma: Late Pleistocene Ice-Rich Syngenetic Permafrost of Beringia. In A. Elias Scott, J. Mock Cary (Eds.): Encyclopedia of Quaternary Science. 2nd ed.: Elsevier, pp. 542–552. Available online at https://www.sciencedirect.com/science/article/pii/B9780444536433001060.

Schirrmeister, L.; Kunitsky, V.; Grosse, G.; Wetterich, S.; Meyer, H.; Schwamborn, G. et al. (2011a): Sedimentary characteristics and origin of the Late Pleistocene Ice Complex on north-east Siberian Arctic coastal lowlands and islands – A review. In *Quaternary International* 241 (1-2), pp. 3–25. DOI: 10.1016/j.quaint.2010.04.004.

# References

Schirrmeister, Lutz; Dietze, Elisabeth; Matthes, Heidrun; Grosse, Guido; Strauss, Jens; Laboor, Sebastian et al. (2020): The genesis of Yedoma Ice Complex permafrost – grain-size endmember modeling analysis from Siberia and Alaska. In *E&G Quaternary Sci. J.* 69 (1), pp. 33–53. DOI: 10.5194/egqsj-69-33-2020.

Schirrmeister, Lutz; Froese, Duane; Wetterich, Sebastian; Strauss, Jens; Veremeeva, Aleksandra; Grosse, Guido (2025): Yedoma: Late Pleistocene ice-rich syngenetic permafrost of Beringia. In : Encyclopedia of Quaternary Science: Elsevier, pp. 296–311.

Schirrmeister, Lutz; Grosse, Guido; Wetterich, Sebastian; Overduin, Pier Paul; Strauss, Jens; Schuur, Edward A. G.; Hubberten, Hans-Wolfgang (2011b): Fossil organic matter characteristics in permafrost deposits of the northeast Siberian Arctic. In *J. Geophys. Res.* 116. DOI: 10.1029/2011JG001647.

Schirrmeister, Lutz; Meyer, Hanno; Andreev, Andrei; Wetterich, Sebastian; Kienast, Frank; Bobrov, Anatoly et al. (2016): Late Quaternary paleoenvironmental records from the Chatanika River valley near Fairbanks (Alaska). In *Quaternary Science Reviews* 147, pp. 259–278. DOI: 10.1016/j.quascirev.2016.02.009.

Schirrmeister, Lutz; Siegert, Christine; Kuznetsova, Tatyana; Kuzmina, Svetlana; Andreev, Andrei; Kienast, Frank et al. (2002): Paleoenvironmental and paleoclimatic records from permafrost deposits in the Arctic region of Northern Siberia. In *Quaternary International* 89 (1), pp. 97–118. DOI: 10.1016/S1040-6182(01)00083-0.

Schuur, E. A. G.; Abbott, B. W.; Bowden, W. B.; Brovkin, V.; Camill, P.; Canadell, J. G. et al. (2013): Expert assessment of vulnerability of permafrost carbon to climate change. In *Climatic Change* 119 (2), pp. 359–374. DOI: 10.1007/s10584-013-0730-7.

Schuur, Edward A. G.; Bockheim, James; Canadell, Josep G.; Euskirchen, Eugenie; Field, Christopher B.; Goryachkin, Sergey V. et al. (2008): Vulnerability of Permafrost Carbon to Climate Change: Implications for the Global Carbon Cycle. In *BioScience* 58 (8), pp. 701–714. DOI: 10.1641/B580807.

Schuur, Edward A.G.; Abbott, Benjamin W.; Commane, Roisin; Ernakovich, Jessica; Euskirchen, Eugenie; Hugelius, Gustaf et al. (2022): Permafrost and Climate Change: Carbon Cycle Feedbacks From the Warming Arctic. In *Annu. Rev. Environ. Resour.* 47 (1), pp. 343–371. DOI: 10.1146/annurev-environ-012220-011847.

Screen, James A.; Simmonds, Ian (2010): The central role of diminishing sea ice in recent

Arctic temperature amplification. In *Nature* 464 (7293), pp. 1334–1337. DOI: 10.1038/nature09051.

Shetty, Pranav; Singh, Suraj (2021): Hierarchical Clustering: A Survey. In *Int. J. Appl. Res.* 7 (4), pp. 178–181. DOI: 10.22271/allresearch.2021.v7.i4c.8484.

Skrzypek, Grzegorz; Kałużny, Adam; Wojtuń, Bronisław; Jędrysek, Mariusz-Orion (2007): The carbon stable isotopic composition of mosses: A record of temperature variation. In *Organic Geochemistry* 38 (10), pp. 1770–1781. DOI: 10.1016/j.orggeochem.2007.05.002.

Smith, Sharon L.; O'Neill, H. Brendan; Isaksen, Ketil; Noetzli, Jeannette; Romanovsky, Vladimir E. (2022): The changing thermal state of permafrost. In *Nat Rev Earth Environ* 3 (1), pp. 10–23. DOI: 10.1038/s43017-021-00240-1.

Stapel, J. G.; Schirrmeister, L.; Overduin, P. P.; Wetterich, S.; Strauss, J.; Horsfield, B.; Mangelsdorf, K. (2016): Microbial lipid signatures and substrate potential of organic matter in permafrost deposits: Implications for future greenhouse gas production. In *Journal of geophysical research. Biogeosciences* 121 (10), pp. 2652–2666. DOI: 10.1002/2016JG003483.

Strauss, J.; Abbott, Benjamin W.; Hugelius, G.; Schuur, E. A. G.; Treat, C. C.; Fuchs, Matthias et al. (2021a): 9. Permafrost. In *Recarbonizing global soils - A technical manuel of recommended management practices.* 2, pp. 130–146.

Strauss, J.; Schirrmeister, L.; Mangelsdorf, K.; Eichhorn, L.; Wetterich, S.; Herzschuh, U. (2015): Organic-matter quality of deep permafrost carbon – a study from Arctic Siberia. In *Biogeosciences* 12 (7), pp. 2227–2245. DOI: 10.5194/bg-12-2227-2015.

Strauss, Jens; Fuchs, Matthias; Hugelius, Gustaf; Miesner, Frederieke; Nitze, Ingmar; Opfergelt, Sophie et al. (2025): Organic matter storage and vulnerability in the permafrost domain. In : Encyclopedia of Quaternary Science: Elsevier, pp. 399–410.

Strauss, Jens; Laboor, Sebastian; Schirrmeister, Lutz; Fedorov, Alexander N.; Fortier, Daniel; Froese, Duane et al. (2021b): Circum-Arctic Map of the Yedoma Permafrost Domain. In *Front. Earth Sci.* 9, Article 758360. DOI: 10.3389/feart.2021.758360.

Strauss, Jens; Schirrmeister, Lutz; Grosse, Guido; Fortier, Daniel; Hugelius, Gustaf; Knoblauch, Christian et al. (2017): Deep Yedoma permafrost: A synthesis of depositional characteristics and carbon vulnerability. In *Earth-Science Reviews* 172, pp. 75–

86. DOI: 10.1016/j.earscirev.2017.07.007.

Strauss, Jens; Schirrmeister, Lutz; Grosse, Guido; Wetterich, Sebastian; Ulrich, Mathias; Herzschuh, Ulrike; Hubberten, Hans-Wolfgang (2013): The deep permafrost carbon pool of the Yedoma region in Siberia and Alaska. In *Geophysical research letters* 40 (23), pp. 6165–6170. DOI: 10.1002/2013GL058088.

Strauss, Jens; Schirrmeister, Lutz; Wetterich, Sebastian; Borchers, Andreas; Davydov, Sergei P. (2012): Grain-size properties and organic-carbon stock of Yedoma Ice Complex permafrost from the Kolyma lowland, northeastern Siberia. In *Global Biogeochemical Cycles* 26 (3), Article 2011GB004104. DOI: 10.1029/2011GB004104.

Stuecker, Malte F.; Bitz, Cecilia M.; Armour, Kyle C.; Proistosescu, Cristian; Kang, Sarah M.; Xie, Shang-Ping et al. (2018): Polar amplification dominated by local forcing and feedbacks. In *Nature Clim Change* 8 (12), pp. 1076–1081. DOI: 10.1038/s41558-018-0339-y.

Tagliapietra, Davide; Sigovini, Marco; Ghirardini, Annamaria Volpi (2009): A review of terms and definitions to categorise estuaries, lagoons and associated environments. In *Mar. Freshwater Res.* 60 (6), p. 497. DOI: 10.1071/MF08088.

Taylor, Patrick C.; Cai, Ming; Hu, Aixue; Meehl, Jerry; Washington, Warren; Zhang, Guang J. (2013): A Decomposition of Feedback Contributions to Polar Warming Amplification. In *Journal of Climate* 26 (18), pp. 7023–7043. DOI: 10.1175/JCLI-D-12-00696.1.

Tessier, S.; Forbes, B.; Grosse, G.; Jones, B. M.; Nitze, I.; Schaeffer, J. (2022): Sudden lake drainage event - Local Environment Observer (LEO) Network [online]. Available online at https://www.leonetwork.org/en/posts/show/DC4753BF-6270-46EE-816B-6B97C36B30D3, checked on 7/11/2025.

Timmermans, Mary-Louise; Labe, Z. (2020): Arctic Report Card 2020: Sea Surface Temperature.

Treat, Claire C.; Jones, Miriam C.; Alder, Jay; Sannel, A. Britta K.; Camill, Philip; Frolking, Steve (2021): Predicted Vulnerability of Carbon in Permafrost Peatlands With Future Climate Change and Permafrost Thaw in Western Canada. In *Journal of geophysical research. Biogeosciences* 126 (5), Article e2020JG005872. DOI: 10.1029/2020JG005872.

Uchenna, O. E.; Olusola, M. O. (2024): Overview of Agglomerative Hierarchical Clustering

Methods. In *British Journal of Computer, Networking and Information Technology* 7 (2), pp. 14–23. DOI: 10.52589/BJCNIT-CV9POOGW.

van Everdingen, R. O. (2005): Multi-language Glossary of Permafrost and Related Ground-ice Terms in Multi-language Glossary of Permafrost and Related Ground-ice Terms in Chinese, English, French, German, Icelandic, Italian, Norwegian, Polish, Romanian, Spanish, and Swedish: Arctic Inst. of North America University of Calgary.

Vries, HL. de; Barendsen, G. W. (1954): Measurements of Age by the Carbon-14 Technique. In *Nature* 174 (4442), pp. 1138–1141. DOI: 10.1038/1741138a0.

Walker, Donald A.; Raynolds, Martha K.; Daniëls, Fred J.A.; Einarsson, Eythor; Elvebakk, Arve; Gould, William A. et al. (2005): The Circumpolar Arctic vegetation map. In *J Vegetation Science* 16 (3), pp. 267–282. DOI: 10.1111/j.1654-1103.2005.tb02365.x.

Walter, K. M.; Zimov, S. A.; Chanton, J. P.; Verbyla, D.; Chapin, F. S. (2006): Methane bubbling from Siberian thaw lakes as a positive feedback to climate warming. In *Nature* 443 (7107), pp. 71–75. DOI: 10.1038/nature05040.

Walter Anthony, Katey; Daanen, Ronald; Anthony, Peter; Schneider von Deimling, Thomas; Ping, Chien-Lu; Chanton, Jeffrey P.; Grosse, Guido (2016): Methane emissions proportional to permafrost carbon thawed in Arctic lakes since the 1950s. In *Nat. Geosci.* 9 (9), pp. 679–682. DOI: 10.1038/ngeo2795.

Walter Anthony, Katey; Schneider von Deimling, Thomas; Nitze, Ingmar; Frolking, Steve; Emond, Abraham; Daanen, Ronald et al. (2018): 21st-century modeled permafrost carbon emissions accelerated by abrupt thaw beneath lakes. In *Nature communications* 9 (1), p. 3262. DOI: 10.1038/s41467-018-05738-9.

Walter Anthony, Katey M.; Anthony, Peter (2013): Constraining spatial variability of methane ebullition seeps in thermokarst lakes using point process models. In *Journal of geophysical research. Biogeosciences* 118 (3), pp. 1015–1034. DOI: 10.1002/jgrg.20087.

Wei, Taiyun; Simko, Viliam (2024): R package 'corrplot': visualization of a Correlation Matrix. Version Version 0.95. Available online at https://github.com/taiyun/corrplot.

Wetterich, Sebastian; Schirrmeister, Lutz; Andreev, Andrei A.; Pudenz, Michael; Plessen, Birgit; Meyer, Hanno; Kunitsky, Viktor V. (2009): Eemian and Late Glacial/Holocene palaeoenvironmental records from permafrost sequences at the Dmitry Laptev Strait

(NE Siberia, Russia). In *Palaeogeography, Palaeoclimatology, Palaeoecology* 279 (1-2), pp. 73–95. DOI: 10.1016/j.palaeo.2009.05.002.

Wickham, Hadley (2016): ggplot2: elegant graphics for Data Analysis. New York: Springer Verlag. Available online at https://ggplot2.tidyverse.org.

Wickland, K. P.; O'Donnell, J. A.; Koch, J. C.; Jorgenson, M. T.; Harden, J. W.; Striegl, Robert G.; Anderson, L. (Eds.) (2009): Fate of Carbon in Sediments of a Drying High Latitude Lake, Interior Alaska. Eos Trans. AGU. p. 90(52), fall Meet. Suppl. Abstract U41C–0057.

Woods, Cian; Caballero, Rodrigo (2016): The Role of Moist Intrusions in Winter Arctic Warming and Sea Ice Decline. In *Journal of Climate* 29 (12), pp. 4473–4485. DOI: 10.1175/JCLI-D-15-0773.1.

Zech, Michael; Buggle, Björn; Leiber, Katharina; Marković, Slobodan; Glaser, Bruno; Hambach, Ulrich et al. (2010): Reconstructing Quaternary vegetation history in the Carpathian Basin, SE-Europe, using n-alkane biomarkers as molecular fossils: Problems and possible solutions, potential and limitations. In *E&G Quaternary Sci. J.* 58 (2), pp. 148–155. DOI: 10.3285/eg.58.2.03.

Zech, Michael; Krause, Tobias; Meszner, Sascha; Faust, Dominik (2013): Incorrect when uncorrected: Reconstructing vegetation history using n-alkane biomarkers in loess-paleosol sequences – A case study from the Saxonian loess region, Germany. In *Quaternary International* 296, pp. 108–116. DOI: 10.1016/j.quaint.2012.01.023.

Zheng, Yanhong; Zhou, Weijian; Meyers, Philip A.; Xie, Shucheng (2007): Lipid biomarkers in the Zoigê-Hongyuan peat deposit: Indicators of Holocene climate changes in West China. In *Organic Geochemistry* 38 (11), pp. 1927–1940. DOI: 10.1016/j.orggeochem.2007.06.012.

Zoltai, S. C.; Tarnocai, C. (1975): Perennially Frozen Peatlands in the Western Arctic and Subarctic of Canada. In *Can. J. Earth Sci.* 12 (1), pp. 28–43. DOI: 10.1139/e75-004.

Zona, D.; Oechel, W. C.; Peterson, K. M.; Clements, R. J.; Paw U, K. T.; Ustin, S. L. (2010): Characterization of the carbon fluxes of a vegetated drained lake basin chronosequence on the Alaskan Arctic Coastal Plain. In *Global Change Biology* 16 (6), pp. 1870–1882. DOI: 10.1111/j.1365-2486.2009.02107.x.

Zona, Donatella; Lipson, David A.; Paw U, Kyaw T.; Oberbauer, Steve F.; Olivas, Paulo;

# References

Gioli, Beniamino; Oechel, Walter C. (2012): Increased CO 2 loss from vegetated drained lake tundra ecosystems due to flooding. In *Global Biogeochemical Cycles* 26 (2), Article 2011GB004037. DOI: 10.1029/2011gb004037.

# Appendix

*Table A. 1. Raw data of the sedimentology.*

| Prefix | mean depth [cm b.s.l.] | abs. ice/water content [wt %] | mean grain size [µm] | clay [vol %] | silt [vol %] | silt acc. [vol %] | sand [vol %] | sand acc. [vol %] | sediment name |
|---|---|---|---|---|---|---|---|---|---|
| BAL24-T0-UL-A_0-8 | 4 | 87.98498 | *NA* | *NA* | *NA* | *NA* | *NA* | *NA* | *NA* |
| BAL24-T0-UL-A_8-20 | 14 | 89.78495 | *NA* | *NA* | *NA* | *NA* | *NA* | *NA* | *NA* |
| BAL24-T0-UL-A_20-22 | 21 | 76.92308 | *NA* | *NA* | *NA* | *NA* | *NA* | *NA* | *NA* |
| BAL24-T0-UL-A_22-32 | 27 | 73.33916 | *NA* | *NA* | *NA* | *NA* | *NA* | *NA* | *NA* |
| BAL24-T0-UL-A_32-37 | 34.5 | 31.6726 | 22.23978 | 4.089086 | 81.76628 | 85.85537 | 14.14463 | 100 | Coarse Silt |
| BAL24-T0-UL-A_37-42 | 39.5 | 26.95716 | *NA* | *NA* | *NA* | *NA* | *NA* | *NA* | *NA* |
| BAL24-T0-UL-A_42-47 | 44.5 | 27.06983 | 23.05513 | 3.917614 | 80.42891 | 84.34652 | 15.65348 | 100 | Coarse Silt |
| BAL24-T0-UL-A_47-52 | 49.5 | 34.94898 | 21.94023 | 4.035608 | 82.07108 | 86.10669 | 13.89331 | 100 | Coarse Silt |
| BAL24-T0-UL-A_52-57 | 54.5 | 57.46888 | 21.2729 | 4.755816 | 80.22266 | 84.97848 | 15.02152 | 100 | Coarse Silt |
| BAL24-T0-UL-A_57-61 | 59 | 58.28066 | *NA* | *NA* | *NA* | *NA* | *NA* | *NA* | *NA* |
| BAL24-T0-UL-A_61-63 | 62 | 46.72897 | 22.77758 | 4.486238 | 76.98021 | 81.46644 | 18.53356 | 100 | Coarse Silt |
| BAL24-T0-UL-A_63-73 | 68 | 34.35074 | *NA* | *NA* | *NA* | *NA* | *NA* | *NA* | *NA* |
| BAL24-T0-UL-A_73-77 | 75 | 51.46871 | 20.23842 | 5.765892 | 77.23882 | 83.00471 | 16.99529 | 100 | Coarse Silt |
| BAL24-T0-UL-A_77-81 | 79 | 54.61957 | 22.61986 | 5.055724 | 75.24725 | 80.30298 | 19.69702 | 100 | Coarse Silt |
| BAL24-T0-UL-A_81-85 | 83 | 52.80899 | 20.40054 | 5.462279 | 77.84958 | 83.31185 | 16.68815 | 100 | Coarse Silt |
| BAL24-T0-UL-A_85-90 | 87.5 | 48.14815 | 22.09123 | 4.474893 | 75.67899 | 80.15389 | 19.84611 | 100 | Coarse Silt |
| BAL24-T0-UL-A_90-95 | 92.5 | 44.30479 | 21.05137 | 4.78027 | 76.4869 | 81.26717 | 18.73283 | 100 | Coarse Silt |
| BAL24-T0-UL-A_95-100 | 97.5 | 39.42857 | 21.29187 | 4.637566 | 76.51104 | 81.14861 | 18.85139 | 100 | Coarse Silt |
| BAL24-T0-UL-A_100-103 | 101.5 | 37.3494 | 21.17054 | 4.529681 | 81.94168 | 86.47136 | 13.52864 | 100 | Coarse Silt |
| BAL24-T0-UL-A_103-108 | 105.5 | 45.31371 | 21.27447 | 4.780184 | 81.88589 | 86.66607 | 13.05538 | 99.72145 | Coarse Silt |
| BAL24-T0-UL-A_108-116 | 112 | 44.76285 | 26.38969 | 3.936395 | 74.35164 | 78.28803 | 21.71197 | 100 | Coarse Silt |
| BAL24-T0-UL-A_116-121 | 118.5 | 44.44444 | 23.7659 | 4.537456 | 78.22674 | 82.7642 | 17.2358 | 100 | Coarse Silt |
| BAL24-T0-UL-A_121-123 | 122 | 86.54354 | 25.64531 | 4.182551 | 77.06504 | 81.24759 | 18.75241 | 100 | Coarse Silt |
| BAL24-T0-UL-A_123-133 | 128 | 99.9181 | *NA* | *NA* | *NA* | *NA* | *NA* | *NA* | *NA* |
| BAL24-T0-UL-A_133-142 | 137.5 | 99.70646 | *NA* | *NA* | *NA* | *NA* | *NA* | *NA* | *NA* |
| BAL24-T0-UL-A_142-150 | 146 | 66.66667 | *NA* | *NA* | *NA* | *NA* | *NA* | *NA* | *NA* |
| BAL24-T0-UL-A_142-150 | 146 | 61.22449 | 23.24753 | 5.048397 | 77.01765 | 82.06605 | 17.93395 | 100 | Coarse Silt |
| BAL24-T0-UL-A_150-155 | 152.5 | 55.24718 | 22.84674 | 4.403946 | 78.42086 | 82.82481 | 17.17519 | 100 | Coarse Silt |
| BAL24-T0-UL-A_155-160 | 157.5 | 54.03304 | 22.68115 | 4.262241 | 80.12783 | 84.39007 | 15.60993 | 100 | Coarse Silt |
| BAL24-T0-UL-A_160-164 | 162 | 53.90625 | 22.53607 | 5.007396 | 78.81736 | 83.82475 | 16.17525 | 100 | Coarse Silt |
| BAL24-T0-UL-A_164-169 | 166.5 | 53.46535 | 21.29005 | 5.003849 | 77.89177 | 82.89562 | 17.10438 | 100 | Coarse Silt |
| BAL24-T0-UL-A_169-175 | 172 | 56.18221 | 22.2587 | 4.800364 | 78.95244 | 83.7528 | 16.2472 | 100 | Coarse Silt |
| BAL24-T0-UL-A_175-180 | 177.5 | 53.52941 | 24.039 | 3.795608 | 78.52672 | 82.32233 | 17.67767 | 100 | Coarse Silt |
| BAL24-T0-UL-A_180-186 | 183 | 53.81264 | 21.85677 | 5.117247 | 78.31672 | 83.43396 | 16.56604 | 100 | Coarse Silt |
| BAL24-T0-UL-A_186-196 | 191 | 56.05139 | *NA* | *NA* | *NA* | *NA* | *NA* | *NA* | *NA* |
| BAL24-T0-UL-A_196-202 | 199 | 59.53488 | 19.75375 | 4.782722 | 79.95398 | 84.7367 | 15.2633 | 100 | Coarse Silt |
| BAL24-T0-UL-A_196-202 | 199 | 59.53488 | *NA* | *NA* | *NA* | *NA* | *NA* | *NA* | *NA* |
| BAL24-T0-UL-A_202-207 | 204.5 | 65.32438 | 18.22156 | 5.536457 | 82.27574 | 87.81219 | 12.18781 | 100 | Coarse Silt |
| BAL24-T0-UL-A_207-213 | 210 | 65.82827 | 21.00709 | 4.97112 | 78.4298 | 83.40092 | 16.59908 | 100 | Coarse Silt |
| BAL24-T0-L-A-VIRBA_1-11 | 6 | 37.4695 | *NA* | *NA* | *NA* | *NA* | *NA* | *NA* | *NA* |
| BAL24-T0-L-A-VIRBA_1-11 | 6 | 43.29268 | 18.27359 | 5.375367 | 83.24763 | 88.62299 | 11.377008 | 100 | Coarse Silt |
| BAL24-T0-L-A-VIRBA_11-16 | 13.5 | 30.79268 | 19.77444 | 5.022346 | 80.87861 | 85.90096 | 14.099042 | 100 | Coarse Silt |
| BAL24-T0-L-A-VIRBA_16-21 | 18.5 | *NA* | 21.70398 | 4.367397 | 81.42866 | 85.79606 | 14.203944 | 100 | Coarse Silt |
| BAL24-T0-L-A-VIRBA_21-26 | 23.5 | 39.05085 | 21.12154 | 4.703476 | 81.23996 | 85.94343 | 14.056566 | 100 | Coarse Silt |
| BAL24-T0-L-A-VIRBA_26-30 | 28 | *NA* | 17.41997 | 5.468147 | 81.81921 | 87.28735 | 12.712645 | 100 | Coarse Silt |

| Prefix | mean depth [cm b.s.l.] | abs. ice/water content [wt %] | mean grain size [µm] | clay [vol %] | silt [vol %] | silt acc. [vol %] | sand [vol %] | sand acc. [vol %] | sediment name |
|---|---|---|---|---|---|---|---|---|---|
| BAL24-T0-L-A-VIRBA_30-34 | 32 | 65.48673 | *NA* | *NA* | *NA* | *NA* | *NA* | *NA* | *NA* |
| BAL24-T0-L-A-VIRBA_34-37 | 35.5 | 64.94253 | 15.57885 | 5.40229 | 83.69458 | 89.09687 | 10.903129 | 100 | Medium Silt |
| BAL24-T0-L-A-VIRBA_37-42 | 39.5 | 67.48286 | *NA* | *NA* | *NA* | *NA* | *NA* | *NA* | *NA* |
| BAL24-T0-L-A-VIRBA_42-47 | 44.5 | *NA* | 16.31473 | 5.412329 | 83.26187 | 88.6742 | 11.325799 | 100 | Coarse Silt |
| BAL24-T0-L-A-VIRBA_47-52 | 49.5 | 56.91188 | *NA* | *NA* | *NA* | *NA* | *NA* | *NA* | *NA* |
| BAL24-T0-L-A-VIRBA_52-57 | 54.5 | *NA* | 14.92544 | 5.736715 | 83.13001 | 88.86672 | 11.133277 | 100 | Medium Silt |
| BAL24-T0-L-A-VIRBA_57-62 | 59.5 | 60.34913 | *NA* | *NA* | *NA* | *NA* | *NA* | *NA* | *NA* |
| BAL24-T0-L-A-VIRBA_62-67 | 64.5 | *NA* | 15.37606 | 5.588694 | 82.33388 | 87.92257 | 12.053578 | 99.97615 | Medium Silt |
| BAL24-T0-L-A-VIRBA_67-72 | 69.5 | 66.72444 | *NA* | *NA* | *NA* | *NA* | *NA* | *NA* | *NA* |
| BAL24-T0-L-A-VIRBA_72-77 | 74.5 | *NA* | 15.77927 | 5.69667 | 82.00961 | 87.70628 | 12.293724 | 100 | Coarse Silt |
| BAL24-T0-L-A-VIRBA_77-82 | 79.5 | 55.91739 | *NA* | *NA* | *NA* | *NA* | *NA* | *NA* | *NA* |
| BAL24-T0-L-A-VIRBA_82-87 | 84.5 | *NA* | 15.69652 | 4.902507 | 87.47016 | 92.37267 | 7.627333 | 100 | Coarse Silt |
| BAL24-T0-L-A-VIRBA_87-91 | 89 | 46.68459 | 12.53332 | 6.206144 | 86.5607 | 92.76684 | 7.233158 | 100 | Medium Silt |
| BAL24-T0-L-A-VIRBA_91-96 | 93.5 | 45.3411 | *NA* | *NA* | *NA* | *NA* | *NA* | *NA* | *NA* |
| BAL24-T0-L-A-VIRBA_96-98 | 97 | 43.27323 | 11.68426 | 6.635934 | 88.24236 | 94.8783 | 5.121703 | 100 | Medium Silt |
| BAL24-T0-L-A-VIRBA_98-103 | 100.5 | *NA* | 11.63914 | 9.286964 | 84.41295 | 93.69991 | 6.300088 | 100 | Medium Silt |
| BAL24-T0-L-A-VIRBA_103-108 | 105.5 | 46.81159 | 11.71753 | 7.424536 | 87.59867 | 95.02321 | 4.976794 | 100 | Medium Silt |
| BAL24-T0-L-A-VIRBA_108-113 | 110.5 | *NA* | 10.43236 | 9.001512 | 86.692 | 95.69351 | 4.306489 | 100 | Medium Silt |
| BAL24-T0-L-A-VIRBA_113-118 | 115.5 | 45.60944 | 13.27685 | 6.217235 | 85.98821 | 92.20545 | 7.794551 | 100 | Medium Silt |
| BAL24-T0-L-A-VIRBA_118-123 | 120.5 | *NA* | 14.98052 | 5.540079 | 88.11079 | 93.65087 | 6.349128 | 100 | Medium Silt |
| BAL24-T0-L-A-VIRBA_123-127 | 125 | 40.92284 | 14.41094 | 6.416653 | 86.42231 | 92.83896 | 7.161038 | 100 | Medium Silt |
| BAL24-T0-L-A-VIRBA_127-137 | 132 | 57.89099 | *NA* | *NA* | *NA* | *NA* | *NA* | *NA* | *NA* |
| BAL24-T0-L-A-VIRBA_137-140 | 138.5 | 56.83453 | 17.73079 | 4.864729 | 81.30296 | 86.16769 | 13.83231 | 100 | Coarse Silt |
| BAL24-T0-L-A-VIRBA_140-145 | 142.5 | 25.96917 | 20.87463 | 4.356131 | 82.56001 | 86.91614 | 13.08386 | 100 | Coarse Silt |
| BAL24-T0-L-A-VIRBA_145-150 | 147.5 | 24.32821 | 20.13235 | 4.222679 | 83.72266 | 87.94534 | 12.054657 | 100 | Coarse Silt |
| BAL24-T0-L-A-VIRBA_150-155 | 152.5 | 28.81699 | 21.71619 | 4.140065 | 81.78362 | 85.92368 | 14.076316 | 100 | Coarse Silt |
| BAL24-T0-L-A-VIRBA_155-160 | 157.5 | 26.6858 | 22.25695 | 4.998728 | 78.97986 | 83.97859 | 16.02141 | 100 | Coarse Silt |
| BAL24-T0-L-A-VIRBA_160-165 | 162.5 | 26.21359 | 20.93211 | 4.278689 | 82.5855 | 86.86419 | 13.135813 | 100 | Coarse Silt |
| BAL24-T0-L-A-VIRBA_165-170 | 167.5 | 24.62936 | 20.16208 | 4.887149 | 82.83529 | 87.72243 | 12.277565 | 100 | Coarse Silt |
| BAL24-T0-L-A-VIRBA_170-175 | 172.5 | 25.83222 | 20.50829 | 4.544479 | 82.14039 | 86.68487 | 13.31513 | 100 | Coarse Silt |
| BAL24-T0-L-A-VIRBA_175-181 | 178 | 24.86441 | 22.45998 | 4.370409 | 81.31374 | 85.68414 | 14.315855 | 100 | Coarse Silt |
| BAL24-T0-L-A-VIRBA_181-187 | 184 | 24.7451 | 20.32145 | 4.307433 | 82.72753 | 87.03496 | 12.965039 | 100 | Coarse Silt |
| BAL24-T0-L-A-VIRBA_187-193 | 190 | 24.50903 | 20.32145 | 4.307433 | 82.72753 | 87.03496 | 12.965039 | 100 | Coarse Silt |
| BAL24-T0-L-A-VIRBA_193-198 | 195.5 | 24.81442 | *NA* | *NA* | *NA* | *NA* | *NA* | *NA* | *NA* |
| BAL24-T0-L-A-VIRBA_198-201 | 199.5 | 25.29412 | 20.8681 | 4.449169 | 82.16566 | 86.61483 | 13.385167 | 100 | Coarse Silt |
| BAL24-T0-L-A-VIRBA_201-206 | 203.5 | 26.40227 | 20.59522 | 4.324413 | 82.14642 | 86.47083 | 13.529168 | 100 | Coarse Silt |
| BAL24-T0-L-A-VIRBA_206-211 | 208.5 | 26.86671 | 24.6684 | 3.261335 | 80.54684 | 83.80818 | 16.191825 | 100 | Coarse Silt |
| BAL24-T0-L-A-VIRBA_211-216 | 213.5 | 29.0152 | 22.6263 | 4.128251 | 80.62312 | 84.75137 | 15.248625 | 100 | Coarse Silt |
| BAL24-T0-L-A-VIRBA_216-221 | 218.5 | 27.53807 | 21.75626 | 4.019066 | 82.25556 | 86.27463 | 13.72537 | 100 | Coarse Silt |
| BAL24-T0-L-A-VIRBA_221-226 | 223.5 | 28.00241 | 23.21871 | 4.0752 | 80.53469 | 84.60989 | 15.390106 | 100 | Coarse Silt |
| BAL24-T0-L-A-VIRBA_226-231 | 228.5 | 29.8278 | 23.62217 | 4.726057 | 78.25681 | 82.98287 | 17.017129 | 100 | Coarse Silt |
| BAL24-T0-L-A-VIRBA_231-241 | 236 | 24.8059 | *NA* | *NA* | *NA* | *NA* | *NA* | *NA* | *NA* |
| BAL24-T0-L-A-VIRBA_241-244 | 242.5 | 25.93718 | 28.85455 | 3.306867 | 74.42857 | 77.73544 | 22.264558 | 100 | Coarse Silt |
| BAL24-T0-L-A-VIRBA_244-249 | 246.5 | 28.6399 | 28.95546 | 3.578458 | 72.40045 | 75.97891 | 24.021092 | 100 | Coarse Silt |
| BAL24-T0-L-A-VIRBA_249-254 | 251.5 | 28.35561 | 36.49246 | 2.264748 | 71.76101 | 74.02576 | 25.97424 | 100 | Very Coarse Silt |
| BAL24-T0-L-A-VIRBA_254-259 | 256.5 | 28 | 37.63426 | 2.861683 | 64.52693 | 67.38861 | 32.611391 | 100 | Very Coarse Silt |

# Appendix

| Prefix | mean depth [cm b.s.l.] | abs. ice/water content [wt %] | mean grain size [µm] | clay [vol %] | silt [vol %] | silt acc. [vol %] | sand [vol %] | sand acc. [vol %] | sediment name |
|---|---|---|---|---|---|---|---|---|---|
| BAL24-T0-L-A-VIRBA_259-264 | 261.5 | 28.11989 | 35.14786 | 3.090284 | 65.30714 | 68.39743 | 31.602575 | 100 | Very Coarse Silt |
| BAL24-T0-L-A-VIRBA_264-269 | 266.5 | 26.67423 | 44.54215 | 2.343448 | 57.02873 | 59.37218 | 40.627818 | 100 | Very Coarse Silt |
| BAL24-T0-L-A-VIRBA_269-274 | 271.5 | 24.26266 | 61.16878 | 1.604184 | 47.10108 | 48.70526 | 51.294738 | 100 | Very Coarse Silt |
| BAL24-T0-L-A-VIRBA_274-279 | 276.5 | 26.65535 | 29.95883 | 3.783835 | 69.92848 | 73.71232 | 26.287684 | 100 | Coarse Silt |
| BAL24-T0-L-A-VIRBA_279-285 | 282 | 26.18718 | 39.94387 | 2.785307 | 63.90733 | 66.69263 | 33.307365 | 100 | Very Coarse Silt |
| BAL24-T0-L-A-VIRBA_285-291 | 288 | 25.50562 | 34.28687 | 2.927489 | 68.06095 | 70.98844 | 29.011562 | 100 | Very Coarse Silt |
| BAL24-T0-L-A-VIRBA_291-297 | 294 | 22.29299 | 38.04889 | 2.470771 | 63.62063 | 66.0914 | 33.908596 | 100 | Very Coarse Silt |
| BAL24-T0-L-A-VIRBA_297-307 | 302 | 26.51347 | *NA* | *NA* | *NA* | *NA* | *NA* | *NA* | *NA* |
| BAL24-T0-L-A-VIRBA_307-311 | 309 | 35.44715 | 30.57104 | 3.129967 | 74.38845 | 77.51841 | 22.481587 | 100 | Coarse Silt |
| BAL24-T0-DLB-A_0-1 | 0.5 | 72.31405 | NA | NA | NA | NA | NA | NA | NA |
| BAL24-T0-DLB-A_1-11 | 6 | 57.8003 | NA | NA | NA | NA | NA | NA | NA |
| BAL24-T0-DLB-A_11-13 | 12 | 46.94737 | 20.04775 | 4.948802 | 82.00391 | 86.95271 | 13.04729 | 100 | Coarse Silt |
| BAL24-T0-DLB-A_13-19 | 16 | 42.45333 | 22.20757 | 4.249615 | 78.86269 | 83.11231 | 16.88769 | 100 | Coarse Silt |
| BAL24-T0-DLB-A_19-23 | 21 | 38.70095 | 22.28019 | 4.980125 | 78.19979 | 83.17991 | 16.82009 | 100 | Coarse Silt |
| BAL24-T0-DLB-A_23-27 | 25 | 38.31169 | 26.60083 | 3.853828 | 76.62118 | 80.47501 | 19.52499 | 100 | Coarse Silt |
| BAL24-T0-DLB-A_27-32 | 29.5 | 33.78747 | 23.94192 | 4.293517 | 78.80491 | 83.09842 | 16.90158 | 100 | Coarse Silt |
| BAL24-T0-DLB-A_32-38 | 35 | 35.84432 | 24.98128 | 4.149495 | 78.10177 | 82.25126 | 17.74874 | 100 | Coarse Silt |
| BAL24-T0-DLB-A_38-42 | 40 | 36.16037 | 25.50787 | 4.122558 | 78.59216 | 82.71472 | 17.28528 | 100 | Coarse Silt |
| BAL24-T0-DLB-A_42-46 | 44 | 34.12395 | 27.41325 | 3.421792 | 77.67638 | 81.09817 | 18.90183 | 100 | Coarse Silt |
| BAL24-T0-DLB-A_46-51 | 48.5 | 33.79265 | 28.21096 | 3.752363 | 76.05842 | 79.81079 | 20.18921 | 100 | Coarse Silt |
| BAL24-T0-DLB-A_51-56 | 53.5 | 34.68635 | NA | NA | NA | NA | NA | NA | NA |
| BAL24-T0-DLB-A_56-58 | 57 | 33.00589 | 23.4947 | 4.042978 | 81.11152 | 85.1545 | 14.8455 | 100 | Coarse Silt |
| BAL24-T0-DLB-A_58-65 | 61.5 | 34.30762 | 24.71895 | 4.104203 | 79.02736 | 83.13156 | 16.86844 | 100 | Coarse Silt |
| BAL24-T0-DLB-A_65-69 | 67 | 35.76642 | 22.77109 | 4.318298 | 79.96863 | 84.28693 | 15.71307 | 100 | Coarse Silt |
| BAL24-T0-DLB-A_69-73 | 71 | 34.95146 | 23.53615 | 4.163384 | 78.90748 | 83.07087 | 16.92913 | 100 | Coarse Silt |
| BAL24-T0-DLB-A_73-78 | 75.5 | 37.63626 | 21.43625 | 4.481403 | 81.22553 | 85.70693 | 14.29307 | 100 | Coarse Silt |
| BAL24-T0-DLB-A_78-84 | 81 | NA | 26.46283 | 3.450107 | 78.44084 | 81.89095 | 18.10905 | 100 | Coarse Silt |
| BAL24-T0-DLB-A_84-90 | 87 | 33.21779 | 22.96875 | 4.211709 | 81.54565 | 85.75736 | 14.24264 | 100 | Coarse Silt |
| BAL24-T0-DLB-A_90-96 | 93 | NA | 18.78735 | 6.069748 | 78.98664 | 85.05638 | 14.94362 | 100 | Coarse Silt |
| BAL24-T0-DLB-A_96-106 | 101 | 34.36727 | NA | NA | NA | NA | NA | NA | NA |
| BAL24-T0-DLB-A_106-108 | 107 | 31.57895 | 28.08025 | 3.455184 | 76.67582 | 80.13101 | 19.86899 | 100 | Coarse Silt |
| BAL24-T0-DLB-A_108-113 | 110.5 | 33.61823 | 25.18158 | 3.704584 | 78.04237 | 81.74696 | 18.25304 | 100 | Coarse Silt |
| BAL24-T0-DLB-A_113-118 | 115.5 | NA | 24.67469 | 4.139495 | 78.70271 | 82.8422 | 17.1578 | 100 | Coarse Silt |
| BAL24-T0-DLB-A_118-123 | 120.5 | 36.65615 | 23.02423 | 4.241721 | 80.2821 | 84.52382 | 15.47618 | 100 | Coarse Silt |
| BAL24-T0-DLB-A_123-128 | 125.5 | NA | 22.84029 | 4.112543 | 78.81923 | 82.93178 | 17.06822 | 100 | Coarse Silt |
| BAL24-T0-DLB-A_128-133 | 130.5 | 36.02151 | 25.71241 | 3.794521 | 76.31761 | 80.11213 | 19.88787 | 100 | Coarse Silt |
| BAL24-T0-DLB-A_133-137 | 135 | NA | 27.17673 | 3.675412 | 75.53228 | 79.20769 | 20.79231 | 100 | Coarse Silt |
| BAL24-T0-DLB-A_137-142 | 139.5 | 30.55787 | 26.40352 | 3.94648 | 75.09022 | 79.0367 | 20.9633 | 100 | Coarse Silt |
| BAL24-T0-DLB-A_142-147 | 144.5 | NA | 31.78688 | 2.527226 | 75.6693 | 78.19652 | 21.80348 | 100 | Very Coarse Silt |
| BAL24-T0-DLB-A_147-152 | 149.5 | 32.45455 | NA | NA | NA | NA | NA | NA | NA |
| BAL24-T0-DLB-A_152-154 | 153 | 31.33641 | 30.57534 | 3.060812 | 72.77409 | 75.8349 | 24.1651 | 100 | Coarse Silt |
| BAL24-T0-DLB-A_154-159 | 156.5 | NA | 26.91889 | 3.608571 | 76.0787 | 79.68727 | 20.31273 | 100 | Coarse Silt |
| BAL24-T0-DLB-A_159-164 | 161.5 | 28.20676 | 29.61542 | 3.04112 | 74.82129 | 77.86241 | 22.13759 | 100 | Coarse Silt |
| BAL24-T0-DLB-A_164-169 | 166.5 | NA | 32.36259 | 2.480526 | 72.7557 | 75.23623 | 24.76377 | 100 | Very Coarse Silt |
| BAL24-T0-DLB-A_169-174 | 171.5 | 30.8084 | 30.12251 | 3.402629 | 74.01819 | 77.42082 | 22.57918 | 100 | Coarse Silt |
| BAL24-T0-DLB-A_174-179 | 176.5 | NA | 30.71379 | 2.699199 | 74.88156 | 77.58075 | 22.41925 | 100 | Coarse Silt |

# Appendix

| Prefix | mean depth [cm b.s.l.] | abs. ice/water content [wt %] | mean grain size [µm] | clay [vol %] | silt [vol %] | silt acc. [vol %] | sand [vol %] | sand acc. [vol %] | sediment name |
|---|---|---|---|---|---|---|---|---|---|
| BAL24-T0-DLB-A_179-184 | 181.5 | 29.29178 | 26.58622 | 3.29042 | 78.54995 | 81.84037 | 18.15963 | 100 | Coarse Silt |
| BAL24-T0-DLB-A_184-189 | 186.5 | NA | 30.55884 | 2.825594 | 74.84361 | 77.6692 | 22.3308 | 100 | Coarse Silt |
| BAL24-T0-DLB-A_189-194 | 191.5 | 28.51109 | 32.1898 | 2.608155 | 72.01442 | 74.62257 | 25.37743 | 100 | Very Coarse Silt |
| BAL24-T0-DLB-A_194-199 | 196.5 | NA | 31.00712 | 2.668665 | 73.62478 | 76.29344 | 23.70656 | 100 | Coarse Silt |
| BAL24-T0-DLB-A_199-209 | 204 | 27.59014 | NA | NA | NA | NA | NA | NA | NA |
| BAL24-T0-DLB-A_209-214 | 211.5 | 28.12331 | 28.26309 | 3.034177 | 76.80953 | 79.84371 | 20.15629 | 100 | Coarse Silt |
| BAL24-T0-M1-PUSH_0-5 | 2.5 | 47.55102 | 29.51701 | 2.987537 | 75.23651 | 78.22404 | 21.77596 | 100 | Coarse Silt |
| BAL24-T0-M1-PUSH_5-10 | 7.5 | 44.18819 | NA | NA | NA | NA | NA | NA | NA |
| BAL24-T0-M1-PUSH_10-13 | 11.5 | 39.97628 | NA | NA | NA | NA | NA | NA | NA |
| BAL24-T0-M1-PUSH_13-18 | 15.5 | 39.41134 | 22.5091 | 3.966835 | 81.16358 | 85.13041 | 14.86959 | 100 | Coarse Silt |
| BAL24-T0-M1-PUSH_18-23 | 20.5 | 38.90034 | 33.48276 | 2.698098 | 71.84072 | 74.53882 | 25.46118 | 100 | Very Coarse Silt |
| BAL24-T0-M1-PUSH_23-28 | 25.5 | 32.87995 | NA | NA | NA | NA | NA | NA | NA |
| BAL24-T0-M1-PUSH_28-33 | 30.5 | 31.84524 | 32.62821 | 2.585367 | 75.23277 | 77.81814 | 22.18186 | 100 | Very Coarse Silt |
| BAL24-T0-M1-PUSH_33-38 | 35.5 | 30.36903 | 33.52656 | 3.348088 | 70.3949 | 73.74299 | 26.25701 | 100 | Very Coarse Silt |
| BAL24-T0-M1-PUSH_38-42 | 40 | 30.75299 | 29.29419 | 2.855051 | 76.52568 | 79.38073 | 20.61927 | 100 | Coarse Silt |
| BAL24-T0-M1-PUSH_42-47 | 44.5 | 27.57808 | NA | NA | NA | NA | NA | NA | NA |
| BAL24-T0-M1-PUSH_47-52 | 49.5 | 24.10667 | 39.61364 | 2.685043 | 61.18244 | 63.86748 | 36.13252 | 100 | Very Coarse Silt |
| BAL24-T0-M1-PUSH_52-55 | 53.5 | 25.36294 | 36.10735 | 2.921177 | 64.51046 | 67.43163 | 32.56837 | 100 | Very Coarse Silt |

*Table A. 2.Raw data of the hydrochemistry.*

| Prefix | mean depth [cm b.s.l.] | DOC [mg $L^{-1}$] | mean $\delta^{18}O$ [‰ vs. SMOW] | mean δD [‰ vs. SMOW] | mean d excess [-] | EC [µS $cm^{-1}$] | pH [-] |
|---|---|---|---|---|---|---|---|
| BAL24-T0-UL-A_8-20 | 14 | 42.05 | -15.08081 | -112.2792 | 8.367266 | 44.62 | 4.87 |
| BAL24-T0-UL-A_42-47 | 44.5 | 33.075 | -16.16772 | -118.5781 | 10.763627 | 49.51 | 6.3 |
| BAL24-T0-UL-A_52-57 | 54.5 | 40.31 | -16.35906 | -120.9678 | 9.904634 | 88.08 | 6.36 |
| BAL24-T0-UL-A_73-77 | 75 | 223.3 | -16.8575 | -128.0053 | 6.854633 | 48.89 | 6.03 |
| BAL24-T0-UL-A_81-85 | 83 | 131.4 | -16.61907 | -128.2484 | 4.704199 | 156.2 | 6.74 |
| BAL24-T0-UL-A_90-95 | 92.5 | 159.1 | *NA* | *NA* | *NA* | 205.9 | 6.93 |
| BAL24-T0-UL-A_103-108 | 105.5 | 99.9 | -14.63003 | -120.0985 | -3.05824 | 256.2 | 7.08 |
| BAL24-T0-UL-A_116-121 | 118.5 | 199.8 | -15.49239 | -125.6627 | -1.723543 | 409.3 | 7.4 |
| BAL24-T0-UL-A_123-133 | 128 | 5.783 | -20.35954 | -160.2123 | 2.663984 | 43.41 | 7.17 |
| BAL24-T0-UL-A_133-142 | 137.5 | 9.155 | -19.83193 | -155.21 | 3.445384 | 73.22 | 7.43 |
| BAL24-T0-UL-A_150-155 | 152.5 | 857.6 | -19.64046 | -152.8184 | 4.305286 | 1405 | 6.97 |
| BAL24-T0-UL-A_160-164 | 162 | 1075 | -19.62421 | -152.7071 | 4.286592 | 1656 | 6.87 |
| BAL24-T0-UL-A_169-175 | 172 | 1342 | -19.72329 | -153.2688 | 4.517505 | 1998 | 6.54 |
| BAL24-T0-UL-A_180-186 | 183 | 1707 | -19.78382 | -151.8303 | 6.440239 | 2379 | 6.4 |
| BAL24-T0-UL-A_202-207 | 204.5 | 940 | -19.43193 | -150.6093 | 4.846156 | 1385 | 5.68 |
| BAL24-T0-L-A-VIRBA_16-21 | 18.5 | 113.8 | -17.03143 | -135.1828 | 1.06863598 | 589.4 | 7.81 |
| BAL24-T0-L-A-VIRBA_26-30 | 28 | 143.7 | -17.33175 | -138.9616 | -0.30764745 | 721.3 | 7.82 |
| BAL24-T0-L-A-VIRBA_42-47 | 44.5 | 142.9 | -17.70276 | -141.2318 | 0.39032678 | 91 | 7.73 |
| BAL24-T0-L-A-VIRBA_52-57 | 54.5 | 151.7 | *NA* | *NA* | *NA* | 695.6 | 7.92 |
| BAL24-T0-L-A-VIRBA_62-67 | 64.5 | 126.3 | *NA* | *NA* | *NA* | 575.7 | 7.66 |
| BAL24-T0-L-A-VIRBA_72-77 | 74.5 | 160.35 | -18.19971 | -146.1684 | -0.57065067 | 721.6 | 7.68 |
| BAL24-T0-L-A-VIRBA_82-87 | 84.5 | 130.55 | -18.41303 | -147.4176 | -0.11343559 | 618.8 | 7.74 |
| BAL24-T0-L-A-VIRBA_98-103 | 100.5 | 183.85 | -18.61363 | -149.3889 | -0.47986551 | 802.1 | 7.57 |
| BAL24-T0-L-A-VIRBA_108-113 | 110.5 | 188.95 | -18.71228 | -150.6735 | -0.97525971 | 862.6 | 7.76 |

| Prefix | mean depth [cm b.s.l.] | DOC [mg $L^{-1}$] | mean $\delta^{18}O$ [‰ vs. SMOW] | mean δD [‰ vs. SMOW] | mean d excess [-] | EC [µS $cm^{-1}$] | pH [-] |
|---|---|---|---|---|---|---|---|
| BAL24-T0-L-A-VIRBA_118-123 | 120.5 | 151.4 | -18.8376 | -151.3072 | -0.60640004 | 634 | 7.72 |
| BAL24-T0-L-A-VIRBA_140-145 | 142.5 | 121.5 | -18.93901 | -151.2825 | 0.22961042 | 569.8 | 7.28 |
| BAL24-T0-L-A-VIRBA_150-155 | 152.5 | 129.1 | -18.94678 | -151.2433 | 0.33095647 | 470.4 | 7.22 |
| BAL24-T0-L-A-VIRBA_160-165 | 162.5 | 124.65 | -18.90321 | -152.3942 | -1.16849969 | 471.4 | 7.73 |
| BAL24-T0-L-A-VIRBA_170-175 | 172.5 | 125.75 | -18.8772 | -152.0884 | -1.07083759 | 459.9 | 7.61 |
| BAL24-T0-L-A-VIRBA_201-206 | 203.5 | 136.7 | *NA* | *NA* | *NA* | 438.9 | 7.58 |
| BAL24-T0-L-A-VIRBA_211-216 | 213.5 | 153.7 | -18.62386 | -147.6998 | 1.29112189 | 520.3 | 8.09 |
| BAL24-T0-L-A-VIRBA_221-226 | 223.5 | 154.15 | -18.55659 | -148.9103 | -0.45764161 | 572.5 | 7.7 |
| BAL24-T0-L-A-VIRBA_244-249 | 246.5 | 213.5 | *NA* | *NA* | *NA* | 821.1 | 8.22 |
| BAL24-T0-L-A-VIRBA_254-259 | 256.5 | 195.7 | -17.98037 | -143.3454 | 0.49753938 | 783.3 | 7.88 |
| BAL24-T0-L-A-VIRBA_264-269 | 266.5 | 186.8 | -17.82924 | -142.6691 | -0.03516393 | 708 | 8.03 |
| BAL24-T0-L-A-VIRBA_274-279 | 276.5 | 204.95 | *NA* | *NA* | *NA* | 799.4 | 7.85 |
| BAL24-T0-L-A-VIRBA_285-291 | 288 | 177.75 | -17.52408 | -133.2424 | 6.95026549 | 784.3 | 7.8 |
| BAL24-T0-DLB-A_13-19 | 16 | 46.63 | -14.3174 | -112.1498 | 2.389364 | 771.9 | 7.69 |
| BAL24-T0-DLB-A_23-27 | 25 | 47.095 | -14.24584 | -112.6655 | 1.301212 | 853.3 | 8.03 |
| BAL24-T0-DLB-A_32-38 | 35 | 93.55 | -15.37501 | -121.0903 | 1.909739 | 980.8 | 7.9 |
| BAL24-T0-DLB-A_42-46 | 44 | 146.25 | -16.57504 | -130.5702 | 2.030058 | 899.4 | 7.8 |
| BAL24-T0-DLB-A_58-65 | 61.5 | 211.25 | -18.05706 | -139.5861 | 4.870412 | 958.8 | 7.62 |
| BAL24-T0-DLB-A_69-73 | 71 | 235.35 | -18.5347 | -142.6532 | 5.624325 | 850.7 | 7.88 |
| BAL24-T0-DLB-A_78-84 | 81 | 211.5 | -18.89099 | -143.8412 | 7.286734 | 887.7 | 7.97 |
| BAL24-T0-DLB-A_90-96 | 93 | 218.1 | -19.11008 | -145.2686 | 7.612041 | 987.9 | 7.76 |
| BAL24-T0-DLB-A_113-118 | 115.5 | 241.8 | *NA* | *NA* | *NA* | 1048 | 8.08 |
| BAL24-T0-DLB-A_123-128 | 125.5 | 255.25 | -19.56639 | -146.3475 | 10.183626 | 1071 | 8.01 |
| BAL24-T0-DLB-A_133-137 | 135 | 198.35 | *NA* | *NA* | *NA* | 733.9 | 7.95 |
| BAL24-T0-DLB-A_142-147 | 144.5 | 173.1 | *NA* | *NA* | *NA* | 742.9 | 7.99 |
| BAL24-T0-DLB-A_154-159 | 156.5 | 179.1 | -18.93635 | -142.6799 | 8.810921 | 815.3 | 7.96 |
| BAL24-T0-DLB-A_164-169 | 166.5 | 232.2 | *NA* | *NA* | *NA* | 961.4 | 8.41 |
| BAL24-T0-DLB-A_174-179 | 176.5 | 217.6 | -19.53497 | -141.6816 | 14.598104 | 944.4 | 8.05 |
| BAL24-T0-DLB-A_184-189 | 186.5 | 197.45 | -19.24295 | -143.8099 | 10.133716 | 923.7 | 8 |
| BAL24-T0-DLB-A_194-199 | 196.5 | 312.25 | *NA* | *NA* | *NA* | 1029 | 8.17 |
| BAL24-T0-M1-PUSH_13-18 | 15.5 | 66.71 | -13.28085 | -102.5079 | 3.738853 | 17290 | 7.47 |
| BAL24-T0-M1-PUSH_33-38 | 35.5 | 45.18 | -13.41767 | -102.2469 | 5.094446 | 19380 | 7.99 |
| BAL24-T0-M1-PUSH_47-52 | 49.5 | 41.375 | -13.14296 | -101.5741 | 3.569637 | 20390 | 7.83 |

*Table A. 3.Raw data of the biogeochemistry.*

| Prefix | mean depth [cm b.s.l.] | TOC [wt %] | TN [wt %] | C/N [-] | $\delta^{13}C$ [‰ vs. VPDB] |
|---|---|---|---|---|---|
| BAL24-T0-UL-A_0-8 | 4 | 42.404752 | 1.197 | 35.42586 | -29.75592 |
| BAL24-T0-UL-A_8-20 | 14 | 44.415247 | 1.057 | 42.0201 | -28.32276 |
| BAL24-T0-UL-A_20-22 | 21 | 37.199883 | 2.0145 | 18.46606 | -27.29474 |
| BAL24-T0-UL-A_22-32 | 27 | 32.420201 | 1.8705 | 17.33237 | *NA* |
| BAL24-T0-UL-A_32-37 | 34.5 | 2.133366 | 0.17 | 12.54921 | -27.93374 |
| BAL24-T0-UL-A_37-42 | 39.5 | 1.848613 | 0.1115 | 16.57949 | *NA* |
| BAL24-T0-UL-A_42-47 | 44.5 | 1.955831 | 0.121 | 16.16389 | -27.61642 |
| BAL24-T0-UL-A_47-52 | 49.5 | 2.645075 | 0.1765 | 14.98626 | -27.34555 |
| BAL24-T0-UL-A_52-57 | 54.5 | 5.392463 | 0.3615 | 14.91691 | -27.06595 |
| BAL24-T0-UL-A_57-61 | 59 | 16.284694 | 0.8155 | 19.96897 | -27.17738 |

# Appendix

| Prefix | mean depth [cm b.s.l.] | TOC [wt %] | TN [wt %] | C/N [-] | $\delta^{13}C$ [‰ vs. VPDB] |
|---|---|---|---|---|---|
| BAL24-T0-UL-A_61-63 | 62 | 4.388157 | 0.322 | 13.62782 | -26.48602 |
| BAL24-T0-UL-A_63-73 | 68 | 3.51261 | 0.311 | 11.29457 | *NA* |
| BAL24-T0-UL-A_73-77 | 75 | 4.431164 | 0.3615 | 12.25772 | -26.18605 |
| BAL24-T0-UL-A_77-81 | 79 | 4.421886 | 0.389 | 11.36732 | -26.05933 |
| BAL24-T0-UL-A_81-85 | 83 | 4.141357 | 0.355 | 11.66579 | -26.0627 |
| BAL24-T0-UL-A_85-90 | 87.5 | 4.875413 | 0.397 | 12.28064 | -26.29928 |
| BAL24-T0-UL-A_90-95 | 92.5 | 4.214175 | 0.3535 | 11.92129 | -26.11445 |
| BAL24-T0-UL-A_95-100 | 97.5 | 4.368179 | 0.3815 | 11.45001 | -26.31385 |
| BAL24-T0-UL-A_100-103 | 101.5 | 4.334399 | 0.3715 | 11.66729 | -25.97824 |
| BAL24-T0-UL-A_103-108 | 105.5 | 3.693207 | 0.324 | 11.39879 | -25.81215 |
| BAL24-T0-UL-A_108-116 | 112 | 3.457644 | 0.3125 | 11.06446 | -26.08825 |
| BAL24-T0-UL-A_116-121 | 118.5 | 3.904331 | 0.3275 | 11.92162 | -26.04694 |
| BAL24-T0-UL-A_121-123 | 122 | 2.836034 | 0.275 | 10.31285 | -25.88572 |
| BAL24-T0-UL-A_123-133 | 128 | 3.544638 | 0.391 | 9.06557 | *NA* |
| BAL24-T0-UL-A_133-142 | 137.5 | 2.742171 | 0.243 | 11.28465 | *NA* |
| BAL24-T0-UL-A_142-150 | 146 | 4.38217 | 0.34 | 12.88873 | *NA* |
| BAL24-T0-UL-A_142-150 | 146 | 5.162768 | 0.4065 | 12.70054 | -26.3262 |
| BAL24-T0-UL-A_150-155 | 152.5 | 4.750294 | 0.3865 | 12.29054 | -26.37964 |
| BAL24-T0-UL-A_155-160 | 157.5 | 5.703895 | 0.469 | 12.16182 | -26.18455 |
| BAL24-T0-UL-A_160-164 | 162 | 4.752249 | 0.4035 | 11.77757 | -26.23169 |
| BAL24-T0-UL-A_164-169 | 166.5 | 5.142456 | 0.449 | 11.45313 | -26.28077 |
| BAL24-T0-UL-A_169-175 | 172 | 5.98625 | 0.458 | 13.07041 | -26.2642 |
| BAL24-T0-UL-A_175-180 | 177.5 | 6.186264 | 0.515 | 12.01216 | -26.17713 |
| BAL24-T0-UL-A_180-186 | 183 | 6.86349 | 0.5555 | 12.35552 | -26.28104 |
| BAL24-T0-UL-A_186-196 | 191 | 8.0954 | 0.5455 | 14.84033 | -26.11563 |
| BAL24-T0-UL-A_196-202 | 199 | 6.464248 | 0.5515 | 11.72121 | -26.29726 |
| BAL24-T0-UL-A_196-202 | 199 | 8.059861 | 0.531 | 15.17865 | -26.29726 |
| BAL24-T0-UL-A_202-207 | 204.5 | 5.015068 | 0.436 | 11.50245 | -26.01277 |
| BAL24-T0-UL-A_207-213 | 210 | 6.078353 | 0.5015 | 12.12034 | -26.21934 |
| BAL24-T0-L-A-VIRBA_1-11 | 6 | 4.3978818 | 0.3635 | 12.098712 | -25.9575 |
| BAL24-T0-L-A-VIRBA_1-11 | 6 | 4.1149664 | 0.3915 | 10.51077 | -25.9575 |
| BAL24-T0-L-A-VIRBA_11-16 | 13.5 | 3.5183134 | 0.3055 | 11.516574 | -26.07906 |
| BAL24-T0-L-A-VIRBA_16-21 | 18.5 | 2.2221847 | 0.198 | 11.223155 | -26.48833 |
| BAL24-T0-L-A-VIRBA_21-26 | 23.5 | 4.567094 | 0.298 | 15.325819 | -26.91835 |
| BAL24-T0-L-A-VIRBA_26-30 | 28 | 14.8916718 | 0.8015 | 18.579753 | -27.06007 |
| BAL24-T0-L-A-VIRBA_30-34 | 32 | 11.876732 | 0.7765 | 15.295212 | -27.7389 |
| BAL24-T0-L-A-VIRBA_34-37 | 35.5 | 14.7244447 | 0.892 | 16.507225 | -27.39818 |
| BAL24-T0-L-A-VIRBA_37-42 | 39.5 | 17.8605949 | 1.0485 | 17.034425 | NA |
| BAL24-T0-L-A-VIRBA_42-47 | 44.5 | 24.3962746 | 1.2815 | 19.03728 | -27.03801 |
| BAL24-T0-L-A-VIRBA_47-52 | 49.5 | 15.8813932 | 1.07 | 14.842424 | -27.10747 |
| BAL24-T0-L-A-VIRBA_52-57 | 54.5 | 21.2254205 | 1.114 | 19.05334 | -27.09753 |
| BAL24-T0-L-A-VIRBA_57-62 | 59.5 | 18.7040005 | 1.039 | 18.001925 | -27.09933 |
| BAL24-T0-L-A-VIRBA_62-67 | 64.5 | 19.0191548 | 0.965 | 19.708969 | -26.89464 |
| BAL24-T0-L-A-VIRBA_67-72 | 69.5 | 21.5813095 | 1.024 | 21.075498 | -27.41507 |
| BAL24-T0-L-A-VIRBA_72-77 | 74.5 | 19.2826855 | 1.0275 | 18.766604 | -26.83618 |
| BAL24-T0-L-A-VIRBA_77-82 | 79.5 | 14.6873548 | 0.824 | 17.82446 | -26.83288 |
| BAL24-T0-L-A-VIRBA_82-87 | 84.5 | 8.3422914 | 0.5415 | 15.405894 | -27.02691 |

| Prefix | mean depth [cm b.s.l.] | TOC [wt %] | TN [wt %] | C/N [-] | $\delta^{13}C$ [‰ vs. VPDB] |
|---|---|---|---|---|---|
| BAL24-T0-L-A-VIRBA_87-91 | 89 | 7.6817501 | 0.817 | 9.402387 | -27.20079 |
| BAL24-T0-L-A-VIRBA_91-96 | 93.5 | 7.3699013 | 0.5255 | 14.02455 | NA |
| BAL24-T0-L-A-VIRBA_96-98 | 97 | 5.9515512 | 0.474 | 12.556015 | -27.56028 |
| BAL24-T0-L-A-VIRBA_98-103 | 100.5 | 6.4226206 | 0.4995 | 12.858099 | -27.89548 |
| BAL24-T0-L-A-VIRBA_103-108 | 105.5 | 6.4669803 | 0.473 | 13.672263 | -27.84737 |
| BAL24-T0-L-A-VIRBA_108-113 | 110.5 | 8.045323 | 0.511 | 15.744272 | -28.6055 |
| BAL24-T0-L-A-VIRBA_113-118 | 115.5 | 6.0295037 | 0.453 | 13.310163 | -28.46013 |
| BAL24-T0-L-A-VIRBA_118-123 | 120.5 | 5.6388233 | 0.443 | 12.728721 | -28.22503 |
| BAL24-T0-L-A-VIRBA_123-127 | 125 | 4.7733779 | 0.3355 | 14.227654 | -27.59902 |
| BAL24-T0-L-A-VIRBA_127-137 | 132 | 13.6370179 | 0.7455 | 18.292445 | NA |
| BAL24-T0-L-A-VIRBA_137-140 | 138.5 | 14.8954943 | 0.8285 | 17.978871 | -27.02562 |
| BAL24-T0-L-A-VIRBA_140-145 | 142.5 | 1.7520784 | 0.138 | 12.696221 | -27.06198 |
| BAL24-T0-L-A-VIRBA_145-150 | 147.5 | 1.7155261 | 0.1135 | 15.114767 | -26.93592 |
| BAL24-T0-L-A-VIRBA_150-155 | 152.5 | 2.0590155 | 0.1555 | 13.241257 | -26.73859 |
| BAL24-T0-L-A-VIRBA_155-160 | 157.5 | 1.7832901 | 0.1255 | 14.209483 | -26.78139 |
| BAL24-T0-L-A-VIRBA_160-165 | 162.5 | 1.7157634 | 0.1555 | 11.033848 | -26.78885 |
| BAL24-T0-L-A-VIRBA_165-170 | 167.5 | 1.5202062 | 0.126 | 12.065129 | -26.80448 |
| BAL24-T0-L-A-VIRBA_170-175 | 172.5 | 1.5287158 | 0.1225 | 12.479313 | -26.64466 |
| BAL24-T0-L-A-VIRBA_175-181 | 178 | 1.4364977 | 0.1135 | 12.656368 | -26.52386 |
| BAL24-T0-L-VIRBA_181-187 | 184 | 1.3388378 | 0.1075 | 12.454305 | -26.25675 |
| BAL24-T0-L-A-VIRBA_187-193 | 190 | 1.5501021 | 0.118 | 13.136459 | -26.45784 |
| BAL24-T0-L-A-VIRBA_193-198 | 195.5 | 1.6936209 | 0.01 | NA | NA |
| BAL24-T0-L-A-VIRBA_198-201 | 199.5 | 1.8165475 | 0.1335 | 13.607098 | -26.65473 |
| BAL24-T0-L-A-VIRBA_201-206 | 203.5 | 1.6903925 | 0.1325 | 12.75768 | -26.72718 |
| BAL24-T0-L-A-VIRBA_206-211 | 208.5 | 1.5854789 | 0.106 | 14.957349 | -26.78911 |
| BAL24-T0-L-A-VIRBA_211-216 | 213.5 | 2.4843497 | 0.1795 | 13.840388 | -26.69328 |
| BAL24-T0-L-A-VIRBA_216-221 | 218.5 | 2.4439894 | 0.1785 | 13.691817 | -26.81237 |
| BAL24-T0-L-A-VIRBA_221-226 | 223.5 | 2.2634744 | 0.2075 | 10.90831 | -26.46927 |
| BAL24-T0-L-A-VIRBA_226-231 | 228.5 | 3.4450036 | 0.234 | 14.722238 | -26.85643 |
| BAL24-T0-L-A-VIRBA_231-241 | 236 | 2.7923137 | 0.176 | 15.865419 | NA |
| BAL24-T0-L-A-VIRBA_241-244 | 242.5 | 2.7969065 | 0.226 | 12.375693 | -26.40654 |
| BAL24-T0-L-A-VIRBA_244-249 | 246.5 | 2.145 | 0.1995 | 10.75188 | -26.19399 |
| BAL24-T0-L-A-VIRBA_249-254 | 251.5 | 1.5864755 | 0.152 | 10.437339 | -25.91843 |
| BAL24-T0-L-A-VIRBA_254-259 | 256.5 | 1.5307057 | 0.148 | 10.342606 | -25.93311 |
| BAL24-T0-L-A-VIRBA_259-264 | 261.5 | 2.0488653 | 0.1635 | 12.531286 | -26.11144 |
| BAL24-T0-L-A-VIRBA_264-269 | 266.5 | 1.721033 | 0.152 | 11.322586 | -25.91325 |
| BAL24-T0-L-A-VIRBA_269-274 | 271.5 | 0.6743496 | 0.01 | NA | -26.11358 |
| BAL24-T0-L-A-VIRBA_274-279 | 276.5 | 1.1531283 | 0.1245 | 9.262075 | -25.44191 |
| BAL24-T0-L-A-VIRBA_279-285 | 282 | 0.9227866 | 0.01 | NA | -25.14901 |
| BAL24-T0-L-A-VIRBA_285-291 | 288 | 0.9332479 | 0.01 | NA | -24.97012 |
| BAL24-T0-L-A-VIRBA_291-297 | 294 | 0.6033988 | 0.01 | NA | -24.7424 |
| BAL24-T0-L-A-VIRBA_297-307 | 302 | 1.5378102 | 0.01 | NA | NA |
| BAL24-T0-L-A-VIRBA_307-311 | 309 | 1.5555746 | 0.13575 | 11.459113 | -25.74635 |
| BAL24-T0-DLB-A_0-1 | 0.5 | 18.380763 | 1.5735 | 11.68145 | -36.49745 |
| BAL24-T0-DLB-A_1-11 | 6 | 8.097071 | 0.536 | 15.10648 | NA |
| BAL24-T0-DLB-A_11-13 | 12 | 5.153482 | 0.3485 | 14.78761 | -26.33504 |
| BAL24-T0-DLB-A_13-19 | 16 | 3.357859 | 0.2305 | 14.56772 | -26.25033 |

| Prefix | mean depth [cm b.s.l.] | TOC [wt %] | TN [wt %] | C/N [-] | $\delta^{13}C$ [‰ vs. VPDB] |
|---|---|---|---|---|---|
| BAL24-T0-DLB-A_19-23 | 21 | 2.761938 | 0.2305 | 11.98238 | -25.92509 |
| BAL24-T0-DLB-A_23-27 | 25 | 2.385997 | 0.2045 | 11.66747 | -25.71227 |
| BAL24-T0-DLB-A_27-32 | 29.5 | 2.417581 | 0.2035 | 11.88001 | -24.97002 |
| BAL24-T0-DLB-A_32-38 | 35 | 3.09344 | 0.2595 | 11.92077 | -25.09181 |
| BAL24-T0-DLB-A_38-42 | 40 | 2.181106 | 0.199 | 10.96033 | -24.93879 |
| BAL24-T0-DLB-A_42-46 | 44 | 2.626967 | 0.2415 | 10.87771 | -25.15381 |
| BAL24-T0-DLB-A_46-51 | 48.5 | 2.442182 | 0.222 | 11.00082 | -25.0079 |
| BAL24-T0-DLB-A_51-56 | 53.5 | 3.232071 | 0.257 | 12.57615 | NA |
| BAL24-T0-DLB-A_56-58 | 57 | 2.938902 | 0.23 | 12.77784 | -24.99468 |
| BAL24-T0-DLB-A_58-65 | 61.5 | 3.422192 | 0.2775 | 12.33222 | -25.19139 |
| BAL24-T0-DLB-A_65-69 | 67 | 3.341776 | 0.2725 | 12.2634 | -25.60757 |
| BAL24-T0-DLB-A_69-73 | 71 | 3.376273 | 0.2835 | 11.90925 | -25.50874 |
| BAL24-T0-DLB-A_73-78 | 75.5 | 4.835132 | 0.377 | 12.82528 | -26.10669 |
| BAL24-T0-DLB-A_78-84 | 81 | 3.705011 | 0.3145 | 11.78064 | -25.78487 |
| BAL24-T0-DLB-A_84-90 | 87 | 2.813204 | 0.2345 | 11.9966 | -25.37337 |
| BAL24-T0-DLB-A_90-96 | 93 | 2.722128 | 0.24475 | 11.12207 | -25.69591 |
| BAL24-T0-DLB-A_96-106 | 101 | 3.439864 | 0.2565 | 13.41077 | NA |
| BAL24-T0-DLB-A_106-108 | 107 | 3.039286 | 0.2205 | 13.78361 | -25.81563 |
| BAL24-T0-DLB-A_108-113 | 110.5 | 3.5208 | 0.2615 | 13.46386 | -26.29006 |
| BAL24-T0-DLB-A_113-118 | 115.5 | 2.773378 | 0.21575 | 12.85459 | -25.43005 |
| BAL24-T0-DLB-A_118-123 | 120.5 | 3.503892 | 0.2705 | 12.95339 | -25.77751 |
| BAL24-T0-DLB-A_123-128 | 125.5 | 3.728514 | 0.2935 | 12.70363 | -25.77952 |
| BAL24-T0-DLB-A_128-133 | 130.5 | 3.323376 | 0.2325 | 14.29409 | -25.96818 |
| BAL24-T0-DLB-A_133-137 | 135 | 2.520167 | 0.187 | 13.47683 | -25.85085 |
| BAL24-T0-DLB-A_137-142 | 139.5 | 2.173149 | 0.15825 | 13.73238 | -25.63851 |
| BAL24-T0-DLB-A_142-147 | 144.5 | 1.796353 | 0.162 | 11.0886 | -25.0832 |
| BAL24-T0-DLB-A_147-152 | 149.5 | 2.953993 | 0.186 | 15.88168 | NA |
| BAL24-T0-DLB-A_152-154 | 153 | 2.449105 | 0.1725 | 14.19771 | -25.30685 |
| BAL24-T0-DLB-A_154-159 | 156.5 | 1.716261 | 0.1415 | 12.12905 | -25.00082 |
| BAL24-T0-DLB-A_159-164 | 161.5 | 1.372018 | 0.112 | 12.25016 | -24.69777 |
| BAL24-T0-DLB-A_164-169 | 166.5 | 1.191931 | 0.117 | 10.18744 | -24.45007 |
| BAL24-T0-DLB-A_169-174 | 171.5 | 1.373012 | 0.10825 | 12.68372 | -24.87394 |
| BAL24-T0-DLB-A_174-179 | 176.5 | 1.548614 | 0.142 | 10.90574 | -25.03603 |
| BAL24-T0-DLB-A_179-184 | 181.5 | 1.244712 | 0.01 | NA | -24.93435 |
| BAL24-T0-DLB-A_184-189 | 186.5 | 1.577965 | 0.1345 | 11.73208 | -24.79041 |
| BAL24-T0-DLB-A_189-194 | 191.5 | 1.466503 | 0.12 | 12.22086 | -25.03898 |
| BAL24-T0-DLB-A_194-199 | 196.5 | 1.559061 | 0.1405 | 11.09652 | -24.92143 |
| BAL24-T0-DLB-A_199-209 | 204 | 1.416598 | 0.01 | NA | NA |
| BAL24-T0-DLB-A_209-214 | 211.5 | 1.373285 | 0.118 | 11.638 | -24.51508 |
| BAL24-T0-M1-PUSH_0-5 | 2.5 | 3.033437 | 0.2095 | 14.47941 | -26.45659 |
| BAL24-T0-M1-PUSH_5-10 | 7.5 | 2.733394 | 0.1385 | 19.7357 | NA |
| BAL24-T0-M1-PUSH_10-13 | 11.5 | 2.759908 | 0.1785 | 15.46167 | -26.62513 |
| BAL24-T0-M1-PUSH_13-18 | 15.5 | 1.961512 | 0.1505 | 13.0333 | -26.48704 |
| BAL24-T0-M1-PUSH_18-23 | 20.5 | 2.228241 | 0.1595 | 13.97016 | -26.55382 |
| BAL24-T0-M1-PUSH_23-28 | 25.5 | 1.942485 | 0.01 | NA | NA |
| BAL24-T0-M1-PUSH_28-33 | 30.5 | 1.977977 | 0.1265 | 15.63619 | -26.31708 |
| BAL24-T0-M1-PUSH_33-38 | 35.5 | 1.362283 | 0.115 | 11.84594 | -26.00289 |

| Prefix | mean depth [cm b.s.l.] | TOC [wt %] | TN [wt %] | C/N [-] | $\delta^{13}C$ [‰ vs. VPDB] |
|---|---|---|---|---|---|
| BAL24-T0-M1-PUSH_38-42 | 40 | 1.535652 | 0.01 | NA | -25.88241 |
| BAL24-T0-M1-PUSH_42-47 | 44.5 | 1.143047 | 0.01 | NA | NA |
| BAL24-T0-M1-PUSH_47-52 | 49.5 | 1.180917 | 0.01 | NA | -25.95536 |
| BAL24-T0-M1-PUSH_52-55 | 53.5 | 1.490674 | 0.01 | NA | -26.1697 |

*Table A. 4. Raw data of the biomarker parameters.*

| Prefix | mean depth [cm b.s.l.] | alkane conc. $C_{21-35}$ [µg $gSed^{-1}$] | alkane conc. $C_{21-35}$ [µg $gTOC^{-1}$] | $P_{aq}$ $C_{23-33}$ [-] | $P_{wax}$ $C_{23-33}$ [-] | CPI $C_{23-33}$ [-] | ACL $C_{23-33}$ [-] |
|---|---|---|---|---|---|---|---|
| BAL24-T0-UL-A_22-32 | 27 | 1115.15277 | 3439.70626 | 0.02181736 | 0.9795025 | 76.878005 | 30.19112 |
| BAL24-T0-UL-A_37-42 | 39.5 | 11.050796 | 597.66338 | 0.20080849 | 0.8316055 | 6.926095 | 28.65358 |
| BAL24-T0-UL-A_63-73 | 68 | 2.36492 | 67.32657 | 0.54065125 | 0.6812005 | 8.078622 | 26.77215 |
| BAL24-T0-UL-A_142-150 | 146 | 4.265215 | 97.33112 | 0.68729556 | 0.574889 | 4.559737 | 26.32625 |
| BAL24-T0-UL-A_186-196 | 191 | 6.161974 | 76.12074 | 0.46638166 | 0.7563173 | 13.586647 | 27.01829 |
| BAL24-T0-L-A-VIRBA_1-11 | 6 | 4.272079 | 97.13686 | 0.46839374 | 0.7314854 | 14.242161 | 27.09811 |
| BAL24-T0-L-A-VIRBA_37-42 | 39.5 | 160.170444 | 896.76079 | 0.05124576 | 0.9561071 | 30.805571 | 29.51639 |
| BAL24-T0-L-A-VIRBA_91-96 | 93.5 | 9.571823 | 129.87722 | 0.24752499 | 0.8450576 | 20.287753 | 28.04895 |
| BAL24-T0-L-A-VIRBA_127-137 | 132 | 84.069858 | 616.48352 | 0.08480376 | 0.9336935 | 30.788197 | 29.10213 |
| BAL24-T0-L-A-VIRBA_193-198 | 195.5 | 1.604963 | 94.76516 | 0.14178045 | 0.8806197 | 9.625946 | 29.00176 |
| BAL24-T0-L-A-VIRBA_231-241 | 236 | 15.756902 | 564.29554 | 0.14874058 | 0.8833486 | 15.774501 | 28.7813 |
| BAL24-T0-DLB-A_1-11 | 6 | 39.8535716 | 492.2017 | 0.148614 | 0.8808532 | 14.829638 | 28.8919 |
| BAL24-T0-DLB-A_51-56 | 53.5 | 2.6537584 | 82.10706 | 0.3525095 | 0.7291223 | 10.289443 | 28.21858 |
| BAL24-T0-DLB-A_96-106 | 101 | 2.2281591 | 64.77463 | 0.5904245 | 0.6415702 | 10.55633 | 26.66692 |
| BAL24-T0-DLB-A_147-152 | 149.5 | 9.9973378 | 338.43475 | 0.7355769 | 0.592202 | 8.316762 | 26.28606 |
| BAL24-T0-DLB-A_199-209 | 204 | 0.4320802 | 30.50125 | 0.3901185 | 0.6958903 | 4.046167 | 27.68644 |
| BAL24-T0-M1-PUSH_5-10 | 7.5 | 3.995972 | 146.1908 | 0.3679285 | 0.7351091 | 9.934087 | 27.56853 |
| BAL24-T0-M1-PUSH_23-28 | 25.5 | 8.030239 | 413.4004 | 0.4511478 | 0.7026432 | 4.315528 | 27.10998 |
| BAL24-T0-M1-PUSH_42-47 | 44.5 | 3.084785 | 269.8739 | 0.4696408 | 0.6834221 | 7.009157 | 27.03258 |

*Table A. 5. Raw data of the radiocarbon ages.*

| Prefix | mean depth [cm b.s.l.] | $^{14}C$ age mean [cal. ka BP] | $^{14}C$ age min. [cal. ka BP] | $^{14}C$ age max. [cal. ka BP] | range [ka BP] |
|---|---|---|---|---|---|
| BAL24-T0-UL-A_20-22 | 21 | 0.086 | 0.032 | 0.14 | 0.108 |
| BAL24-T0-UL-A_61-63 | 62 | 30.2915 | 30.175 | 30.408 | 0.233 |
| BAL24-T0-UL-A_100-103 | 101.5 | 34.385 | 34.198 | 34.572 | 0.374 |
| BAL24-T0-UL-A_142-150 | 146 | 34.4765 | 34.29 | 34.663 | 0.373 |
| BAL24-T0-UL-A_196-202 | 199 | 32.7775 | 32.269 | 33.286 | 1.017 |
| BAL24-T0-L-A-VIRBA_34-37 | 35.5 | 0.2975 | 0.287 | 0.308 | 0.021 |
| BAL24-T0-L-A-VIRBA_96-98 | 97 | 0.3965 | 0.36 | 0.433 | 0.073 |
| BAL24-T0-L-A-VIRBA_137-140 | 138.5 | 0.4805 | 0.458 | 0.503 | 0.045 |
| BAL24-T0-L-A-VIRBA_198-201 | 199.5 | 2.27 | 2.24 | 2.3 | 0.06 |
| BAL24-T0-L-A-VIRBA_241-244 | 242.5 | 11.9155 | 11.829 | 12.002 | 0.173 |
| BAL24-T0-L-A-VIRBA_307-311 | 309 | 1.5335 | 1.517 | 1.55 | 0.033 |
| BAL24-T0-DLB-A_11-13 | 12 | 1.1155 | 1.054 | 1.177 | 0.123 |
| BAL24-T0-DLB-A_56-58 | 57 | 50 | 50 | 50 | 0 |
| BAL24-T0-DLB-A_106-108 | 107 | 50 | 50 | 50 | 0 |
| BAL24-T0-DLB-A_152-154 | 153 | 50 | 50 | 50 | 0 |

# Appendix

| Prefix | mean depth [cm b.s.l.] | $^{14}$C age mean [cal. ka BP] | $^{14}$C age min. [cal. ka BP] | $^{14}$C age max. [cal. ka BP] | range [ka BP] |
|---|---|---|---|---|---|
| BAL24-T0-DLB-A_209-214 | 211.5 | 50 | 50 | 50 | 0 |
| BAL24-T0-M1-PUSH_10-13 | 11.5 | 0.8 | 0.684 | 0.916 | 0.232 |
| BAL24-T0-M1-PUSH_52-55 | 53.5 | 28.221 | 27.678 | 28.764 | 1.086 |

*Table A. 6. Biomarker statistics for the four cores.*

| Core | Parameter | n.valid | min | med | max | mean | sd |
|---|---|---|---|---|---|---|---|
| DLB | ACL $C_{23-33}$ [-] | 5 | 26.29 | 27.69 | 28.89 | 27.55 | 1.08 |
| | CPI $C_{23-33}$ [-] | 5 | 4.05 | 10.29 | 14.83 | 9.61 | 3.91 |
| | Long-chain alkane conc. $C_{21-35}$ [µg $gSed^{-1}$] | 5 | 0.43 | 2.65 | 39.85 | 11.03 | 16.52 |
| | Long-chain alkane conc. $C_{21-35}$ [µg $gTOC^{-1}$] | 5 | 30.50 | 82.11 | 492.20 | 201.60 | 203.38 |
| | $P_{aq}$ $C_{23-33}$ [-] | 5 | 0.15 | 0.39 | 0.74 | 0.44 | 0.23 |
| | $P_{wax}$ $C_{23-33}$ [-] | 5 | 0.59 | 0.70 | 0.88 | 0.71 | 0.11 |
| L | ACL $C_{23-33}$ [-] | 7 | 26.72 | 28.78 | 29.52 | 28.32 | 1.07 |
| | CPI $C_{23-33}$ [-] | 7 | 4.17 | 15.77 | 30.81 | 17.96 | 10.11 |
| | Long-chain alkane conc. $C_{21-35}$ [µg $gSed^{-1}$] | 7 | 1.60 | 9.57 | 160.17 | 39.74 | 60.60 |
| | Long-chain alkane conc. $C_{21-35}$ [µg $gTOC^{-1}$] | 7 | 94.77 | 177.70 | 896.76 | 368.15 | 321.66 |
| | $P_{aq}$ $C_{23-33}$ [-] | 7 | 0.05 | 0.15 | 0.56 | 0.24 | 0.20 |
| | $P_{wax}$ $C_{23-33}$ [-] | 7 | 0.63 | 0.88 | 0.96 | 0.84 | 0.12 |
| M | ACL $C_{23-33}$ [-] | 3 | 27.03 | 27.11 | 27.57 | 27.24 | 0.29 |
| | CPI $C_{23-33}$ [-] | 3 | 4.32 | 7.01 | 9.93 | 7.09 | 2.81 |
| | Long-chain alkane conc. $C_{21-35}$ [µg $gSed^{-1}$] | 3 | 3.08 | 4.00 | 8.03 | 5.04 | 2.63 |
| | Long-chain alkane conc. $C_{21-35}$ [µg $gTOC^{-1}$] | 3 | 146.19 | 269.87 | 413.40 | 276.49 | 133.73 |
| | $P_{aq}$ $C_{23-33}$ [-] | 3 | 0.37 | 0.45 | 0.47 | 0.43 | 0.05 |
| | $P_{wax}$ $C_{23-33}$ [-] | 3 | 0.68 | 0.70 | 0.74 | 0.71 | 0.03 |
| UL | ACL $C_{23-33}$ [-] | 5 | 26.33 | 27.02 | 30.19 | 27.79 | 1.60 |
| | CPI $C_{23-33}$ [-] | 5 | 4.56 | 8.08 | 76.88 | 22.01 | 30.85 |
| | Long-chain alkane conc. $C_{21-35}$ [µg $gSed^{-1}$] | 5 | 2.36 | 6.16 | 1115.15 | 227.80 | 496.06 |
| | Long-chain alkane conc. $C_{21-35}$ [µg $gTOC^{-1}$] | 5 | 67.33 | 97.33 | 3439.71 | 855.63 | 1461.85 |
| | $P_{aq}$ $C_{23-33}$ [-] | 5 | 0.02 | 0.47 | 0.69 | 0.38 | 0.27 |
| | $P_{wax}$ $C_{23-33}$ [-] | 5 | 0.57 | 0.76 | 0.98 | 0.76 | 0.15 |

*Table A. 7. Sedimentological statistics for the three permafrost layers.*

| Permafrost layer | Paramter | n.valid | min | med | max | mean | sd |
|---|---|---|---|---|---|---|---|
| active layer | Absolute ice / water content [wt%] | 8 | 26.96 | 72.83 | 89.78 | 64.60 | 23.95 |
| | Clay [vol %] | 1 | 4.09 | 4.09 | 4.09 | 4.09 | NA |
| | Mean grain size [µm] | 1 | 22.24 | 22.24 | 22.24 | 22.24 | NA |
| | Sand acc. [vol %] | 1 | 100.00 | 100.00 | 100.00 | 100.00 | NA |
| | Sand [vol %] | 1 | 14.14 | 14.14 | 14.14 | 14.14 | NA |
| | Silt acc. [vol %] | 1 | 85.86 | 85.86 | 85.86 | 85.86 | NA |
| | Silt [vol %] | 1 | 81.77 | 81.77 | 81.77 | 81.77 | NA |
| perennial frozen | Absolute ice / water content [wt%] | 60 | 27.07 | 40.94 | 99.92 | 46.01 | 15.84 |
| | Clay [vol %] | 60 | 2.48 | 4.20 | 6.07 | 4.21 | 0.77 |
| | Mean grain size [µm] | 60 | 18.22 | 23.15 | 32.36 | 24.21 | 3.33 |
| | Sand acc. [vol %] | 60 | 99.72 | 100.00 | 100.00 | 100.00 | 0.04 |
| | Sand [vol %] | 60 | 12.19 | 17.21 | 24.76 | 17.80 | 2.80 |
| | Silt acc. [vol %] | 60 | 75.24 | 82.79 | 87.81 | 82.19 | 2.79 |
| | Silt [vol %] | 60 | 72.76 | 78.27 | 82.28 | 77.98 | 2.33 |
| talik | Absolute ice / water content [wt%] | 66 | 22.29 | 28.58 | 67.48 | 35.16 | 12.61 |
| | Clay [vol %] | 60 | 1.60 | 4.29 | 9.29 | 4.32 | 1.55 |
| | Mean grain size [µm] | 60 | 10.43 | 21.74 | 61.17 | 24.52 | 9.69 |
| | Sand acc. [vol %] | 60 | 99.98 | 100.00 | 100.00 | 100.00 | 0.00 |
| | Sand [vol %] | 60 | 4.31 | 14.15 | 51.29 | 17.93 | 9.68 |
| | Silt acc. [vol %] | 60 | 48.71 | 85.85 | 95.69 | 82.07 | 9.68 |
| | Silt [vol %] | 60 | 47.10 | 81.27 | 88.24 | 77.75 | 8.46 |

*Table A. 8. Biogeochemical statistics for the three permafrost layers.*

| Permafrost layer | Parameter | n.valid | min | med | max | mean | sd |
|---|---|---|---|---|---|---|---|
| active layer | TN [wt%] | 8 | 0.11 | 1.13 | 2.01 | 1.07 | 0.74 |
| | TOC [wt%] | 8 | 1.85 | 25.40 | 44.42 | 23.36 | 17.93 |
| | C/N [-] | 8 | 11.68 | 16.96 | 42.02 | 21.15 | 11.23 |
| | $\delta^{13}C$ [‰ vs. VPDB] | 5 | -36.50 | -28.32 | -27.29 | -29.96 | 3.76 |
| perennial frozen | TN [wt%] | 70 | 0.01 | 0.28 | 0.82 | 0.30 | 0.14 |
| | TOC [wt%] | 70 | 1.19 | 3.45 | 16.28 | 3.85 | 2.15 |
| | C/N [-] | 69 | 9.07 | 12.16 | 19.97 | 12.55 | 1.64 |

| Permafrost layer | Parameter | n.valid | min | med | max | mean | sd |
|---|---|---|---|---|---|---|---|
| | $\delta^{13}C$ [‰ vs. VPDB] | 63 | -27.62 | -25.97 | -24.45 | -25.84 | 0.65 |
| talik | TN [wt%] | 77 | 0.01 | 0.16 | 1.28 | 0.33 | 0.34 |
| | TOC [wt%] | 77 | 0.60 | 2.22 | 24.40 | 5.37 | 6.12 |
| | C/N [-] | 65 | 9.26 | 13.61 | 21.08 | 14.06 | 2.80 |
| | $\delta^{13}C$ [‰ vs. VPDB] | 67 | -28.61 | -26.65 | -24.52 | -26.58 | 0.83 |

*Table A. 9. Hydrochemical statistics for the three permafrost layers.*

| Permafrost layer | Parameter | n.valid | min | med | max | mean | sd |
|---|---|---|---|---|---|---|---|
| active layer | DOC [mg $L^{-1}$] | 1 | 42.05 | 42.05 | 42.05 | 42.05 | NA |
| | EC [µS $cm^{-1}$] | 1 | 44.62 | 44.62 | 44.62 | 44.62 | NA |
| | Mean d excess [-] | 1 | 8.37 | 8.37 | 8.37 | 8.37 | NA |
| | Mean $\delta^{18}O$ [‰ vs. SMOW] | 1 | -15.08 | -15.08 | -15.08 | -15.08 | NA |
| | Mean δD [‰ vs. SMOW] | 1 | -112.28 | -112.28 | -112.28 | -112.28 | NA |
| | pH [-] | 1 | 4.87 | 4.87 | 4.87 | 4.87 | NA |
| perennial frozen | DOC [mg $L^{-1}$] | 30 | 5.78 | 199.08 | 1707.00 | 324.27 | 418.22 |
| | EC [µS $cm^{-1}$] | 30 | 43.41 | 870.50 | 2379.00 | 819.49 | 576.28 |
| | Mean d excess [-] | 25 | -3.06 | 4.85 | 14.60 | 5.39 | 4.03 |
| | Mean $\delta^{18}O$ [‰ vs. SMOW] | 25 | -20.36 | -18.89 | -14.25 | -17.88 | 1.99 |
| | Mean δD [‰ vs. SMOW] | 25 | -160.21 | -142.65 | -112.15 | -137.62 | 14.49 |
| | pH [-] | 30 | 5.68 | 7.66 | 8.41 | 7.37 | 0.73 |
| talik | DOC [mg $L^{-1}$] | 26 | 41.38 | 147.55 | 312.25 | 149.36 | 54.81 |
| | EC [µS $cm^{-1}$] | 26 | 91.00 | 701.80 | 20390.00 | 2761.55 | 6007.52 |
| | Mean d excess [-] | 20 | -1.17 | 0.10 | 6.95 | 0.87 | 2.22 |
| | Mean $\delta^{18}O$ [‰ vs. SMOW] | 20 | -18.95 | -18.31 | -13.14 | -17.54 | 1.92 |
| | Mean δD [‰ vs. SMOW] | 20 | -152.39 | -146.79 | -101.57 | -139.48 | 17.02 |
| | pH [-] | 26 | 7.22 | 7.75 | 8.22 | 7.76 | 0.24 |

*Table A. 10. Biomarker statistics for the three permafrost layers.*

| Permafrost layer | Paramter | n.valid | min | med | max | mean | sd |
|---|---|---|---|---|---|---|---|
| active layer | ACL $C_{23\text{-}33}$ [-] | 3 | 28.65 | 28.89 | 30.19 | 29.25 | 0.83 |
| | CPI $C_{23\text{-}33}$ [-] | 3 | 6.93 | 14.83 | 76.88 | 32.88 | 38.31 |
| | Long-chain alkane conc. $C_{21\text{-}35}$ [µg $gSed^{-1}$] | 3 | 11.05 | 39.85 | 1115.15 | 388.69 | 629.30 |
| | Long-chain alkane conc. $C_{21\text{-}35}$ [µg $gTOC^{-1}$] | 3 | 492.20 | 597.66 | 3439.71 | 1509.86 | 1672.13 |
| | $P_{aq}$ $C_{23\text{-}33}$ [-] | 3 | 0.02 | 0.15 | 0.20 | 0.12 | 0.09 |
| | $P_{wax}$ $C_{23\text{-}33}$ [-] | 3 | 0.83 | 0.88 | 0.98 | 0.90 | 0.08 |
| perennial frozen | ACL $C_{23\text{-}33}$ [-] | 6 | 26.29 | 26.72 | 28.22 | 26.88 | 0.71 |
| | CPI $C_{23\text{-}33}$ [-] | 6 | 4.56 | 9.30 | 13.59 | 9.23 | 3.03 |
| | Long-chain alkane conc. $C_{21\text{-}35}$ [µg $gSed^{-1}$] | 6 | 2.23 | 3.46 | 10.00 | 4.61 | 3.04 |
| | Long-chain alkane conc. $C_{21\text{-}35}$ [µg $gTOC^{-1}$] | 6 | 64.77 | 79.11 | 338.43 | 121.02 | 107.15 |
| | $P_{aq}$ $C_{23\text{-}33}$ [-] | 6 | 0.35 | 0.57 | 0.74 | 0.56 | 0.14 |
| | $P_{wax}$ $C_{23\text{-}33}$ [-] | 6 | 0.57 | 0.66 | 0.76 | 0.66 | 0.07 |
| talik | ACL $C_{23\text{-}33}$ [-] | 11 | 26.72 | 27.69 | 29.52 | 27.97 | 0.98 |
| | CPI $C_{23\text{-}33}$ [-] | 11 | 4.05 | 9.93 | 30.81 | 13.73 | 9.90 |
| | Long-chain alkane conc. $C_{21\text{-}35}$ [µg $gSed^{-1}$] | 11 | 0.43 | 4.27 | 160.17 | 26.70 | 50.34 |
| | Long-chain alkane conc. $C_{21\text{-}35}$ [µg $gTOC^{-1}$] | 11 | 30.50 | 177.70 | 896.76 | 312.45 | 275.98 |
| | $P_{aq}$ $C_{23\text{-}33}$ [-] | 11 | 0.05 | 0.37 | 0.56 | 0.31 | 0.18 |
| | $P_{wax}$ $C_{23\text{-}33}$ [-] | 11 | 0.63 | 0.74 | 0.96 | 0.79 | 0.11 |

# Appendix

*Figure A. 1. Core BAL24-T0-UL with the sedimentological and cryolithological core description.*

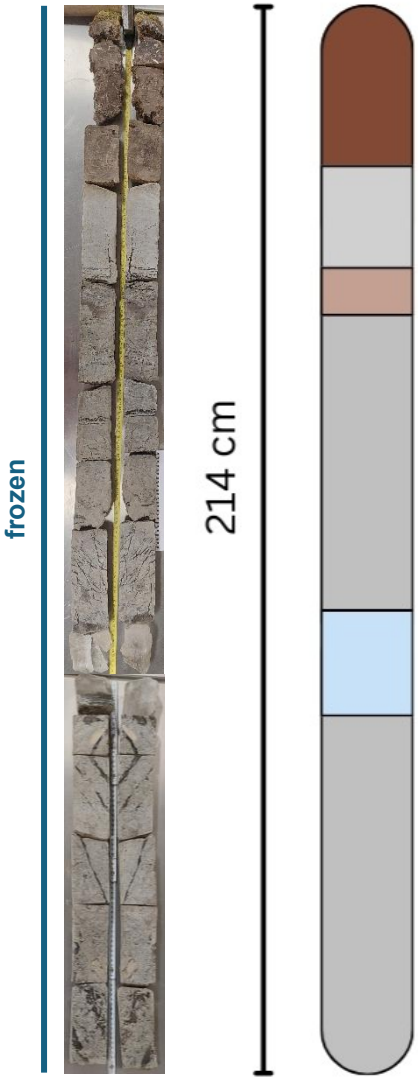


| Depth [cm b.s.l.] | |
|---|---|
| 0 – 20 | Peat, brown, porous, structureless, large macro remains (0.5*2 cm) |
| 20 – 32 | Slightly silty, organic rich, brown, structureless, macro remains (roots) |
| 32 – 42 | Silty, light grey, micro lenticular – wavy, no plants / organics visible |
| 42 – 52 | Silty, (light) grey, horizontal bands at 50 – 53 (<0.5 cm), vertical ice band (>0.5 cm) |
| 52 – 57 | Lenticular structure (few mm), >0.5 cm horizontal ice structure, ice bands at top (0.5 cm) |
| 57 – 61 | Silty, slightly organic, grey-brown, micro lenticular horizontal ice structure |
| 61 – 73 | Silty grey, dominantly horizontal ice veins <2*8 mm, vertical ice veins <1mm wide, few 45° angular veins <4*0.1 cm, irregular-reticulate, macro remains <3 mm |
| 73 – 81 | Silty grey, horizontal – wavy micro lenticular structure, plant remains <0.5 cm (wood) |
| 81 – 83 | Two horizontal ice bands (1 and 0.3 cm wide) |
| 83 – 90 | Silty grey, horizontal micro lenticular ice veins towards ice veins below <3 cm long, reticulate-chaotic, woody plant remains <1 cm wide |
| 90 – 103 | Silty grey, wavy micro lenticular at top, angular ice veins <2 cm long, ice band at bottom <1 cm, woody plant remains <1 cm long |
| 103 – 121 | Silty, slightly lighter grey, dominantly 45° angular ice veins <10*0.4 cm, few vertical ice veins <10*0.2 cm, darker spot 115 – 118 (3 cm wide) |
| 121- 142 | Pure ice, organics suspended, air bubbles ~2 mm (few horizontal orientated), ice wedge hit |
| 142 – 164 | Silty grey, ice rich, 45° angular <1.5 cm wide ice veins, chaotic micro lenticular structure, large woody remain 4*1.5 cm, smaller wood remains |
| 164 – 180 | Silty grey, similar as above, only one 45° angular ice vein <1 cm wide |
| 180 – 196 | Silty grey, wavy lenticular, partly structureless, small and large wood remains <3.5*2 cm |
| 196 – 214 | Silty grey, ice rich, partly ataxitic (hit ice wedge at bottom?), few little macro remains |

*Figure A. 2. Core BAL24-T0-L with the sedimentological and cryolithological core description. Corrected depths in red.*

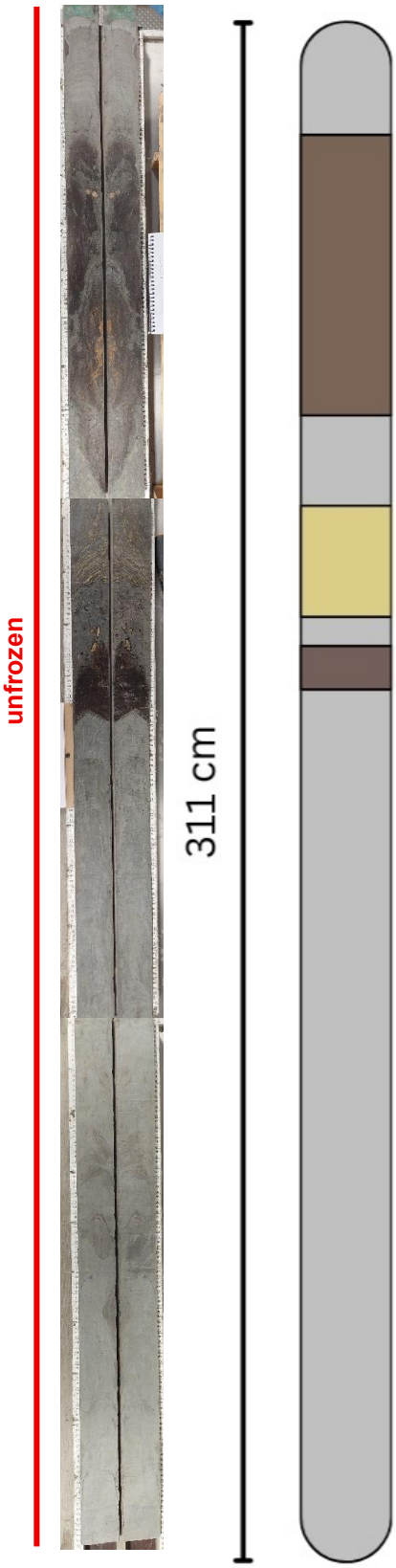


| Depth [cm b.s.l.] | |
|---|---|
| 0 – 2 / 0 – 9.4 | Silty, light grey, laminated, few woody macro remains |
| 2 – 9 / 9.4 – 41 | Silty grey, vertical organic matter intrusion, slightly laminated, few woody macro remains |
| 9 – 17 / 41 – 74.5 | Silty grey – brown, lamination <0.5-1 cm wide, few macro remains |
| 17 – 24 / 74.5 – 101.6 | Silty grey – brown, turbated, woody macro remains |
| 24 – 49 / 101.6 – 184.5 | Organic rich with vertical silty intrusions, dark brown to grey, woody macro remains <1.5*1 cm |
| 49 – 68 / 184.5 - 235 | Diagonal structure; 1. half as above, diagonal split of silty material (grey), laminated; 2. half organic rich with silty parts, light grey to light brown/brown, woody macro remains <2*1.5 cm, 62 – 79 cm / 220 – 260.1 cm woody plant macro remains <2.5 cm wide |
| 68 – 79 / 235 – 260.1 | Material as 2. half above |
| 79 – 98 / 260.1/ 297.5 | Diagonal structure; 1. half material as above, siltier, 2. half silty, grey to grey-yellowish, woody macro remains < 6*4 mm |
| 98 – 121 / 297.5 – 334.2 | Silty, grey-yellowish vertical to angular to horizontal lamination 0.5 cm wide (*Woody macro remains?*), macro remain at 106 cm / 311.2 cm 0.5*1 cm |
| 121 – 126 / 334.2 – 341.2 | Silty grey, turbated, woody macro remain 0.5*2 cm |
| 126 – 135 / 341.2 – 352.8 | Diagonal structure; 1. half as above, 2. half organic rich, dark brown, macro remains ~2 mm |
| 135 – 139 / 352.8 – 357.6 | Organic rich, darker than above, macro remains ~3 mm, end of lake sediment? |
| 139 – 148 / 357.6 – 367.8 | Silty grey |
| 148 – 201 / 367.8 – 412.4 | Silty grey, darker than above, some yellow-brownish parts, macro remains ~3mm |
| 201 – 224 / 412.4 – 425.5 | Silty grey, brow-yellowish turbations, few macro remains 4*2 mm |
| 224 – 249 / 425.5 – 436.8 | Silty grey, more organic and darker than above, brown-yellowish turbations, few macro remains 4*2 mm |
| 249 – 311 / 436.8 – 455 | Silty grey, lighter than above, black spot at 253 cm / 438.3 cm(1*1 cm), brown-greyish part at 255 – 263 cm / 439.1 – 441.9 cm with macro remains 2*4 mm, macro remain at 274 (2/3 mm), parts with very slight yellow, core catcher 293 - 311 |
| 148 – 201 / 367.8 – 412.4 | Silty grey, darker than above, some yellow-brownish parts, macro remains ~3mm |
| 201 – 224 / 412.4 – 425.5 | Silty grey, brow-yellowish turbations, few macro remains 4*2 mm |
| 224 – 249 / 425.5 – 436.8 | Silty grey, more organic and darker than above, brown-yellowish turbations, few macro remains 4*2 mm |
| 249 – 311 / 436.8 – 455 | Silty grey, lighter than above, black spot at 253 cm / 438.3 cm(1*1 cm), brown-greyish part at 255 – 263 cm / 439.1 – 441.9 cm with macro remains 2*4 mm, macro remain at 274 (2/3 mm), parts with very slight yellow, core catcher 293 - 311 |

*Figure A. 3. Core BAL24-T0-DLB with the sedimentological and cryolithological core description.*

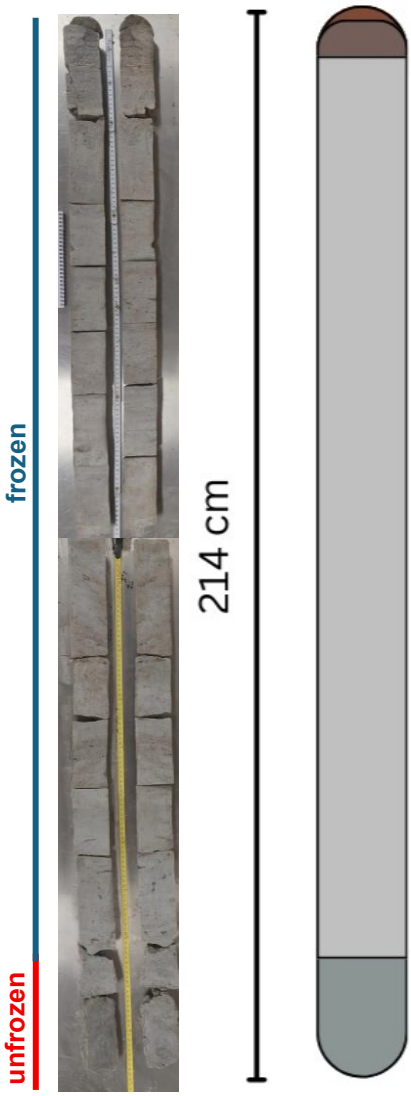


| Depth [cm b.s.l.] | |
|---|---|
| 0 – 1 | Organic rich, dark brown, plant macro remains |
| 1 – 10 | Brown-grey, horizontal and vertical ice veins <0.3*4 cm (frost cracking → Active layer), horizontal macro lenticular structure, plant macro remains 2*4 mm, frost desiccation holes |
| 10 – 13 | More grey than above, dominantly wavy micro lenticular, horizontal and vertical frost cracks, plant macro remains 1.5*5 mm |
| 13 – 27 | Grey, horizontal and bended wavy macro lenticular, signs of cryoturbation, thin ice veins <3 cm, frost desiccation holes, macro remains |
| 27 – 38 | Silty grey, massive, 2 ice veins <1.5 cm long, few macro remains |
| 38 – 42 | Silty grey, fine and dominantly horizontal ice veins, partly angular |
| 42 – 46 | Vertical frost crack, few wavy micro lenticular structures, macro remains 0.2*1 cm |
| 46 – 73 | Silty grey, ice veins at 60, macro remains <0.5 cm |
| 73 – 80 | Silty grey, angular orientation, many macro remains |
| 80 – 108 | Silty grey, massive, ice lens at 90, vertical frost crack 95 – 108, few macro remains |
| 108 – 131 | Silty grey, massive, angular orientation (Due permafrost mound frost heaving?), macro remain 1 cm long at 116 |
| 131 – 133 | Massive, horizontal orientation, large woody remains |
| 133 – 147 | Silty grey, massive and structureless, macro remains |
| 147 – 154 | Angular orientation, (micro) ice lenses <0.2*1 cm |
| 154 – 157 | Cluster of macro remains ~2 mm |
| 157 – 167 | Silty grey, massive, few macro remains |
| 167 – 189 | As above, large woody macro remains 3*0.5 cm |
| 189 – 214 | Talik, silty grey, 189 – 200 harder than below, few macrofossils |

*Figure A. 4. Core BAL24-T0-M with the sedimentological and cryolithological core description.*

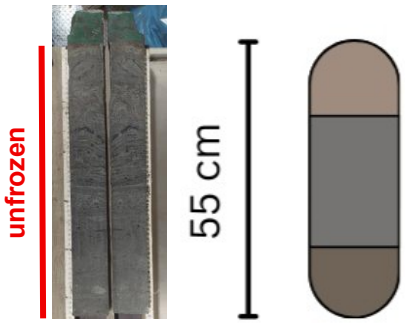


| Depth [cm b.s.l] | |
|---|---|
| 0 – 15 | Brown to grey, blackish parts at 4-8 cm, turbated due wave action, macro remains 5 x 2 mm |
| 15 – 29 | Silty, grey to black, laminations, few macro remains up to 4x4 cm, water lenses 0.5x1 cm, pebble at 26 cm |
| 29 – 41 | Silty, grey to black, fading lamination, black dots, two macro remains 2x4 cm |
| 41 – 49 | Dark grey-brownish, no lamination |
| 49 – 55 | Sandy with small pebbles 1-5mm, large pebble at 49 with 3x2 cm |

*Figure A. 5. Example of a gas chromatogram and mass spectra in Xcalibur (Thermo Fischer).*

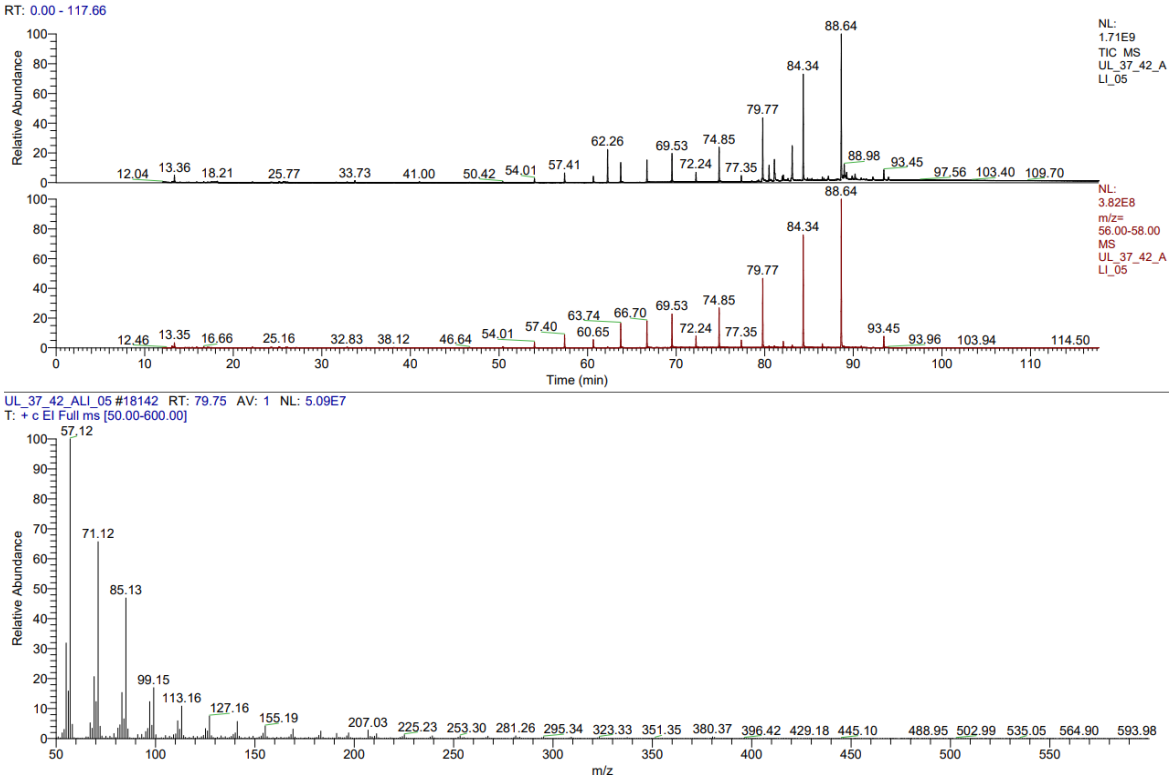


*Figure A. 6. Result of the exponential compaction correction for the core length of BAL24-T0-L.*

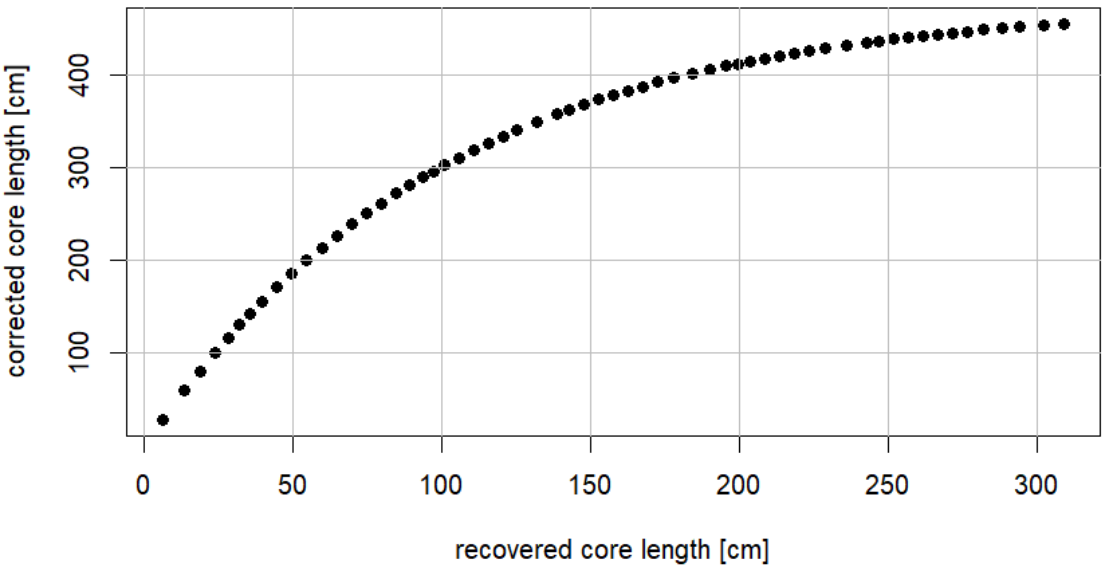

*Figure A. 7. Correlation matrix of all parameters.*

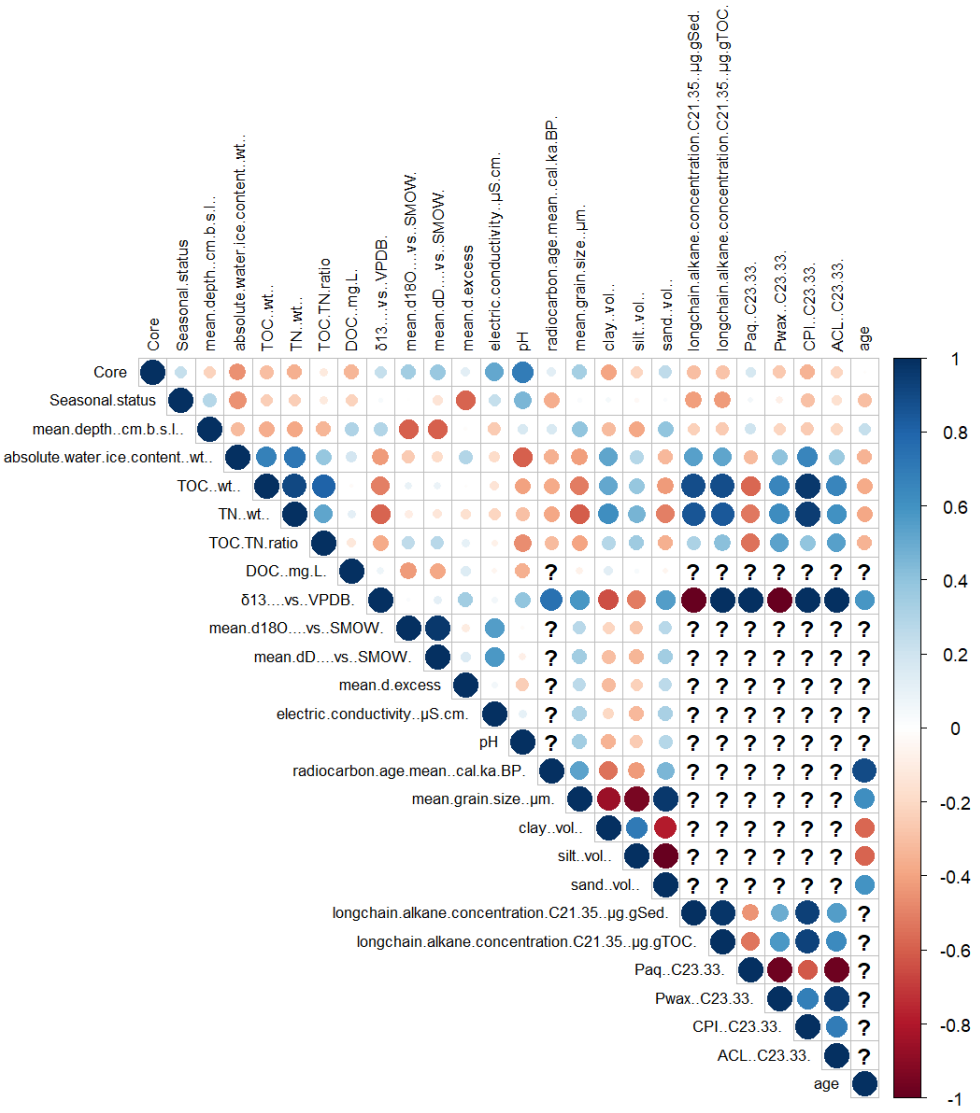

*Figure A. 8. Biplot of the PCA-Analysis with biomarker proxies as supplementary variables, colored after (a) cores and (b) permafrost layer.*

a)

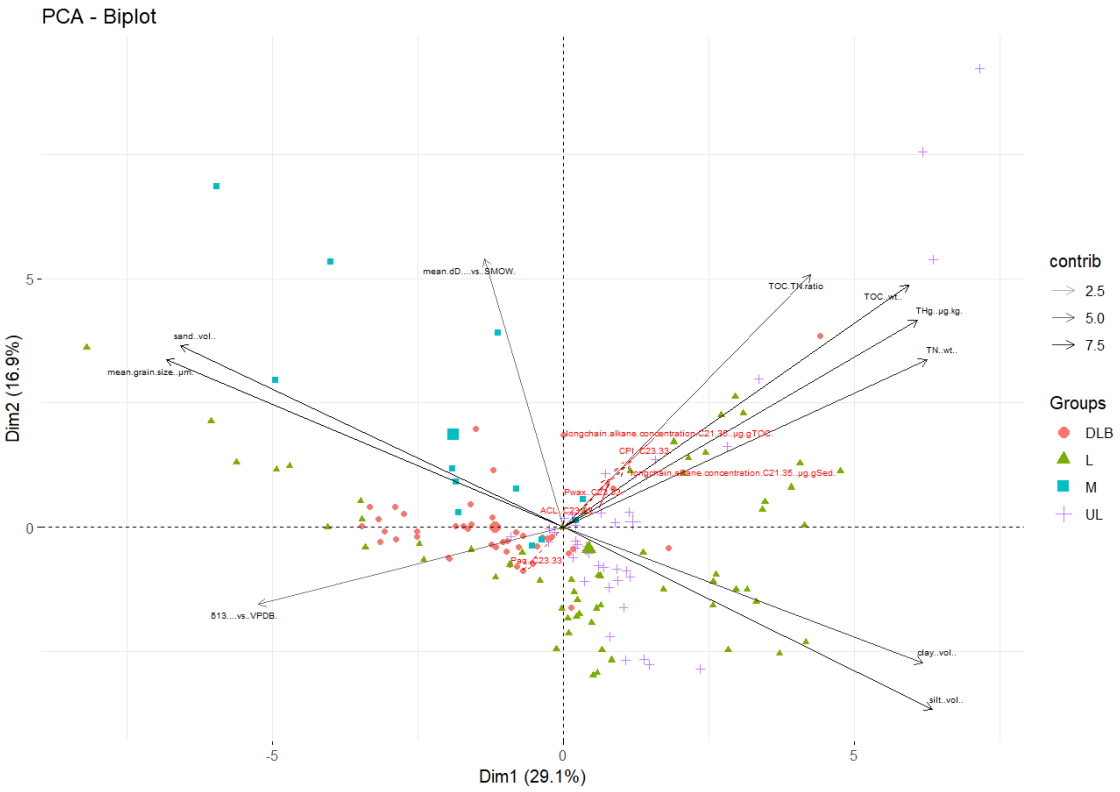


b)

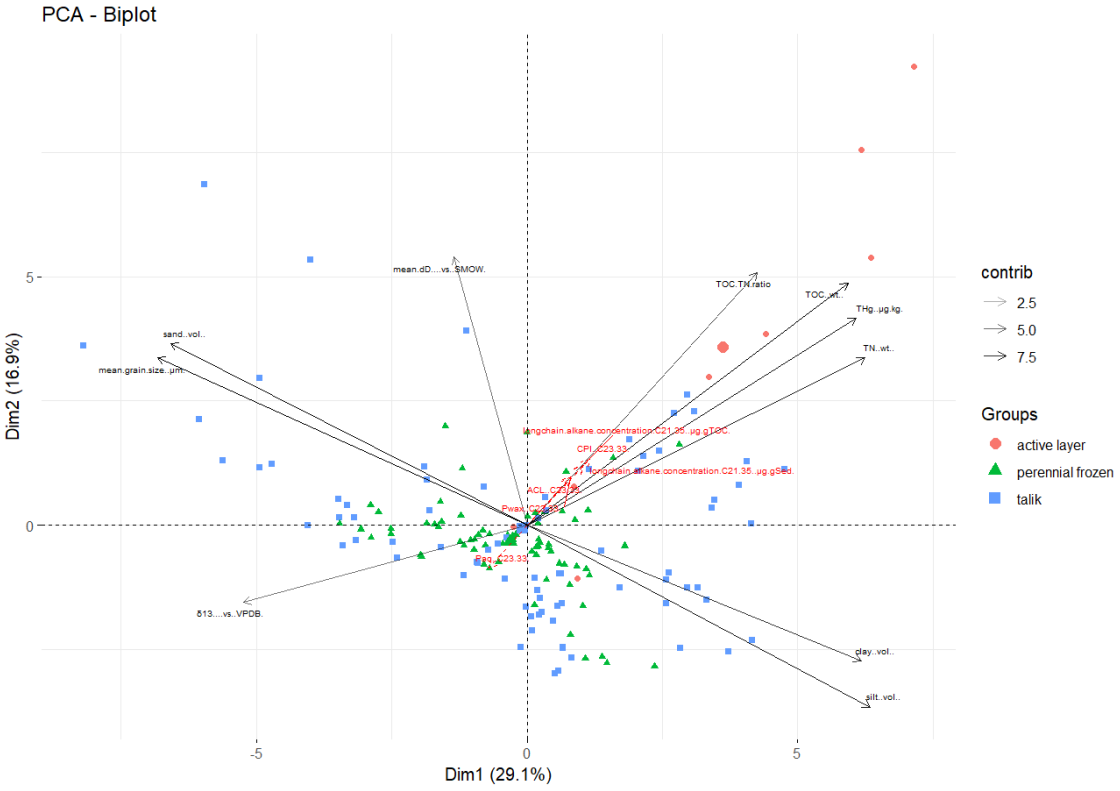

*Figure A. 9. Contribution of (a) cores and (b) permafrost layers to the three different clusters resulting from the HCPC.*

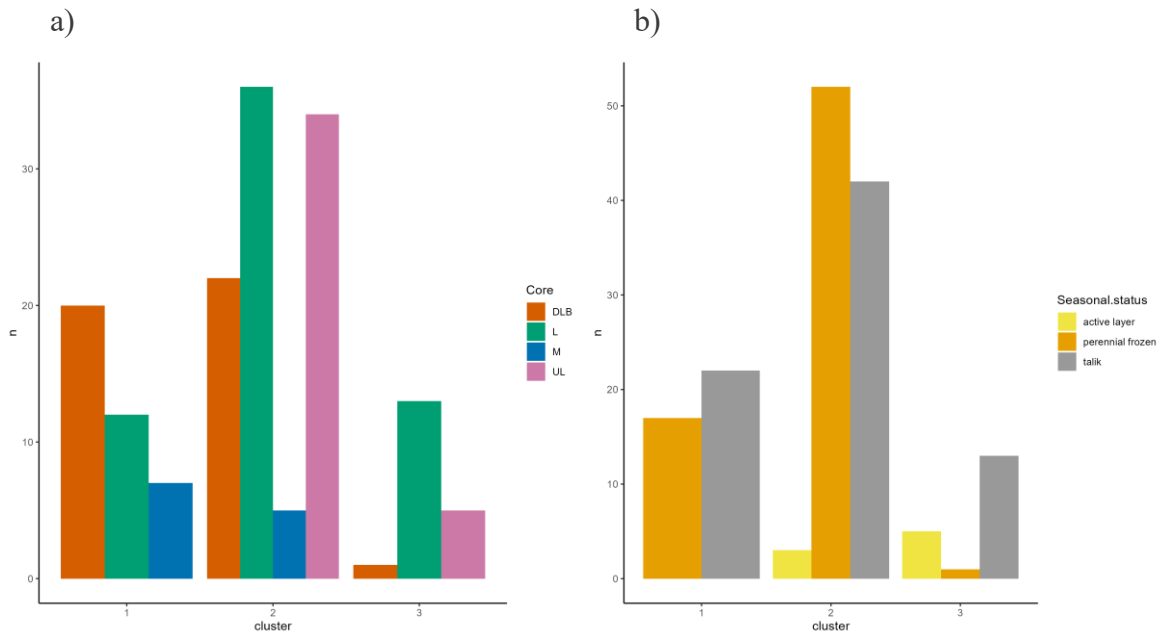

# Acknowledgement

This Master thesis was conducted in the Permafrost Biogeochemistry section at the Alfred Wegener Institute in Potsdam. I would like to express my gratitude for the opportunity to work there and for the warm welcome from such kind colleagues who made me feel part of the team from the very beginning.

A great thank you goes to my supervisors, Dr. Jens Strauss and Prof. Dr. Guido Grosse, for your strong support and your open ears to all my questions. I'm also very grateful to you Fabian Seeman for trusting me with your project and for always being there to help me.

I would also like to really thank Justin Lindemann, Jonas Kaltschmidt, and Alena Kalitzki for your amazing help in the lab, and Torben Windirsch for dedicating so much of your time to introduce me to biomarker analysis and for continuously supporting me throughout the process.

Lovely thanks to my officemates Bennett, Fabian, Lars, Maren, and Verena, who welcomed me into your group and made the time, also outside of work, so amazing.

Last but not least, special thanks to my wonderful friends and my family for supporting me through every phase of this thesis, motivating me, and at times just patiently putting up with me and my doubts. Thank you, Clemens, for all the coworking and for getting through this together with me.

# Statement of Originality

I confirm that this assignment is my own work, is not copied from any other person's work (published or unpublished), and has not previously been submitted for assessment either at the University of Potsdam or elsewhere. By signing this form, I confirm that any use of AI tools will be disclosed in accordance with the university's guidelines and all submitted work represents my own intellectual effort unless properly attributed.

Potsdam, 6 August 2025

Signature (Carolin Luise Frauhammer)